

**WAVEFORM-OPTIMIZED WIRELESS POWER
TRANSFER FOR IMPLANTABLE MEDICAL DEVICES**

LIU ZHONGTAO

(B.Eng., Nanjing University of Science and Technology, P.R.C)

**A THESIS SUBMITTED
FOR THE DEGREE OF DOCTOR OF PHILOSOPHY
NUS GRADUATE SCHOOL FOR INTEGRATIVE
SCIENCES AND ENGINEERING
NATIONAL UNIVERSITY OF SINGAPORE**

2016

Declaration

I hereby declare that the thesis is my original work and it has been written by me in its entirety.

I have duly acknowledged all the sources of information which have been used in the thesis.

This thesis has also not been submitted for any degree in any university previously.



Liu Zhongtao

20 October 2016

Acknowledgements

Four years is a sufficiently long period of time to change a shy boy into a young man. Within these four years, I have experienced the feelings of accomplishment and depression, the happiness and sorrow, the relaxation and high pressure, and a lot of big changes in my life. I would like to thank all the people accompanying my growth here.

First of all, I would like to express my gratefulness and sincere appreciation to my supervisor, Prof. Guo Yongxin, for his support throughout my doctoral study. Without his kind support and continuous encouragement, this work would not be possible. I also would like to thank Prof. Hong Minghui and Prof. Jiang Zhenhui for their time and advice as my thesis advisor committee members through my Ph.D. life.

I'd also appreciate Dr. Zhong Zheng for his detailed guidance, constructive comments on both research and life. I'm also thankful for the assistant given by Huang Andong, who is smart and always active in research discussions. I would also like to thank all my lab mates in the Microwave Research Lab and MMIC Lab for their kind help during the past four years.

Besides, it was my greatest luck and pleasure to join NUS Graduate School for Integrative Sciences and Engineering (NGS). I'd like to present my gratitude to all the NGS staffs for their kind support, financially and emotionally. They make NGS a big family, which I'll always miss for the rest of my life. Thanks for accompanying me in the past four years.

Last, but not least, I would never complete my Ph.D. thesis without the love and generous support from my parents and wife, Dr. An Sai. Whenever

I'm going through difficult times, it is you that encourage me and let me know you'll always stand by my side. I love you.

Table of Contents

Acknowledgements	ii
Table of Contents	iv
Summary.....	vii
List of Tables	ix
List of Figures.....	x
List of Acronyms	xiv
Chapter 1 Introduction.....	1
1.1 Background	1
1.2 Research Motivation	6
1.3 Research Objectives	8
1.4 Research Contributions	9
1.5 List of Publications.....	10
1.6 Dissertation Outline.....	12
Chapter 2 Literature Review	14
2.1 Implantable Medical Devices.....	14
2.2 Wireless Power Transfer	18
2.2.1 WPT System Architecture	19
2.2.2 Technology Categories	20
2.2.3 Radiation Elements Design.....	25
2.2.4 Rectifier Circuits Design.....	31
2.2.5 Waveform Design	36
2.3 Tissue Effects Consideration.....	41
2.3.1 Biocompatible Coating	41
2.3.2 Electromagnetic Exposure Safety Consideration.....	43

Chapter 3 Reconfigurable Diode Topology Designs for Wireless Power Transfer with a Wide Power Range	46
3.1 Introduction	46
3.2 Diode Topologies Design.....	48
3.2.1 Topology Behavior Analysis	48
3.2.2 Reconfigurable Diode Topology Design	53
3.3 Measurement and System Design	57
3.3.1 I-V Curve Measurement	57
3.3.2 WPT Experiment Test.....	59
3.4 Iterative reconfigurable diode topology	63
3.5 Conclusion.....	67
 Chapter 4 Advanced System Block Designs for High-Efficiency Wireless Power Transfer.....	68
4.1 Rapid Design Approach of Optimal Efficiency Magnetic Resonant Wireless Power Transfer System	69
4.1.1 Introduction.....	69
4.1.2 MR-WPT System Model Analysis	70
4.1.3 Rapid Design Approach.....	73
4.1.4 Experiment Result and Analysis.....	76
4.1.5 Effects of Biological Tissue.....	80
4.1.6 Technology Comparison.....	84
4.1.7 Summary	88
4.2 Enhanced Dual-band Rectifier Design with an Ultra-Wide Power Range	89
4.2.1 Introduction.....	89
4.2.2 Rectifier Design	91
4.2.3 Experiment and Measurement	94
4.2.4 Incident Waveform Analysis	96
4.2.5 Summary	100
4.3 Conclusion.....	100

Chapter 5 In-Vivo High-Efficiency Wireless Power Transfer with Multi-sine Excitation	102
5.1 Introduction	103
5.2 Multi-sine Waveform Analysis	105
5.3 System Modelling and Analysis.....	107
5.3.1 Integral Inductor Model	108
5.3.2 Power Transfer Model	110
5.3.3 Reconfigurable Rectifier Topology Design	114
5.4 Experimental Verification	116
5.4.1 Flexible Coil Design	116
5.4.2 MR-WPT System Design	119
5.4.3 Reconfigurable Rectifier with the Multi-sine Waveform	122
5.5 Tissue Effects and In-vivo Test.....	126
5.5.1 Tissue Effects.....	126
5.5.2 In Vivo System Test in Rodent Model.....	129
5.6 Conclusion.....	131
Chapter 6 Conclusion and Future Works	133
6.1 Conclusion.....	133
6.2 Future Works.....	136
Bibliography	139

Summary

For the state-of-the-art implantable medical devices (IMD) design, wireless power transfer (WPT) is a promising technique to deliver power to these devices without percutaneous wires and battery replacements. To establish a high-efficiency wireless power link for IMDs, this thesis presents several new techniques based on the waveform-optimized WPT from the component, circuit block, and system levels, respectively.

From the component level, the reconfigurable diode topology is designed to realize both the low threshold voltage and the independently tuned high breakdown voltage. These properties of the topology are highly desired in improving the performance of the waveform-optimized WPT system.

Besides the novel component level design, new block level designs from both the coil system and the rectifier are considered as well. For the coil system block, a concise mathematical model for the magnetic resonant WPT (MR-WPT) system is demonstrated and the rapid design approach to achieve its optimal efficiency design is proposed. It provides an efficient approach to design and track the maximal efficiency of an MR-WPT system. Meanwhile, for the rectifier design, a dual-band rectifier with the extended power range is designed. It not only extends the rectifier's operating power range by implementing the reconfigurable diode topology but also explores its performance when the optimized waveforms with different power ratios incident.

Based on the component and block level designs, investigations on the system performance of the waveform-optimized WPT are accomplished

thereafter. A completed MR-WPT system with the optimized multi-sine excitation is presented involving integral inductor model, bandwidth calculation, and rectifier topology analysis. Tissue effects and in-vivo test are also considered to present a comprehensive design procedure for a stable and high-efficiency waveform-optimized WPT system for biomedical applications.

In summary, the proposed research thesis presents the design approaches of a high-efficiency waveform-optimized WPT system for biomedical implants from three different aspects: 1) Component level: high-performance diode topology designs; 2) Block level: power-efficient coil system and rectifier designs; 3) System level: WPT system design with the optimized waveform for bio-implants. All the presented designs are fabricated and verified by the measurement results. The contributions of this thesis are summarized as follow:

1. Development of a reconfigurable diode topology and the associated rectifier for an extended-power-range wireless power transfer;
2. Development of a rapid design approach to obtain the optimal efficiency of an MR-WPT system;
3. Development of refined mathematical models for both the coils and the power transfer system in an MR-WPT system;
4. Investigation of optimized waveforms and their efficiency improvement effects with different incident power ratios;
5. Development of a high-efficiency wireless power transfer system with the multi-sine excitation;
6. In-vivo rodent experiment with the multi-sine WPT system for spinal cord stimulator.

List of Tables

Table 1.1 Comparison of different power supplies for IMDs	5
Table 2.1 the state-of-the-art IMDs [1]	16
Table 2.2 Characteristics of different WPT technologies.....	25
Table 2.3 Overview of Coil Systems in Prior Literature	31
Table 2.4 Comparison of state-of-the-art rectifier circuit designs.....	36
Table 2.5 Electrical Characteristics of Human Tissues at 6.78 MHz.....	44
Table 3.1 Equivalent Breakdown Voltages Comparison of the Diode Topologies	58
Table 3.2 Rectifier Performance Comparison in Wide Power Range	63
Table 4.1 Coil Characteristics in the MR-WPT system	76
Table 4.2 Result Comparison and Analysis at 6.78 MHz	78
Table 4.3 Rectifier Performance Comparison	96
Table 5.1 Coil Physical Parameters.....	118
Table 5.2 MR-WPT System Performance	121
Table 5.3 Coil System Performance Comparison	122
Table 5.4 Rectifier Performance Comparison	126

List of Figures

Figure 1.1 Applications of the state-of-the-art implantable biomedical devices. Device figures are downloaded from online resources [30]-[33],[37],etc.	2
Figure 1.2 Timeline of Implantable Pacemaker Development. Device figures are downloaded from [12][13][15],etc.	3
Figure 2.1 System Architecture for Wireless Power Transmission.....	19
Figure 2.2 Schematics of different categories of WPT systems. (a) far-field WPT based on EM radiations. (b) near-field inductive WPT. (c) near-field magnetic resonant WPT. (d) Capacitive coupling WPT.	21
Figure 2.3 Illustration for Induction Calculation by the Biot-Savart Law	27
Figure 2.4 Typical Schematic of the Rectifier.....	34
Figure 2.5 Different Rectifier Topologies for WPT	35
Figure 2.6. (a) Diode's rectification process with CW and multi-sine waveforms. (b) Multi-sine waveform and filtered waveform at the output of receiver	40
Figure 3.1 (a) WPT system diagram (b) Typical rectifier efficiency curve vs. input power (c) Diode's I-V curve and voltage waveforms across the diode in both low and high power range.	49
Figure 3.2 (a) Diode's Equivalent Circuit [67]. (b) Diode's typical I-V Curve	50
Figure 3.3 Typical RF-DC efficiency curve of the diode with different power losses [67].	51
Figure 3.4 Diode Topologies: (a) Single diode (b) diode in series (c) diode with MOSFET (d) Reconfigurable diode topology.	53
Figure 3.5 Topology analysis of the diode-equivalent reconfigurable topology (a) Equivalent topology in ON state (b) Equivalent topology in OFF state with breakdown channel 1 (c) Equivalent topology in OFF state with breakdown channel 2. Dark black lines indicates the valid circuit portions.	54
Figure 3.6 Theoretical improvement of the reconfigurable topology over the traditional off-the-shelf diodes.	57

Figure 3.7 Fabricated circuits and measured I-V curves for the proposed diode topologies	58
Figure 3.8 Inductive WPT test environment of both the transmitter and the receiver with different diode topologies.....	59
Figure 3.9 Inductive WPT test system diagram and measurement environment. .	60
Figure 3.10 Inductive WPT test system diagram and measurement environment.	60
Figure 3.11 Measured system efficiencies and output DC voltages vs. input power of receivers with diode topologies (a)-(d)	60
Figure 3.12 Two types of iterative reconfigurable diode topologies.....	63
Figure 4.1 Magnetic resonant wireless power transfer system prototype	71
Figure 4.2 System Diagram of Magnetic Resonant Wireless Power Transfer	72
Figure 4.3 System Diagram of Magnetic Resonant Wireless Power Transfer	74
Figure 4.4 Coupling Coefficient k_{xy} vs. distance between coil x and y.	77
Figure 4.5 The MR-WPT system performance verification with CST Simulation and the prototype Experiment.	77
Figure 4.6 The MR-WPT system performance measurement with the Rapid Design Approach, CST Simulation and prototype experiment.	78
Figure 4.7 Maximum Efficiency Tracking with the Varying Transmitter-receiver Distance D_{23}	79
Figure 4.8 In-phantom Simulation and in-vitro experiment of the MR-WPT system.....	82
Figure 4.9 MR-WPT system performance verification in phantom model and in minced pork.....	83
Figure 4.10 System diagram of different wireless power delivery approaches. ...	85
Figure 4.11 Demonstration of breakdown point shift by single (0.915 GHz), dual (0.915GHz & 1.8 GHz) and triple (0.915 GHz & 1.8 GHz & 2.1 GHz) band RF power inputs. RF energy is equally delivered from each band.	90
Figure 4.12 Rectifier Structure with different incident strategies (a) Independent input rectifier structure (b) Simultaneous input rectifier structure	91

Figure 4.13 (a) Block structure of rectifier with EPR (b) simulated dual-band RF-DC conversion efficiencies of conventional rectifier and rectifier with EPR in both independent and simultaneous mode. RF energy is equally delivered from each band.....	93
Figure 4.14 Schematics and fabricated circuits of the proposed rectifier with EPR	94
Figure 4.15 Experiment and Measurement Setup	95
Fig. 4.16 Simulated and measured efficiency and output DC voltage of the dual-band rectifier in simultaneous input mode. RF power is equally delivered from each band.	95
Figure 4.17 Investigation of power gain performance of dual-band conventional (diode in series structure) rectifier (0.915GHz: 1.8GHz=1:1) and dual-band rectifier with EPR with different input power ratios (0.915GHz: 1.8GHz).	98
Figure 5.1 Frequency spectrum and time-domain waveforms of 6.78 MHz CW signal and 3-tone 10 kHz-spacing multi-sine waveforms.	106
Figure 5.2 Photography of the planar spiral coil (PSC) and its equivalent models (a) Archimedes spiral model (b) concentric-loop model.....	108
Figure 5.3 Self-inductance and mutual inductance calculation based on the integral inductor model in Cartesian coordinates.	109
Figure 5.4 System Diagram of Magnetic Resonant Wireless Power Transfer	111
Figure 5.5 Iterative Reconfigurable Rectifier Topology	115
Figure 5.6 Coupling Coefficients vs. Separation Distance Configuration.	119
Figure 5.7 (a) Fabricated Flexible Coils (b) In-air Experiment Setup for the proposed MR-WPT system	120
Figure 5.8 (a) Power Transfer Performance of the MR-WPT system in different test environments (b) In Vitro Experiment Setup for the proposed MR-WPT system.....	120
Figure 5.9 I-V curve of the traditional and the reconfigurable rectifier topology	123

Figure 5.10 (a) Circuit Schematics and Fabricated Boards of the Rectifier Topologies. (b) Rectifier Test Experiment Setup. $C1=110\text{pF}$, $C2=500\text{pF}$, $L1=4.7\mu\text{F}$, $RL=1.8\text{K}\Omega$. DUT: Device Under Test.	123
Figure 5.11 Simulated and Measured RF-DC Efficiency and Output Voltage Curves of the Traditional and the Proposed Reconfigurable Rectifier under Various Incident Waveforms. TR: Traditional rectifier, RR: Reconfigurable rectifier, CW: Continuous wave, single frequency, MS: Multi-Sine waveform .	124
Figure 5.12 Three-dimensional Gustav Voxel human body model for the wireless power transfer system implanted in spine	128
Figure 5.13 (a) 1-g average SAR distribution (b) 10-g average SAR distribution (c) temperature variation distribution in voxel human body model.....	128

List of Acronyms

IMD	Implantable Medical Device
WPT	Wireless Power Transmission
MR-WPT	Magnetic Resonant Wireless Power Transmission
SCS	Spinal Cord Stimulator
RFID	Radio-frequency identification
MOSFET	Metal-oxide-semiconductor field-effect transistor
SAR	Specific Absorption Rate
ECG	Electrocardiogram
EEG	Electroencephalogram
SPS	Solar Powered Satellite
WBSN	Wireless Body Sensor Network
EMI	Electromagnetic interference
CW	Continuous Wave
PAPR	Peak to Average Power Ratio
UWB	Ultra Wide Band
OFDM	Orthogonal Frequency Division Multiplex
PDMS	Polydimethylsiloxane
CMOS	Complementary Metal-Oxide-Semiconductor
PCB	Printed Circuit Board
EPR	Extended Power Range
GSM	Global System for Mobile communication
HEMT	High-Electron-Mobility Transistor
PSC	Planar Spiral Coil
LDO	Low Drop-Out
PWM	Pulse Width Modulation

LCR	Inductor-Capacitor-Resistor
GaAs	Gallium Arsenide
PMA	Power Matters Alliance
A4WP	Alliance for Wireless Power
MRI	Magnetic Resonance Imaging

Chapter 1 Introduction

1.1 Background

With the decades of development of modern medicine, it has become a trend to involve the bioelectronics into the daily clinics. It envisions a brand new area for future therapeutics and treatments far from today's medical practices. Different from the traditional medicine based on chemical or biological mechanisms, the emerging bioelectronic medicines explore a new approach for the clinic diagnostics and therapy with greater precision and fewer side effects. In this case, the bio-electronics medicine, e.g. the implantable medical devices [1], hold the potential to be the spotlight of the next generation medical industry.

Implantable medical devices are designed to effectively monitor the patients' physiological signals [2]-[4], implement drug delivery [5] and neural stimulations [6] or restore biological functions of patients [7][8]. So far, there have been some medical devices implanted or ingested into a human body as shown in Fig. 1.1: Artificial pancreas [5] and prosthesis [6] are used to replace the dysfunctional pancreas and limbs of the patients; Cochlear [7] and retinal [8] implants are adopted to restore hearing and sight; Spinal cord stimulators

[9] are applied for pain relief and implantable defibrillators [10] provide treatment for gastric disorder. Future IMDs also hold the potential to be implemented in the treatment of Parkinson's disease [11], Alzheimer's disease and other diseases, which are hard to be cured by traditional pharmaceuticals. With the use of implantable biomedical devices, these diseases could be more effectively treated than by the conventional medicines.

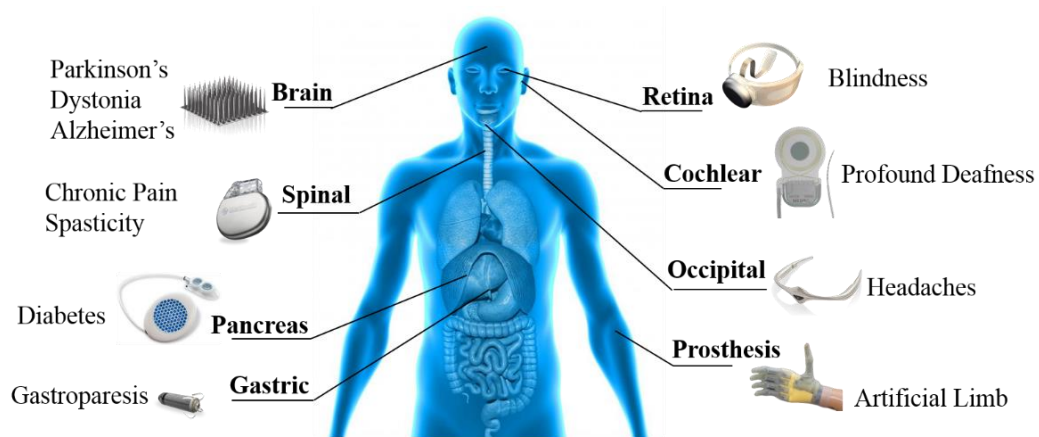


Figure 1.1 Applications of the state-of-the-art implantable biomedical devices. Device figures are downloaded from online resources [30]-[33],[37],etc.

Since the first successful pacemaker implantation [12] in 1958, the IMDs have gone through a substantial progress and development. The traditional implantable devices are, in most cases, simple and bulky. These devices inevitably bring discomfort to the patient and influence their daily lives. Within the recent years, IMDs are experiencing a rapid growth in both their capability and the market. A number of advanced implantable devices have been invented in recent decades with more capabilities and less weight [13].



Figure 1.2 Timeline of Implantable Pacemaker Development. Device figures are downloaded from [12][13][15],etc.

For the advanced IMD designs, there are strong emphases on both increasing its functionalities and miniaturizing its size and weight. With the increased task complexities, more sensors and actuators are implemented and more complicated algorithms are designed in miniaturized devices for monitoring, sampling and stimulating, etc. With the integration of features, the IMDs, on the other hand, require more power consumptions. The large capacity battery is needed to provide sufficient energy for the devices within their lifetimes. However, it turns out that the battery has become the component occupying the most space in the current implantable devices.

Therefore, there always has to be a tradeoff between its high functionality and the sufficiently long lifetime. The tradeoff brings a great design challenge since simply reducing the battery size greatly shortens the device's lifetime and leads to frequent surgeries for the battery replacement. Although the ultra-low power circuit designs [14] are investigated to extend the device lifetime,

the design of a continuous and stable power supply or a reliable recharging approach brings much more possibilities for the future IMDs.

Beyond the bulky battery, the exploration of other feasible power supplies for the IMDs attracts much research attention. Several energy harvesting techniques [15]-[21] have been investigated and proposed for use. Currently, thermoelectricity, piezoelectricity, and electromagnetics (EM) are applied as the potential power sources for the miniaturized IMDs to replace the traditional Lithium battery. Energy harvesting circuits are designed to collect these energies and convert them into the stable DC power to supply the subsequent circuits or to recharge the miniaturized super-capacitors or solid-state batteries for the temporary energy storage.

In order to select a proper power supply for the IMDs, a comparison has been made and presented in Table 1.1 below. Only when a sufficient amount of energy is stably delivered to the devices can the IMDs be designed with the miniaturization and a sufficiently long lifetime. Therefore, the batteryless IMDs with energy harvesting techniques would be a promising solution for the next generation bioelectronic medicine.

Table 1.1 Comparison of different power supplies for IMDs

Ref.	Power Supply	Generated Power	Characteristics
[18]	Lithium-Battery	210 mWh/g	<ul style="list-style-type: none"> • High output power • Large size & Toxicity
[16]	Thermoelectricity	180 $\mu\text{W}/\text{cm}^2$	<ul style="list-style-type: none"> • Unlimited Lifetime • Low output power
[17,19]	Piezoelectricity	0.33 μW - 1W	<ul style="list-style-type: none"> • High Output Power • Limited Implantable Position
[20,21]	Electromagnetics	50 mW -150 mW	<ul style="list-style-type: none"> • High Output Power • Compact Size

Before a power source is selected to supply the IMDs inside the human body, harsh selection criteria should be met due to the high reliability and robustness requirements for IMDs. The tissue cushioning effect and homeothermal property of the human body make it a tough environment for the energy delivery of both thermoelectricity and piezoelectricity. These energy harvesting approaches are no longer valid to provide sufficient and stable energy for the IMDs when implanted inside the human body.

Compared with the other energy harvesting methods, to harvest the EM energy from a dedicated power source outside a human body is a more reliable and feasible solution for the IMD's power delivery. RF energy is transmitted from a dedicated power source outside the human body and wirelessly delivered to the biomedical devices implanted in the brain, eyes, chest, and limbs, etc. The RF power penetrated into human body provides a continuous

and sufficient power supply for the deeply implanted devices, and it can be widely applied in most implantation scenarios. Therefore, to investigate a reliable power supply to replace the traditional bulky battery in the miniaturized IMDs, wireless power transfer (WPT) is a good alternative.

1.2 Research Motivation

Based on the analysis above, WPT is an excellent selection to power the miniaturized IMDs. However, there exist several challenging problems still needed to be solved when designing a high efficiency wireless power link for the bio-implants.

The design challenges have been greatly upgraded when WPT is applied in the biomedical application scenarios to meet the critical design requirements on the high efficiency [49][50], long transmission distance [46][62], and high robustness[56][58][59], with the state-of-the-art specifications presented in chapter 2. In general, when the WPT system is implanted inside human body and the miniaturized receiving coils are surrounded by the biological tissues, it may lead to the potential performance degradation from two aspects: 1) the maximal applicable RF power for the IMDs is limited to follow the maximum electromagnetic field exposure regulations for the patients' safety consideration. 2) The insufficient input power for the rectifiers would also

result in unsatisfactory rectifier performance due to the rectifier's properties.

Lots of research have been conducted on circuit optimization for the both transmitter and the receivers. However, most of the designs are usually based on the single-carrier, continuous-wave (CW) signal transmission waveform.

The transmission waveform optimization was left blank for years and has been recently drawn much research attention as a novel approach for WPT system performance improvement. It been proven to be efficient to improve the WPT system efficiency with high peak to average power ratio (PAPR) waveforms. The waveform optimization enlightens a promising research area for the high-efficiency WPT system design, especially for the challenging implantable biomedical applications. However, the research on the transmission waveform optimization is still in its infancy status, a number of challenging problems need to be solved and lots of research efforts should be taken to make it a practical power delivery solution for the future IMDs.

In this thesis, the research work based on the transmission waveform optimization and the new design considerations of each block are presented to build up a practical waveform-optimized WPT system for the future IMDs.

1.3 Research Objectives

The objective of this thesis is to develop a waveform-optimized wireless power link for biomedical implants and related circuit designs. The primary goal of this thesis includes:

- To investigate the optimized waveforms with various configurations and explore their efficiency improvements over the traditional sine waveform.
- To develop a high-performance diode with an ultra-low threshold voltage and a high reverse breakdown voltage to fit for the optimized waveforms with high voltage peak.
- To present a concise mathematical model of the MR-WPT system and build an algorithm to assist the optimal efficiency design and tracking.
- To provide a completed design procedure for the high efficiency MR-WPT system with optimized waveforms, which includes both the coil system design and the rectifier design.
- To realize a completed high-efficiency WPT system with biocompatibility considerations in an in-vivo rat experiment to verify its capability to be applied in practical implant scenarios.

1.4 Research Contributions

In this thesis, a waveform-optimized wireless power link is for the first time developed for the miniaturized IMDs. Each block is carefully examined and specifically designed for the optimized transmission waveform. A generalized design procedure has also been demonstrated in the waveform-optimized WPT system for implantable biomedical applications. The research contributions of this thesis are categorized into the component, block and system levels, respectively.

From the component level, a reconfigurable diode topology is designed in the thesis to realize both the low threshold voltage and the independently tuned high breakdown voltage, which are the desired characteristics of the waveform-optimized WPT systems. Furthermore, the reconfigurable diode topology design envisions a new approach from the aspect of topology design to improve the diodes' performance apart from the traditional approaches to exploring advanced semiconductor materials.

From the circuit block level, improvements are implemented from both the coil system design and the rectifier design. For the coil system design, a concise mathematical model for the MR-WPT system is presented and the rapid design approach is designed to find the optimal efficiency configurations

and the maximum efficiency tracking strategy. For the rectifier design, besides the reconfigurable diode topology implementation, the investigations on the efficiency enhancement effect with different transmission waveforms are initialized. The simultaneous incident of multiple frequencies is proved to have better rectification efficiency and different power ratios of the incident waveforms are also explored.

From the system level, a completed waveform-optimized MR-WPT system is demonstrated in chapter 5 for the implantable medical devices. The system achieves high overall efficiency while giving a completed design procedure for applying the optimized multi-sine waveforms with a high PAPR. System-level design considerations on the flexible coil design, power transfer model, waveform configuration and rectifier topology design are all involved to improve the overall system efficiency. With all the optimized designs, the multi-sine waveform is for the first time implemented in an in-vivo MR-WPT system for the IMD power delivery. Biocompatible considerations such as the low SAR and temperature increase are also demonstrated to guarantee a safe WPT system for the biomedical implants.

1.5 List of Publications

The related publications are listed below.

- [1] Zhongtao Liu, Zheng Zhong and Yong-Xin Guo, "In vivo High-Efficiency Wireless Power Transfer with Multi-sine Excitation," IEEE Transaction on Microwave Theory and Technique (Under Review).
- [2] Zhongtao Liu, Zheng Zhong and Yong-Xin Guo, "Reconfigurable Diode Topology for Wireless Power Transfer with Wide Power Range," IEEE Microwave and Wireless Components Letters, vol. 26, no. 10, pp. 846-848, Sep 2016.
- [3] Zhongtao Liu, Zheng Zhong and Yong-Xin Guo, "Rapid Design of Optimal Efficiency Magnetic Resonant Wireless Power Transfer System," Electronic Letters, vol. 52, no. 4, pp. 314-315. Feb 2016.
- [4] Zhongtao Liu, Zheng Zhong and Yong-Xin Guo, "Enhanced Dual-band Ambient RF Energy Harvesting with Ultra-Wide Operating Power Range," IEEE Microwave and Wireless Components Letters, vol. 25, no. 9, pp. 630-632, Sep 2015.
- [5] Zhongtao Liu, Zheng Zhong and Yong-Xin Guo, "Intermodulation Harvesting Rectifier Design for High-Efficiency Multi-sine Wireless Power Transfer," IEEE MTT-S International Microwave Symposium Digest, San Francisco, CA, USA, 2016, pp. 1-3.

[6] Zhongtao Liu, Zheng Zhong and Yong-Xin Guo, “Iterative Non-breakdown Rectifier Topology for Via-Tissue Multi-Sine Wireless Power Transmission,” IEEE MTT-S International Microwave Workshop Series on RF and Wireless Technology for Biomedical Healthcare Application, Taipei, 2015, pp. 102-103. **(2nd Best Student Paper Award)**

[7] Zhongtao Liu, Zheng Zhong and Yong-Xin Guo, “High-Efficiency Triple Band Ambient RF Energy Harvesting for Wireless Body Sensor Network,” IEEE MTT-S International Microwave Workshop Series on RF and Wireless Technology for Biomedical Healthcare Applications, London, 2014, pp. 1-3.

[8] Yong-Xin Guo, Zheng Zhong, Zhongtao Liu, The Application of Multi-Carriers Wireless Power Transmission towards Implantable Biomedical Devices. China Patent 201510449145.4. (Pending)

1.6 Dissertation Outline

This thesis is organized as follows: chapter 2 presents a comprehensive literature review for readers with either electrical or biomedical engineering backgrounds. It introduces the implantable medical devices, wireless power transfer technique with optimized waveforms and bio-compatible considerations in the device implantations. The new techniques involved in the

waveform-optimized WPT system designs are presented in chapters 3, 4 and 5, respectively. Firstly, a new reconfigurable diode topology is presented in chapter 3 as the contribution from the component level. Secondly, block level designs are presented in chapter 4. The coil system design and rectifier design with waveform optimization investigation are investigated in section 4.1 and 4.2, respectively. Lastly, a design guideline for the waveform-optimized WPT systems as well as a completed in-vivo WPT system with the optimized multi-sine waveforms are presented in chapter 5 for the next generation miniaturized spinal cord stimulator (SCS). The rodent experiment is applied to verify and demonstrate the new waveform-optimized WPT system design. Chapter 6 summarizes the thesis and draws the conclusion and future works.

Chapter 2 Literature Review

A comprehensive literature review is presented in chapter 2 to introduce the developments of the state-of-the-art implantable medical devices and to investigate the technical details of the waveform-optimized WPT systems and the associated implantation considerations.

2.1 Implantable Medical Devices

Within the recent years, escalated incidence of cancer and cardiovascular diseases has become global healthcare challenges. Aside from the delayed diagnostics and expensive therapy from the traditional approach, the future healthcare should draw specific attention on the prevention, early detection and treatments with minimal invasion [22]. The advanced development of the current IMDs has enabled an unobtrusive health monitoring and replaced the traditional episodic sampling operations with the automatic continuous sampling and intelligent intervention. For the future health management, the miniaturized IMDs play a significant role in both sensing and stimulating. Advances in the IMDs' development support the small, lightweight and *in-vivo* stable sensors and actuators with a long operating lifetime and the minimal incision.

IMDs have been widely applied in monitoring critical health indicators, the nerve stimulating and drug delivery. Key physiological signals such as electrocardiogram (ECG) [2], electroencephalogram (EEG) [3], blood oxygen saturation [23] and body temperature [24] are continuously monitored and the current IMD systems also have the capability to deliver drugs like insulin [25] to blood and electric stimulations to brain [26] or peripheral nerves [27]. The implementation of the IMDs brings great convenience to the disease prevention and patients' treatments. For example, the patients suffering from the chronic pain would no longer have to take the analgesics and avoid the drug addiction risk if a miniaturized neural stimulator is implanted around the spine cord of the patient for intelligent pain management [28]. The patient can also control their blood glucose levels by tailoring the delivered insulin amount the implantable artificial pancreas [29]. Due to the high demand for biomedical signal monitoring and therapy delivery, the evolution of IMDs has been accelerated in the past decade. Some state-of-the-art IMDs [1] from both academia and industry haven been summarized and presented in Table. 2.1 below.

Table 2.1 The state-of-the-art IMDs [1]

Sensors Type	Key Technical Features	Clinical focus	Citation
Heart rhythm	Implantable defibrillator	Cardiac arrhythmia	Evera [30]
Temp. & Respiration	Ingestible capsule for wireless core temperature	Infection	VitalSense [31]
Auditory nerve	Auditory nerve stimulation	Deafness	Cochlear [32]
Visible light	Retinal ganglion cells stimulation	Blindness	SecondSight [33]
Brain stimulator	Single lead implantable neurostimulator	PD, Tremor	Solettra [34]
Medicine ingestion	Ingestible pill with wireless interrogation for ingestion signatures	Tablet ingestion management	Proteus [35]
Force sensor	Battery-less piezoelectric energy harvester knee implant	Knee replacement	[36]
Pressure sensor	Complete artificial heart	Heart replacement	Carmat [37]
pH	pH capsule attached to esophageal wall	GERD	[38]

The IMDs in Table. 2.1 are categorized by its functionalities. The technical features and clinic focuses of each IMD are also listed for review. For most biomedical applications, the IMD serves as a continuous monitoring tool, replacement prosthesis and long-term medicine ingestion. These implanted electronic devices are designed to monitor the body core temperature [31], the pH value in stomach [38] and to replace the patients' retina [33], knee [36] and even heart [37].

Along with the IMD's substantial progress and innovations, several critical requirements always need to be carefully evaluated when designing an implantable electronic system:

1. Miniaturized size and light weight. Miniaturized IMDs would have smaller incision during implantations. The smaller and lighter devices bring less discomfort and pain to the patient as well.

2. Sufficient long lifetime. It is noted that the IMDs with an increased functionalities require more power consumptions from the limited battery capacities and accordingly holds a short operating lifetime. Since the implantation surgery is rather costly and time-consuming, sufficiently long lifetime and high device reliability of the device is crucial.

3. In-vivo stability. For an implantable electronic device, good biocompatibility is important due to the complicated human biological response to the synthetic materials used in device fabrication [18]. A reliable coating solution should be provided to overcome the infections with long-term implant utilizations.

In summary, the challenges of a chronic or even permanent implant remain to be in the spots of minimal invasion, active power management, long-term

device stability and biocompatibility. For the miniaturized batteryless implants, wireless power transfer is deployed as a good candidate for the energy source, which non-invasively provides sufficient energy from outside the human body and largely extend the IMD's operating lifetime. To power the miniaturized medical devices with a high efficiency wireless power link has become a trend and consequently, the research and development on wireless power transfer for biomedical devices will be under the spotlight for quite a long period of time in future.

2.2 Wireless Power Transfer

The concept of wireless power transfer was for the first time raised when Nikola Tesla invented the wireless power transfer coil [39] in 1889, which is named Tesla coil later on. The wireless power transfer technique has enabled the devices to be compact in size and light in weight, which may be leveraged to increase its feasibility to realize the batteryless miniaturized design. It can be perfectly applied in the scenarios where interconnecting wires are hard or even impossible to access. Starting from the Tesla coils, several WPT approaches have been developed and applied in different practical scenarios. The following sections present a detailed review of the WPT system architecture, categories and functionalities of each system block.

2.2.1 WPT System Architecture

Although various WPT systems have been developed with different target applications [18][22][40] and unique features, they all share the same system architecture and the core components that allow the RF energy to flow from the generator to the target device wirelessly. The generalized WPT system architecture is illustrated in Fig. 2.1. In the architecture, a wireless transmitter connected to a power source conveys the time-varying electromagnetic fields across an intervening space via the transmitting element, either the antennas or coils. The receiving element, as the counterpart of the transmitting elements, receives the EM energy and the rectifying circuits in the receiver block are designed to convert the oscillating RF energy back into DC power to supply the subsequent circuits.

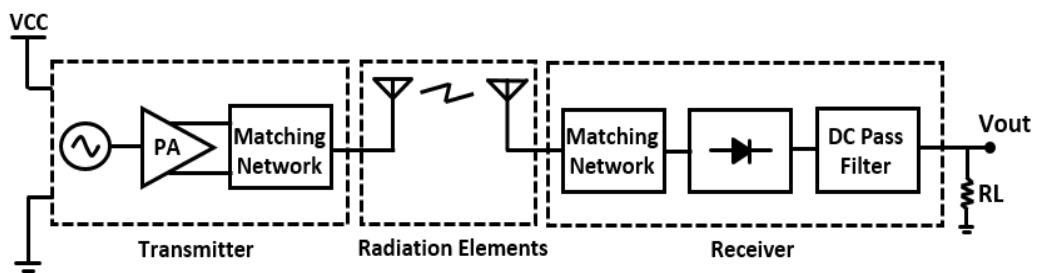


Figure 2.1 System Architecture for Wireless Power Transmission

As shown in Fig. 2.1, there are three major blocks in the WPT system architecture: the transmitter, the radiation elements and the receiver. Since the techniques involved in the transmitter design are rather different from the

other two blocks, the transmitter design is temporarily out of the scope of this thesis. The radiating elements and receiving circuits are the two significant blocks for the WPT system architecture. The radiating element block includes antennas operating in the far field and coil pairs in near field. They are applied to excite the oscillating E-field or H-field with the power incident from the RF generator and received by the other side without any accessible medium in between. The receiver block serves as the RF-DC converter to rectify the received RF signals into stable DC power to supply the circuits. In the following sections, the techniques and design considerations in the radiation elements and receiver blocks are presented in detail.

2.2.2 Technology Categories

Based on the system architecture, the WPT technique can be classified into four categories as shown in Fig. 2.2 based on its operating mechanisms: 1) far-field WPT based on the electromagnetic radiation; 2) near-field inductive WPT; 3) near field magnetic resonant WPT; 4) capacitive coupling WPT.

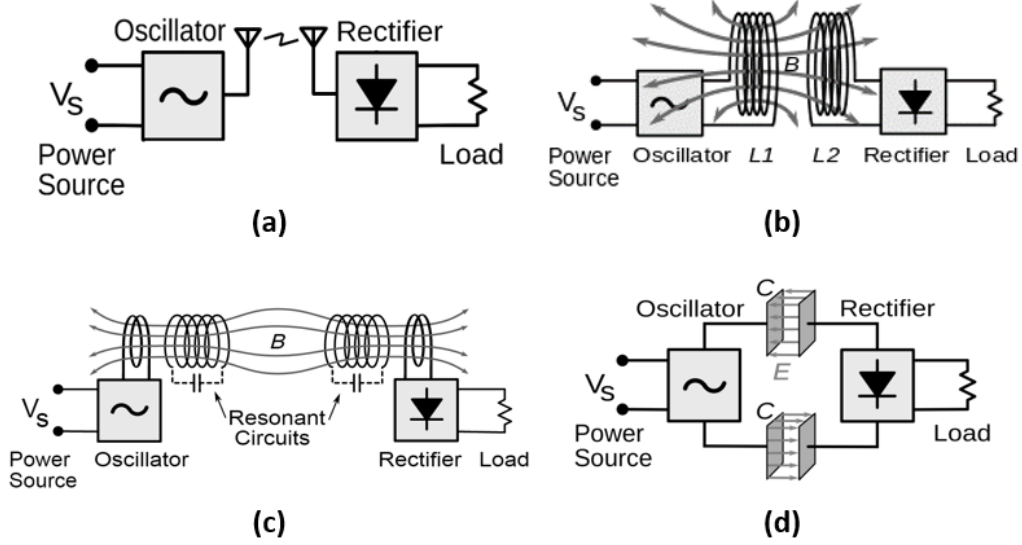


Figure 2.2 Schematics of different categories of WPT systems. (a) far-field WPT based on EM radiations. (b) near-field inductive WPT. (c) near-field magnetic resonant WPT. (d) Capacitive coupling WPT.

In Fig. 2.2(a), the far-field WPT transmits the RF energy by the changing electromagnetic fields excited by antennas. It has been applied to the applications such as the solar power satellites (SPS) [41], radio-frequency identification (RFID) [42] and ambient RF energy harvesting [43][44]. It is able to work for long range and omnidirectional power delivery with different antenna patterns. However, the far-field WPT suffers from a high path loss as the Friis transmission equation [45] indicates and the propagating E-field has a high dielectric loss [46] and absorption rate in tissue. Although there are some literatures on the far-field WPT systems [47][48] for biomedical applications, it is still a less practical approach for the targeted high efficiency WPT system for IMDs.

Fig. 2.2(b) and 2.2(c) show the two major categories of the near-field wireless power transfer techniques. Both of them are widely used in the biomedical applications [18][21][46]. In the inductive wireless power transfer in Fig. 2.2(b), an “air-borne transformer” is formed by the transmitter and the receiver coils. As Ampere’s law presents, the oscillating current in the transmitter coil generates an alternating magnetic field. An induction current is accordingly generated in the receiving coil when the magnetic field goes through the receiving coil. The induced current is then delivered to power the load. The delivered power is in proportion to the received magnetic flux from the transmitter coil, which is represented by the mutual inductance M between the two coils. Ferrite cores can be used to confine the magnetic flux inside the core and improve the mutual inductance between the two coils. However, the heavy and bulky characteristics of the ferrite make it hard to be applied in a certain application scenarios such as the bio-implants. The inductive wireless power transfer currently is the most widely used technology for transcutaneous power delivery of the IMDs. Insulin pumps and cardiac pacemakers are applying it to avoid the transcutaneous wire with the potential infection risk.

The inductive wireless power transfer is able to achieve excellent performance but only at the adjacent very close distances. For the increasing

demands of deeply-implanted IMDs, the magnetic resonant wireless power transfer as shown in Fig. 2.2(c) has become a better alternative. The power is delivered through the strongly coupled magnetic resonant tanks. The resonant tank includes the coil and the tuned-to-resonance capacitor with their parasitic resistances. By applying the two additional resonant tanks, the resonances between the transmitter and receiver sides are greatly increased as well as the coupling and the power transfer efficiency. The idea of the magnetic resonant wireless power transfer [111] is for the first time raised in 2007 by Marin Soljacic from MIT. 60 W power is transferred at a distance of 2 m with 10 MHz magnetic resonant coils working with around 40% efficiency. The magnetic resonant wireless power transfer has gradually been incorporated in the wireless power systems such as Qi [113] and AirFuel Alliance [114] (incorporated by PMA [115] and A4WP [116] recently). Taking advantages of its great characteristics, the magnetic resonant wireless power transfer has drawn more attention on its application for biomedical devices.

Fig. 2.2(d) presents the WPT system based on the capacitive coupling mechanism [51]. Instead of relying on the induction between coils, the capacitive coupling WPT system applies a totally different approach. A “capacitor” is formed by between the transmitter and the receiver electrodes

and the medium in between (skin tissue for biomedical applications). When a voltage is applied on the transmitter electrode, an alternating electric potential is generated in the receiver electrode by electrostatic induction. When a loop is formed in the circuit, the power with an oscillating voltage is delivered from the transmitter side to the receiver side. Due to its capacitive mechanism, power can only be transmitted within a very close distance. The capacitive coupling WPT has been used in some low power biomedical applications [52]. However, the high voltage on both the electrodes for power delivery may lead to potential risks for human body. Besides, the human tissues between the two electrodes would suffer from a high exposure of the electromagnetic power, which may cause unpredicted problems when the SAR limit is reached. However, the capacitive coupling WPT holds several advantages over the induction-based WPT as well. The electric fields for power delivery is only valid within the two electrodes and there are much less leakages and interferences with the extraneous objects.

In brief, the different WPT techniques differ in transmitting range, operating frequencies and accordingly application scenarios. A brief summary is presented in Table. 2.2. The technique selection for a certain application is,

in most cases, dominated by its requirements on the desired transmit range, transmit power, efficiency and cost, etc.

Table 2.2 Characteristics of different WPT technologies

Technology	Range	Frequency	Transmit Elements	Application
Inductive coupling	Short	kHz - MHz	Wired coils	Consumer electronics, electric vehicles, NFC, smartcards
Magnetic Resonant coupling	Mid	kHz - GHz	Wired coils & resonator	Charging portable devices, biomedical implants
Capacitive coupling	Very Short	kHz - MHz	Electrodes	Charging portable devices, IC power routing
Far-field WPT	Long	GHz	Antennas	Solar power satellite, powering drone aircraft, RFID

2.2.3 Radiation Elements Design

The “radiation element” in the WPT system is a generalized term for either the antennas for far-field applications or the coils for near-field applications. For the biomedical applications proposed in this thesis, the far-field WPT with the antenna as its radiation element may not be an appropriate selection as discussed in the prior sections. Therefore, the technical analysis presented in this section would be mainly based on the coil pairs, which are the better alternative for the biomedical applications.

The coil, in general, is an electrical conductor with various shapes like spiral or helix in typical. As the consequence of the Faraday's law, when a coil with a certain shape is in close proximity to the other, the varying current in one fraction generates a magnetic field and induces an electromagnetic force in the other fraction and vice versa. Besides the ferrite that is commonly used in the electrical transformers, the medium where the magnetic fields propagate could be selected with various materials. For the wireless power transfer system in this thesis, the air and the biological tissue have been applied as the medium for field propagation and power delivery.

As is known for the induction, besides feeling a force from the external magnetic fields, an electric current also generates its own magnetic field. The experimentally determined rule for calculating this generated magnetic field is called Biot-Savart Law. The magnetic field generated by the steady linear current I in the wire has been defined in in Eq. (2.1).

$$\mathbf{B}_1(\mathbf{r}) = \frac{\mu_0 I_1}{4\pi} \int \frac{d\mathbf{l}_1 \times (\mathbf{r} - \mathbf{r}_1)}{|\mathbf{r} - \mathbf{r}_1|^3} \quad (2.1)$$

Assuming coil 1 with an oscillating current generates its magnetic fields as Fig. 2.3 shows, the vector \mathbf{r}_1 is the location of the wire in coil 1 with current and \mathbf{r} is the point where the magnetic field is calculated. The constant μ_0 is the

permeability of the surrounded environment. In most cases, the constant μ_0 in free space is 1.256×10^{-6} H/m.

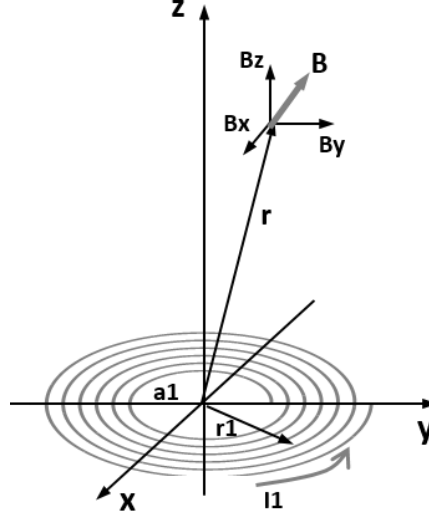


Figure 2.3 Illustration for Induction Calculation by the Biot-Savart Law

It is important to know from Eq. (2.1) that the magnetic field \mathbf{B}_1 is proportional to the current I_1 and the flux through the coil 1 itself is shown in Eq. (2.2) below, where the integral is over the area covered by coil 1.

$$\Phi_{11} = \int \mathbf{B}_1 \cdot d\mathbf{a}_1 \quad (2.2)$$

The self-inductance of the coil is defined and calculated in Eq. (2.3) [54].

$$L_1 = \frac{\Phi_{11}}{I_1} \quad (2.3)$$

Based on the Biot-Savart law and the magnetic flux equation (2.2) above, the mutual inductance representing the portion of magnetic flux received by the coil 2 is derived in Eq. 2.4. The magnetic flux can also be rewritten as Eq. 2.5 by the magnetic vector potential \mathbf{A}_1 .

$$\Phi_{21} = \int B_1 \cdot d\mathbf{a}_2 \quad (2.4)$$

$$\Phi_{21} = \int (\nabla \times \mathbf{A}_1) \cdot d\mathbf{a}_2 \quad (2.5)$$

Eq. (2.5) is rewritten as a line integral in Eq. (2.6) by applying the Stoke's theorem.

$$\int (\nabla \times \mathbf{A}_1) \cdot d\mathbf{a}_2 = \int \mathbf{A}_1 \cdot d\mathbf{l}_2 \quad (2.6)$$

Referring to [11][46], we have the equation for the magnetic vector potential in Eq. (2.7).

$$\mathbf{A}_1(\mathbf{r}_2) = \frac{\mu_0 I_1}{4\pi} \int \frac{d\mathbf{l}_1}{|\mathbf{r}_2 - \mathbf{r}_1|} \quad (2.7)$$

Therefore, the formulas of the magnetic flux and the mutual inductance between two loops are shown below. Eq. (2.9) is also known as the Neumann formula [55].

$$\Phi_{21} = \frac{\mu_0 I_1}{4\pi} \iint \frac{d\mathbf{l}_1 \cdot d\mathbf{l}_2}{|\mathbf{r}_2 - \mathbf{r}_1|} \quad (2.8)$$

$$M_{21} = \frac{\mu_0}{4\pi} \iint \frac{d\mathbf{l}_1 \cdot d\mathbf{l}_2}{|\mathbf{r}_2 - \mathbf{r}_1|} \quad (2.9)$$

For the implanted coil design in medical devices, the advantage of the coils is indicated in Eq. (2.1) that the permeability constant μ_0 has only little variation when its surroundings are non-metallic materials such as human tissue [46]. This unique characteristic presents highly desired properties of the MR-WPT system design for biomedical implants.

However, it is still challenging to design a high efficiency coil pair for the IMDs since the coil misalignment frequently occurs. In the coil-based WPT systems for bio-implants, the receiving coil is significantly smaller than the transmitting coil and it is implanted beneath the tissue. It is hard to predict the exact location of the implanted small coil and always keep its alignment. Although the theoretical derivation above models the coil system, further research is still desired to present an accurate coil system model and to explore the optimal coil pair designs.

Firstly, it is difficult to accurately model the coils considering all the parasitic parameters and the mutual coupling between either two fractions of wires before it is actually built. As indicated, the magnetic flux in Eq. (2.1) is not only in proportion to the current I_1 but also highly related to the geometry of the two loops. A number of simplified and empirical equations are presented in [55] for coils with different shapes such as square, hexagonal, octagonal and circular. In most cases, the multi-turn circular coils are modeled as several concentric loops [56] with different diameters. These equations hold an acceptable accuracy in most cases with a large number of turns. However, the accuracy of these models drops and is no longer acceptable when they are applied to model the coils with only a few turns or large turn spacing, which

are frequently used in MR-WPT systems as its drive and load loop as shown in Fig. 2.2(c).

Secondly, a proper coil geometry design is crucial to obtain good transfer efficiency [46][49][50] and larger alignment flexibility[57][58] since the coil pair performance is largely determined by the coil geometry. The magnetic field distributions [56] of the transmitter coils with different configurations are modeled to find the optimal location and angle to achieve the maximum energy transfer. Analytical models [58] are derived to investigate the H-fields at the receiving coil in both lateral and angular misalignment situations. Moreover, the unique bowl-shaped helical coil [57] is designed to excite an evenly distributed H-field to enable the free-positioning of the receiver coils. Since the coils would always have to be designed under various size and shape constraints in practical products, a few optimization technologies are developed to compensate for the physical constraints and track its optimal efficiency with sophisticated designed approaches [59][60]. The state-of-the-art coil systems are presented below in Table 2.3 for an overview. In the comparison, the MR-WPT systems generally gets higher transfer efficiency and longer transmission distance than the inductive system, although different

system configurations are applied. Detailed theoretical analysis will be presented in chapter 4.

Table 2.3 Overview of Coil Systems in Prior Literature

Reference	Type	Coil Dimension (r_p, r_s)	Distance (mm)	Efficiency (%)
[49]	Inductive	(35,10)	20	30
[61]	Inductive	(26,,5)	15	22
[62]	Inductive	(5,5)	12	40
[50]	Magnetic Resonance	(30,30)	80	68
[46]	Magnetic Resonance	(32,11)	32	72

2.2.4 Rectifier Circuits Design

In the WPT system design, the rectifier circuits design is another important aspect to consider besides the coil pairs analyzed above. The efficiency to convert the RF signal to DC power is one significant portion of the overall WPT system efficiency. In order to accomplish the rectifier design with satisfactory RF-DC performance, proper diode and rectifier topologies should be carefully selected and designed.

2.2.4.1 Diode Behaviors

In order to achieve the desired performance of the rectifier, the diode in use is the critical component to be studied first. The diode is a nonlinear component to convert the received RF signal into DC power. Several critical specifications should be considered to evaluate its performance such as the threshold voltage V_{th} , reverse breakdown voltage V_{br} , parasitic capacitor C_j and parasitic resistor R_s .

To describe the diode behavior, the nonlinear I-V relationship [63] between the current flow through the diode and the applied voltage is expressed as follows before the diode breaks down

$$I_D = I_s \left(e^{\frac{V_d}{nV_t}} - 1 \right) = I_s \left(e^{\frac{V_b - R_s I_D}{nV_t}} - 1 \right) \quad (2.10)$$

where I_s is the diode saturation current and V_d is the voltage across the Schottky barrier. From the diode's I-V curve, when the applied voltage forward biases the diode, the current flow through the diode increases. The equivalent resistance R_{eq} decreases rapidly when the applied voltage is larger than its threshold voltage V_{th} . When a reversely-biased voltage applies, the diode is turned off and only a small amount of leakage current flows through the diode with an almost infinite R_{eq} . When the reverse bias voltage falls below the reverse breakdown voltage V_{br} , the diode drastically breaks down

with a large reverse current reversely flows, resulting in a substantial power loss.

Besides the characteristics of threshold voltage V_{th} and breakdown voltage V_{br} , there are two device parasitic parameters [64] acting as the critical factors that affect the diode performance: the junction resistance R_s and the junction capacitance C_j generated from the semiconductor structure. The junction resistance R_s influences the overall RF-DC efficiency since it dissipates power when the current flows through the diode in rectification. The junction capacitance C_j limits the maximum operating frequency of the diode since it forms an equivalent low-pass filter in the semiconductor structure and performance degradation occurs when the operating frequency is high.

2.2.4.2 Rectifier Design

Based on the diode behaviors, rectifiers are able to be designed accordingly to meet various design requirements. A rectifier basically consists of a band-pass filter, a nonlinear rectifying component and a DC pass filter. The basic structure of the rectifier is presented in Fig. 2.4.

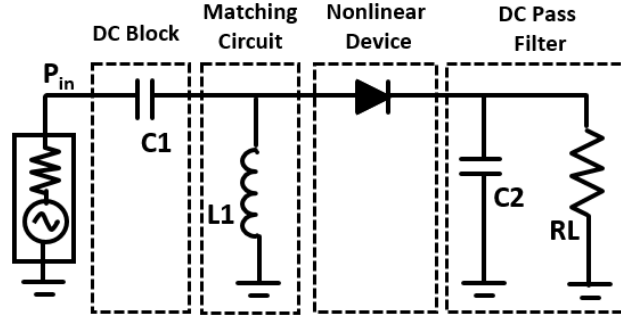


Figure 2.4 Typical schematic of the rectifier

When an RF signal incidents from the antenna, the band-pass filter serves as a matching circuit to allow the desired RF signal to feed into the rectifier and at the same time prevent the reflected harmonics from transmitting out via the antenna. Then, the nonlinear diode rectifies the incident signal and generates several spectral components: DC, fundamental, harmonic components or even intermodulation components when a modulated signal is fed. The DC pass filter is designed to pass the generated DC components and reflects all other spectral components.

In order to achieve the optimal performance of the rectifier, a critical factor, RF-DC conversion efficiency η , is firstly defined to evaluate the rectifier performance. The RF-DC efficiency is the power ratio of the output DC power, which is measured by the output DC voltage over the load resistor, over the received RF power P_{in} as shown below

$$\eta = \frac{V_{DC}^2}{R_L \cdot P_{in}} \quad (2. 11)$$

where V_{DC} is the output DC voltage, R_L is the load resistor. P_{in} is the input power. With the goal of the maximum RF-DC efficiency, optimal rectifier designs have been achieved in single-band [47][67], dual-band [70] and broadband [43] modes and with different rectifier topologies [64][71][72].

For the rectifier topology designs, the most commonly used topologies [66] are shown in Fig. 2.6, which includes the diode-in-series, the diode-in-shunt, the charge pump and the diode bridge topology.

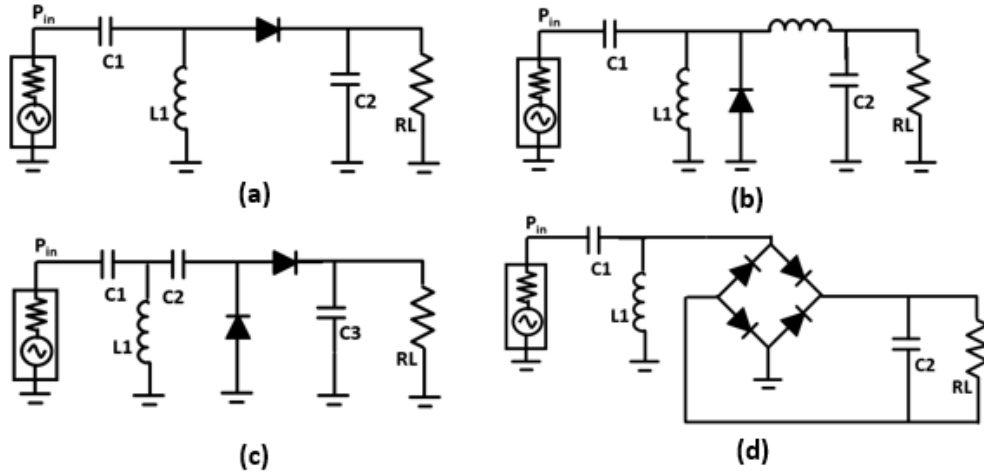


Figure 2.5 Different Rectifier Topologies for WPT

The diode-in-series, diode-in-shunt topology in Fig. 2.5(a) and 2.5(b) are usually applied in scenarios where high efficiency is paramount. The diode bridge in Fig. 2.5(d) is designed for full-wave rectification and has larger power handling ability. In the charge pump topology in Fig. 2.5(c), each stage serves as the bias reference for the latter stage and consequently a larger output voltage is obtained. Although the charge pump topology has a degraded

RF-DC efficiency since more diodes are involved, it holds the advantage to generate a sufficiently high output voltage at a low power range to turn on the subsequent circuits. A cascaded charge pump is commonly used in RFID designs [73] to increase the voltage levels to be able to power the circuits.

Upon the analysis above, Table 2.4 presents a list of the state-of-the-arts rectifier designs. They have been optimized for different bands and topologies based on their application requirements.

Table 2.4 Comparison of state-of-the-art rectifier circuit designs

Reference	Rectifier Topology	Frequency (GHz)	Pin (dBm)	Efficiency (%)
[72]	Series diode	0.85 & 2.45	-20	18 & 10
[73]	Shunt diode	10	[19 ~24]	[25 - 40]
[74]	Voltage doubler	2.45	[-20 ~10]	[30 - 68]
[63]	Class-F	5.8	[0~18]	[30 - 80]
[43]	Shunt diode	2-18	[-17 ~15]	[0.1 - 20]
[75]	pHEMT	0.9	[0 ~11.5]	[27 - 85]

2.2.5 Waveform Design

For the decades of development [76], the transmission waveform used in the WPT system is always the traditional single frequency, continuous wave (CW) sine waveform. Although there have already been a multitude of

research efforts on the circuit-level optimizations on both transmitters and receivers, little attention has been drawn on the waveform optimizations until the recent years. Compared with research on the transmitter and receiver optimizations, there is still much space to work on an appropriately optimized transmission waveform.

It has been found in [77] that the waveforms featuring a high peak-to-average-power-ratio (PAPR) have the capability to improve the rectification efficiency when compared with the traditional uniform amplitude sine waveform. A number of waveform designs, such as the ultra-wide-band (UWB) signals [78], harmonic signals [79], chaotic signals [80] and the multi-sine signals [65][81][82], have been proposed to provide efficiency improvement in WPT systems.

It is noted that applying the UWB signal would increase the rectification efficiency [78]. However, its 2-8 GHz ultra-wide bandwidth leads to a challenging receiver circuit design since the pulse signal is hard for matching and difficult to be filtered out. Its ultra-wide bandwidth may also cause potential interference with the other parts of the entire system in the practical products. Chaotic waveform is another alternative for the waveform optimization. It has a continuous frequency spectrum within a certain

bandwidth. It has been generated by a Colpitts-based topology and demonstrated an efficiency improvement in [80]. For the WPT system applying chaotic waveforms, an appropriate filter should be applied to limit the occupied frequency spectrum and avoid unnecessary radiation in restricted frequency bands. Moreover, the harmonic signal [79], which applies several discrete but harmonically spaced frequencies, is also an excellent candidate for the waveform optimization. Its time-domain waveform achieves a high PAPR and thus high rectification efficiency due to the harmonic relationships among frequencies. Besides, its asymmetric time-domain waveform with high positive voltage peak and low negative voltage peak is of great benefit to get high rectification efficiency within wide power range. However, the desired rectification performance can only be achieved with a set of in-phase harmonics and its performance improves further when more harmonic frequencies are involved. However, the multi-band rectifier design and harmonics' phase arrangements are both difficult tasks that prevent the practical applications of the optimized harmonic waveforms.

Among the various optimized waveforms, the multi-sine waveform would be the most appropriate candidate for the waveform-optimized WPT system design. The involvement of in-phase, narrowly-spaced multi-tone signals

within a single band is defined as the “multi-sine” signal, which is commonly used in orthogonal frequency division multiplex (OFDM) communication systems. For its application in the waveform-optimized WPT systems, the multi-sine signal contributes to the rectifiers’ RF-DC efficiency improvement and it can be easily incorporated into the conventional WPT systems without further circuit amendments. The synthesized multi-sine waveform with high PAPR is theoretically proven to have significant efficiency improvement [77] over the traditional CW excitations with the same average power. Its nonlinear rectifier behaviors have been investigated and a mathematical model for the multi-sine waveform is presented in [83] to evaluate its efficiency improvement effect with various configurations. Besides, its efficiency improvement has also been demonstrated in extending the reading range of the commercial RFID tags as shown in [81][82][84].

To analyze its efficiency improvement mechanism in detail, Fig.2.6 illustrates the rectification process of a high-PAPR signal and demonstrates its efficiency improvement mechanism over the traditional CW sine signal. As can be seen in Fig. 2.6(a), CW sine signal has a uniform voltage amplitude while the multi-sine waveform has a non-uniform voltage waveform with periodic peaks in the time domain. For the CW signal rectification, a minimum

voltage amplitude is required to switch on the rectifier since the rectifier functions only when the voltage across the diode keeps beyond its threshold barrier as analyzed in section 2.2.4. In contrast, the high periodic peaks of the multi-sine signal would only intermittently switch on the rectifier. According to its rectification mechanism, these peaks can overcome the diode threshold barrier more efficiently than the uniform CW signal and the output capacitor is charged to a higher output with increased DC component as shown in Fig. 2.6. Therefore, by applying the multi-sine waveform, its output DC components would be higher than that of a CW signal input with the same average power.

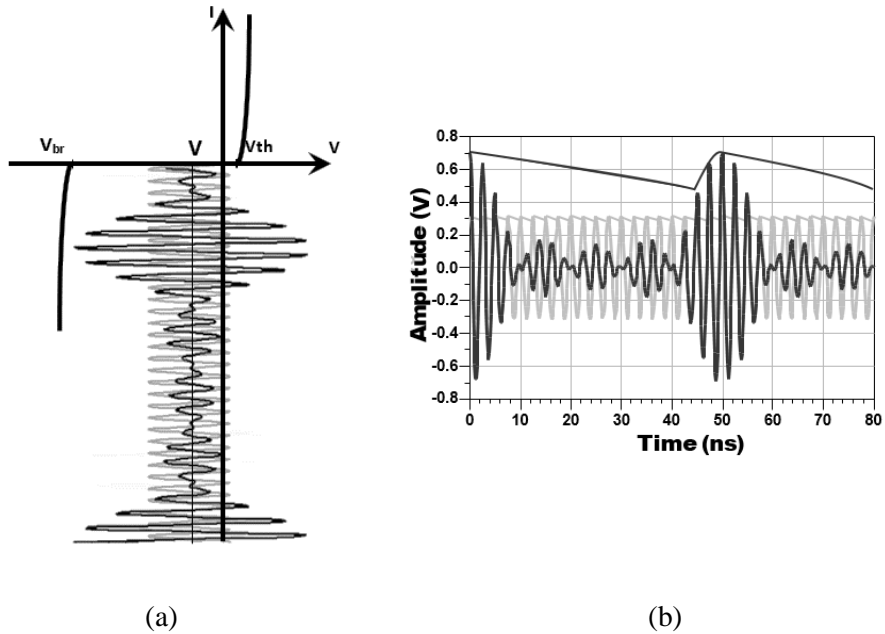


Figure 2.6. (a) Diode's rectification process with CW and multi-sine waveforms. (b) Multi-sine waveform and filtered waveform at the output of receiver

In general, it can be concluded that the waveform optimization would be a good approach contributing to the rectification efficiency improvement with

the unconventional high PAPR waveforms. Various waveforms are investigated with their pros and cons. The multi-sine waveform has been analyzed in detail and been selected as an appropriate candidate for the high efficiency in-vivo WPT system. Detailed investigations on its optimal configurations and solutions to its early breakdown problem will be addressed in chapter 4 and 5, respectively.

2.3 Tissue Effects Consideration

The implantation considerations of the IMDs should not be ignored after the complicated device development. After the implantation, the IMD should be fully functional and cause no harm to the surrounding tissue as well. Two potential risks should be taken into considerations: 1) infections caused by improper interactions with the surrounding tissue [85]; 2) High radiation absorption and related body temperature increase [47][48]. Considerations to avoid the potential risks have been conducted from the following two aspects.

2.3.1 Biocompatible Coating

In the implantable bioelectronics devices, the lumped components and copper wires exposed to the tissue may cause the systemic toxicity that possibly impairs the nervous or immune system of human body. Moreover, the systemic reaction to the external implants is generally distant from the point of

contact of the medical device. Therefore, it is difficult for the patients and doctors to diagnose the implanted medical devices as the source of the toxic reaction.

Therefore, the consideration on devices' biocompatibility has always been viewed as a critical standard in the development of safely implanted medical devices. The biocompatible property is commonly defined [85] as “the quality of being compatible with the living tissue or a living system by not being toxic or injurious and not causing immunological rejection”. It is tested to determine the potential toxicity resulting from contact with a material or medical devices.

In order to guarantee a safe implantation, biomaterial coating has been acting as an increasingly important role in improving the biocompatibility of the implantable bioelectronics. Unique requirements exist for the materials covering the implanted devices, especially in the applications that devices would temporarily contact or permanently be implanted in a human body. The sterilized devices and the biocompatible material need to meet the basic biocompatibility requirements defined by the ISO 10993 standards [86], which is to be nontoxic, non-chromogenic, non-carcinogenic, non-antigenic and non-mutagenic. The properties of the selected biocompatible materials determine its interaction with proteins in the biological environment and subsequently

the interaction with the cells and tissues. A proper selection of the biocompatible materials encourages positive wound healing and the ignorance of biocompatibility or inappropriate material selection may cause slow healing process, infection and even the failure of implantation.

Polydimethylsiloxane (PDMS) is the most commonly used material for biocompatible coating for the bioelectronics devices. It is optically clear, inert, non-toxic and non-flammable. For its interaction with the RF design of the implantable devices, the coated PDMS has a mass density of 0.970 g/cm^3 and thermal conductivity of $0.15 \text{ W/m}\cdot\text{K}$ and dielectric constant of 2.8 [87].

2.3.2 Electromagnetic Exposure Safety Consideration

Besides the biological responses with the surrounding tissue, the absorption of the radiated EM energy by the tissue is another important consideration. The absorption not only leads to the path loss of the energy delivered to the implanted device but also does harm to the human tissue. In order to guarantee patients' safety, an index of specific absorption rate (SAR) is defined and evaluated in both near-field [88][89] and far-field [47][48] WPT. It is the measurement of the energy ratio that is absorbed by the human body when exposed to radio frequency electromagnetic fields. It is defined as the power absorbed per mass of tissue and has the unit of watts per kilogram (W/Kg).

The index SAR is usually evaluated over a small sample volume (typically 1g or 10g of tissue) and is defined by equation (2.12).

$$SAR = \frac{1}{V} \int_{sample} \frac{\sigma(\mathbf{r})|E(\mathbf{r})|^2}{\rho(\mathbf{r})} d\mathbf{r} \quad (2.12)$$

As seen in the equation 2.12, σ is the electrical conductivity of the sample tissue, E is the RMS electric field, ρ is the sample density, V is the volume of the sample.

The SAR value is heavily depended on the body position that is exposed to the RF energy since different tissues have rather different dielectric constants and the composition of the tissue varies when the exposed position changes. Table. 2.5 shows the different dielectric constants of different tissue inside a human body [90] at the frequency of 6.78 MHz.

Table 2.5 Electrical Characteristics of Human Tissues at 6.78 MHz

Tissue	Conductivity σ (S/m)	Dielectric Constant ϵ_r	Mass Density ρ (Kg/m ³)
Skin	0.14712	478.4	1010
Fat	0.027775	16.318	920
Muscle	0.6021	233.27	1040
Bone	0.11585	89.923	1850
Blood	1.0673	421.67	1060

With reference to the different tissue properties, their exposure to the RF energy should be limited by the following two standards. The IEEE C95.1 -

1999 standard limits the averaged SAR value over any 1-g cubic tissue to be less than 1.6W/Kg [91]. The IEEE C95.1-2005 standard limits the average SAR value over any 10-g cubic tissue to be less than 2W/Kg [92].

Besides the potential risk of electromagnetic energy absorption, the temperature increase caused by the electromagnetic energy absorption also affects the daily activities of the human body. In order to maintain a stable metabolic activity, the temperature rise of the surrounding tissue should not exceed 1-2 degrees [47].

Chapter 3 Reconfigurable Diode Topology Designs for Wireless Power Transfer with a Wide Power Range

3.1 Introduction

With a comprehensive literature presented in chapter 2, much research has been conducted on the optimizations of each system block. Among all the system blocks, the diodes used in rectifier designs are the critical components in a WPT system. The characteristics of the diode in use largely determine the rectification efficiency. Therefore, tough requirements are raised for the selected diodes to fit for the unconventional transmission waveforms and the complicated application scenarios. When the unconventional optimized waveforms incident into the rectifier, the waveform with high PAPR brings constraints on its operating power range together with its efficiency improvements since the increased peak voltages are more likely to cause the diode to break down. Meanwhile, the diode also suffers from low rectification efficiency under the large dynamic input power range in most misalignment situations like capsule endoscopy [59] and free-moving animals [93] and retro-reflective wireless charging [94], etc.

So far, the performances of the rectifiers in these dynamic scenarios are not satisfactory. It is noted that conventional rectifiers are designed only for a narrow input power range. When applied to the dynamic application scenarios, rectifiers with a wide power range are highly desired. Some recent efforts have been made in order to improve the input power range of the rectifier by switching among different pre-designed topologies [95] for each narrow power range. However, the complicated switches and detectors in this approach would only be applied at a specific frequency and the increase in circuit size would severely limit its practical applications.

Since a major portion of rectifier power loss results from the inappropriate selection of diodes with either a large threshold voltage or low reverse breakdown voltage. Therefore, in this chapter, we propose the component level solutions of both the reconfigurable diode topologies [96] and the iterative reconfigurable topology [97] to enable the independently tuned threshold voltage and reverse breakdown voltage and thus extending the rectifier's input power range. With appropriate configurations, the diode-equivalent reconfigurable topologies are realized with an ultra-low threshold voltage and a large breakdown voltage, which is almost close to the characteristics of an ideal diode. When applied in rectifier designs, it helps to

obtain the desired wide power range in WPT systems and maintain good performance under large power variations. It is also a good practice to configure the topology with a sufficiently high reverse breakdown voltage while its forward threshold voltage is kept. These two desired features of the topologies contribute to increase the rectifiers' power handling ability when the optimized waveforms with high PAPR incident.

3.2 Diode Topologies Design

3.2.1 Topology Behavior Analysis

In a WPT system shown in Fig. 3.1(a), diodes form the rectifier and it plays a major role in receiver circuits to convert the collected RF energy to output DC power for the subsequent circuits. The typical efficiency versus input power of the rectifier is presented in Fig. 3.1(b) and it shows that the high efficiency is valid for only a narrow power range. The efficiency curve monotonically increases with input power in a low power range while drops sharply in a high power range. The explanation and mechanism analysis of these behaviors are derived from the diode's I-V curve and voltage waveform analysis shown in Fig. 3.1(c). As can be seen, the voltage waveform is biased by the output DC voltage V_o and clipped at the threshold voltage V_{th} . The diode is slightly turned on in the low input power range and the on-state power

loss consumes a large portion of the incident power and accordingly achieves a low rectification efficiency. The rectification efficiency would gradually increase when the input power increases. When it goes to the high input power range, large reverse current passes through the diode when its voltage swing exceeds the reverse breakdown voltage V_{br} . The diode suffers a large power loss from breakdown and accordingly its rectification efficiency drops drastically [69].

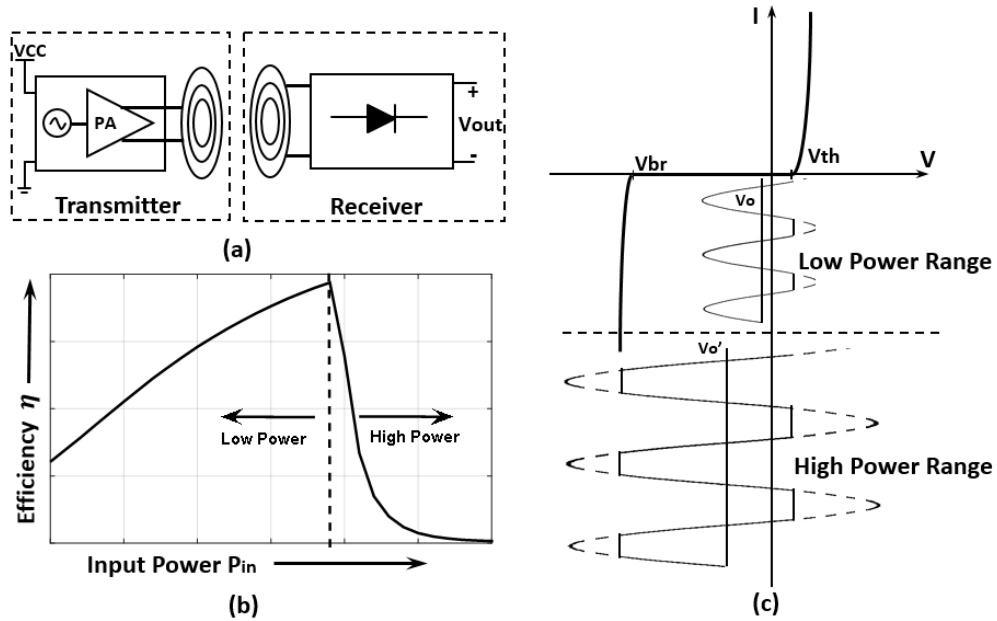


Figure 3.1 (a) WPT system diagram (b) Typical rectifier efficiency curve vs. input power (c) Diode's I-V curve and voltage waveforms across the diode in both low and high power range.

In order to achieve the desired performance of the rectifier, the diode behavior should be fully studied [65][66]. As a nonlinear component, the off-the-shelf Schottky diode is typically modeled as the equivalent circuit [67][68] shown in Fig. 3.2(a). It consists of a series resistor R_s , nonlinear junction

capacitance C_j and nonlinear resistance R_j . These parameters vary nonlinearly with the voltage across the junction V_d . Its junction resistor R_j is, in the ideal cases, assumed to be zero in forward bias and infinite in reverse bias. This nonlinear behavior is reflected in the diode's typical I-V curve in Fig. 3.2(b). For the nonlinear rectification, the incident RF signal is reversely biased by the output DC voltage V_o as shown in the figure.

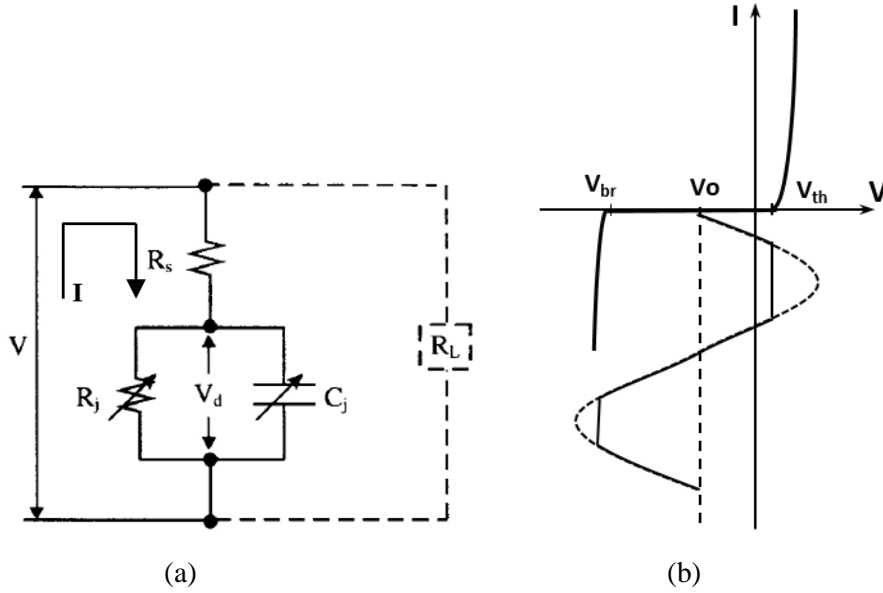


Figure 3.2 (a) Diode's Equivalent Circuit [67]. (b) Diode's typical I-V Curve

Detailed theoretical deduction with a set of closed-form equations for the RF-DC efficiency of the diode is presented in [67][68][69]. Diode's turn-on phase angle θ_{on} and breakdown phase angle θ_{br} are solved with a given V_o , R_s and R_L and thus its RF-DC efficiency is calculated in time-domain expressions as a function of θ_{on} , θ_{br} , diode parameters and V_o .

$$P_{DC} = \frac{V_o^2}{R_L} \quad (3.1)$$

$$P_{loss} = L_{on,R_s} + L_{on,diode} + L_{off,R_s} + L_{off,diode} \quad (3.2)$$

$$+ L_{br,R_s} + L_{br,diode}$$

$$L_{on,R_s} = \frac{1}{2\pi} \int_{-\theta_{on}}^{\theta_{on}} \frac{(V - V_{th})^2}{R_s} d\theta \quad (3.3)$$

$$L_{on,diode} = \frac{1}{2\pi} \int_{-\theta_{on}}^{\theta_{on}} \frac{(V - V_{th})V_{th}}{R_s} d\theta \quad (3.4)$$

$$L_{off,R_s} = \frac{1}{2\pi} \int_{-\theta_{on}}^{2\pi-\theta_{on}} \frac{(V - V_d)^2}{R_s} d\theta \quad (3.5)$$

$$L_{off,diode} = \frac{1}{2\pi} \int_{-\theta_{on}}^{2\pi-\theta_{on}} \frac{(V - V_d)V_d}{R_s} d\theta \quad (3.6)$$

$$L_{br,R_s} = \frac{1}{2\pi} \int_{-\theta_{on}}^{\theta_{on}} \frac{(V + V_{br})^2}{R_s} d\theta \quad (3.7)$$

$$L_{br,diode} = \frac{1}{2\pi} \int_{-\theta_{on}}^{\theta_{on}} \frac{(V + V_{br})V_{br}}{R_s} d\theta \quad (3.8)$$

$$\eta = \frac{P_{DC}}{P_{DC} + P_{loss}} \quad (3.9)$$

As shown in equations (3.1)-(3.9) above, the power losses from both the diode and parasitic resistor R_s in both on/off and breakdown states are analyzed and lead to the RF-DC efficiency calculation. The six portions of the power loss result from several factors in the rectifier design, in which the threshold and breakdown voltages are predominant ones.

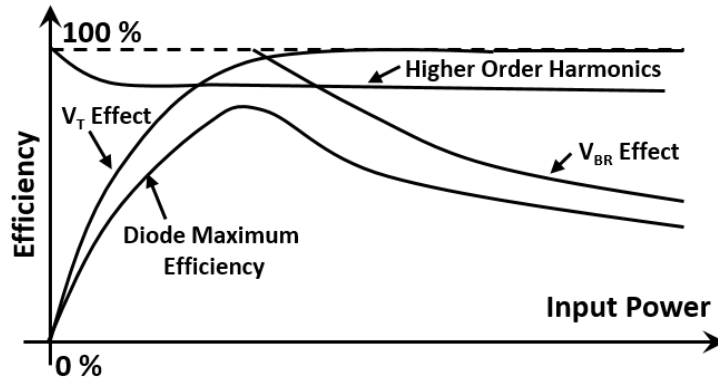


Figure 3.3 Typical RF-DC efficiency curve of the diode with different power losses [67].

As shown in Fig. 3.3, the threshold voltage determines the diode's performance in the low power range while the reverse breakdown voltage affects its performance in the high power range.

A low threshold voltage is highly desired since it allows a sufficiently low power to overcome the Schottky barrier and turn on the diode. Moreover, a low threshold voltage results in less power loss when the diode is on as shown in Eq. (3.4). Similarly, the breakdown voltage determines the diode's performance in a high power range. When a large power RF power incidents into the diode, its large voltage swing at the bias point exceeds the breakdown voltage and shorts the diode with a large reverse current and a substantial power loss as shown in Eq. (3.8). Therefore, a large reverse breakdown voltage is needed for the diode working under a wide power range.

In summary, the effects of threshold and breakdown voltages are shown in Fig. 3.3 as the power losses in low and high power range. For the target of good rectification performance in a wide input power range, an ideal diode should be the one with both low V_{th} and high V_{br} . However, limited by the intrinsic properties of a semiconductor process, a high V_{br} is always associated with a high V_{th} and vice versa. There always has to be a tradeoff between

these two desired properties for a traditional diode. Thus, it would restrain the best performance of a rectifier within the narrow power range.

3.2.2 Reconfigurable Diode Topology Design

Apart from seeking for solutions in an advanced semiconductor process, here a novel reconfigurable diode topology in Fig. 3.4 is presented in this thesis to overcome the process limit and get the ultra-low V_{th} and tunable high V_{br} simultaneously.

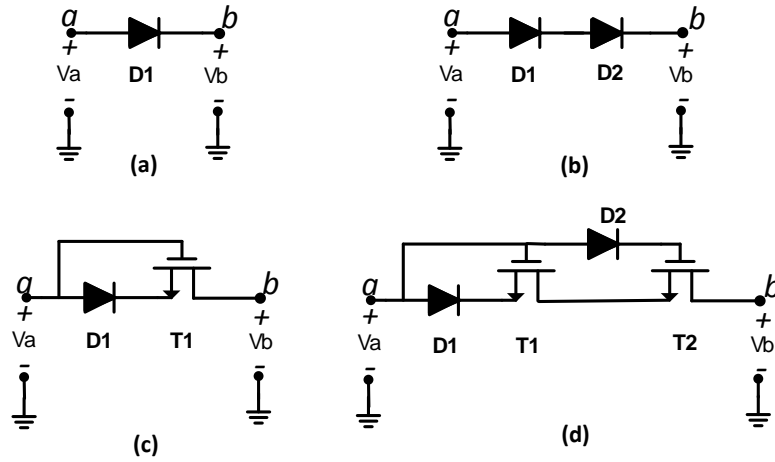


Figure 3.4 Diode Topologies: (a) Single diode (b) diode in series (c) diode with MOSFET (d) Reconfigurable diode topology.

Fig. 3.4 (a) shows a series-mounted single diode as the rectifier. It has a low V_{th} as well as a low V_{br} . Therefore, this rectifier is only suitable for low-input-power applications. Normally, the traditional approach to improve the rectifier's power handling ability is to stack diodes in series as presented in Fig. 3.4(b). It is able to improve the rectifier's power handling ability but at

the sacrifice of the enlarged threshold voltage and degraded efficiency in the low power range. Therefore, it is only suitable for high-input-power WPT applications. Fig. 3.4(c) presents a rectifier design to extend the input power range with a diode and a MOSFET [71]. The topology behaves like a single diode in forward bias while in reverse bias MOSFET T1 turns off to hold the major portion of the voltage between its source and drain. It is a good trial to extend a rectifier's input power range but it only holds a fixed extension range and lacks a generalized theoretical analysis.

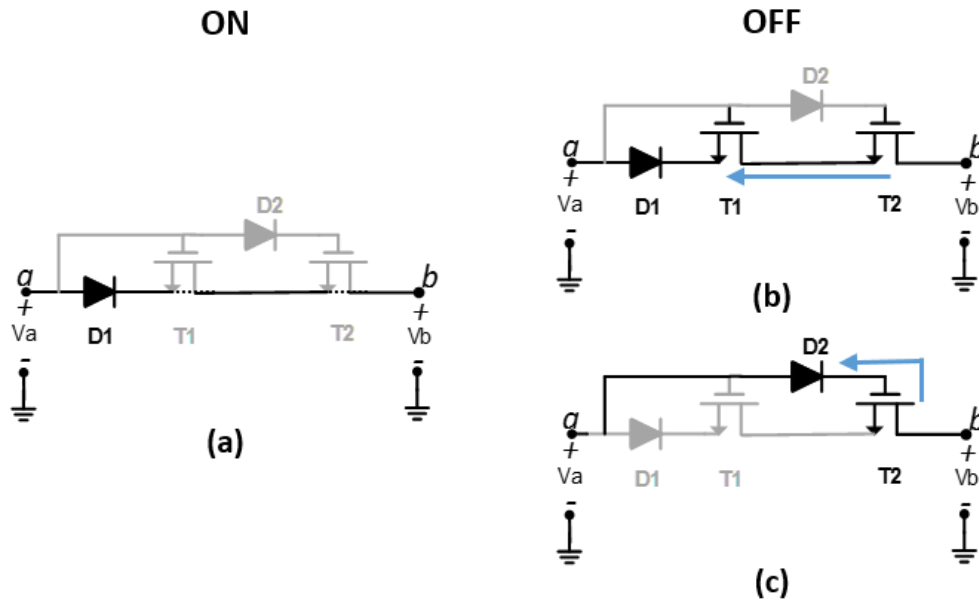


Figure 3.5 Topology analysis of the diode-equivalent reconfigurable topology (a) Equivalent topology in ON state (b) Equivalent topology in OFF state with breakdown channel 1 (c) Equivalent topology in OFF state with breakdown channel 2. Dark black lines indicates the valid circuit portions.

To further improve the diode topology to achieve a generalized solution, Fig. 3.4(d) reveals the proposed reconfigurable diode topology to be

configured to desired V_{th} and V_{br} . The topology consists of 2 Schottky diodes and 2 n-channel depletion-mode MOSFETs, which have a negative turn-on voltage ($V_{gs} < 0$). The detailed topology analysis is presented in Fig. 3.5 above. When the topology in Fig. 3.4(d) is forward biased ($V_a > V_b$), the gate-source voltage of the n-channel MOSFETs are positive and MOSFETs will turn on as an ideal switch. The topology is equivalent to the simple diode D1 and the threshold voltage remains almost the same. When the topology is reversely biased, the transistors switch off first to prevent D1 from breakdown. When the reverse bias voltage keeps increasing, the topology is approaching its breakdown voltage. There are two possible breakdown paths:

- 1) The channel via MOSFET's source and drain breaks down first. The equivalent breakdown voltage is

$$V_{BR} = V_{ds|BR}^{T1} + V_{ds|BR}^{T2} + V_{d|BR}^{D1} \quad (3.10)$$

- 2) The channel via T2's gate and drain breaks down first. The equivalent reverse breakdown voltage is

$$V'_{BR} = V_{gd|BR}^{T2} + V_{d|BR}^{D2} \quad (3.11)$$

where $V_{d|BR}^{Dx}$ represents diode D_x 's reverse breakdown voltage, $V_{ds|BR}^{Tx}$ and $V_{gd|BR}^{Tx}$ refer to the breakdown voltages of drain-source and gate-drain of transistor T_x . Referring to the characteristics of the selected components, the

breakdown path would be via T2's gate and drain in most cases since commonly $V_{BR} \ll V'_{BR}$ with a proper selection of D2.

Therefore, the reconfigurable diode topology in Fig. 3.4(d) achieves an ultra-low threshold voltage V_{TH}^{D1} and an extended breakdown voltage $V_{gd|BR}^{T2} + V_{d|BR}^{D2}$ as shown in Fig. 3.6(a). Besides the V_{br} extension from previous work, the reconfigurable topology also presents a generalized diode topology design with an independently tuned V_{th} and V_{br} , by which a diode is fully customized to its desired characteristics regardless of the semiconductor process constraints.

Moreover, the extended and tunable V_{br} also contributes to the rectifier performance improvement as revealed in its rectification efficiency curve in Fig. 3.6(b). As presented in the figure, the high efficiency portion is largely extended and the breakdown point of the efficiency curve is delayed due to the effects of the V_{br} extension. Further experiment verification has been demonstrated in the following sections.

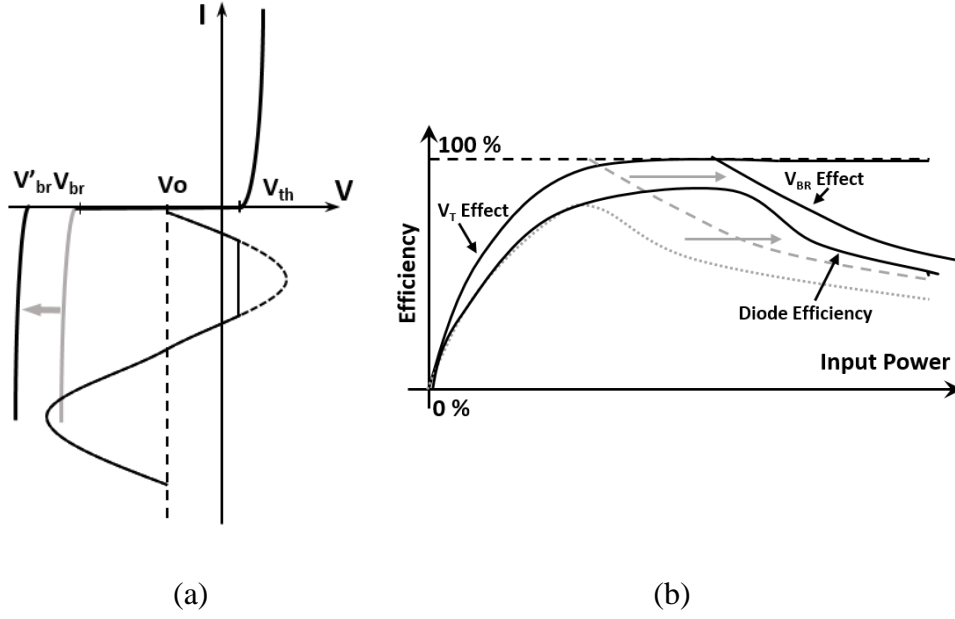


Figure 3.6 Theoretical improvement of the reconfigurable topology over the traditional off-the-shelf diodes.

3.3 Measurement and System Design

In order to demonstrate the performance of the proposed reconfigurable diode topology, Schottky diode (Avago HSMS-2860) and n-channel MOSFET (BF998) are adopted in the design. The topologies are tested and compared in both the I-V curve and the near-field experiment.

3.3.1 I-V Curve Measurement

To present the properties of the diode topologies, fabricated circuits and measured I-V curves are presented in Fig. 3.7.

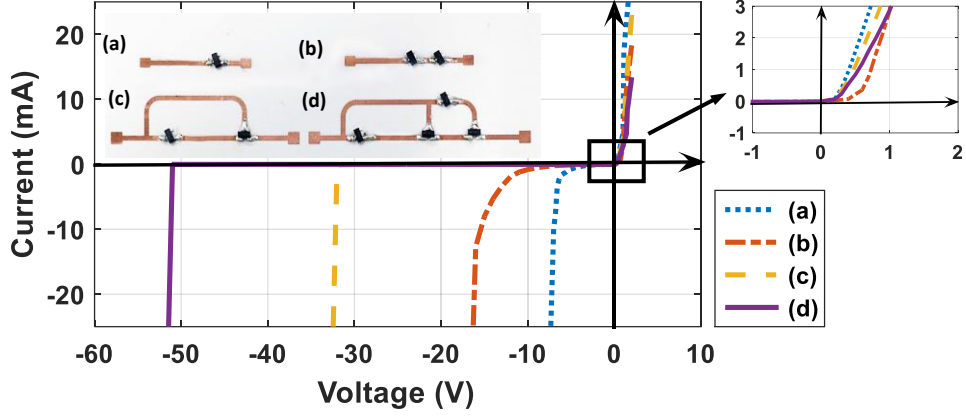


Figure 3.7 Fabricated circuits and measured I-V curves for the proposed diode topologies

As revealed in Fig. 3.7, a single diode has low V_{br} while two diodes in series extend its V_{br} but V_{th} is enlarged as well. Topology in Fig. 3.4(c) obtains an extended V_{br} to -32V and the reconfigurable diode topology in Fig. 3.4(d) can tune its breakdown voltage to an extended -51V with its ultra-low V_{th} almost the same as that of Fig.3.4(a). The reverse leakage currents have been kept at an ultra-low level before breakdown. Table 3.1 summarizes the theoretical and measured breakdown voltages of the topologies above.

Table 3.1 Equivalent Breakdown Voltages Comparison of the Diode Topologies

Topology	Theoretical V_{br} (V)	Measured V_{br} (V)
A	$V_{d BR}$	-7
B	$2V_{d BR}$	-14
C	$V_{ds BR}^{T1} + V_{d BR}^{D1}$	-30
D	$V_{gd BR}^{T2} + V_{d BR}^{D2}$	-49

3.3.2 WPT Experiment Test

In the experiment, an inductive WPT test environment is setup to mimic the large power variation in dynamic application scenarios. Rectifiers are designed by applying the topologies in Fig. 3.4 considering their optimal loads [98] and matching status. The off-the-shelf coils are 10-turn 24uH Litz-wire planar coil with 90 Q-value. The primary and secondary coils keep aligned with 5mm gap in this experiment.

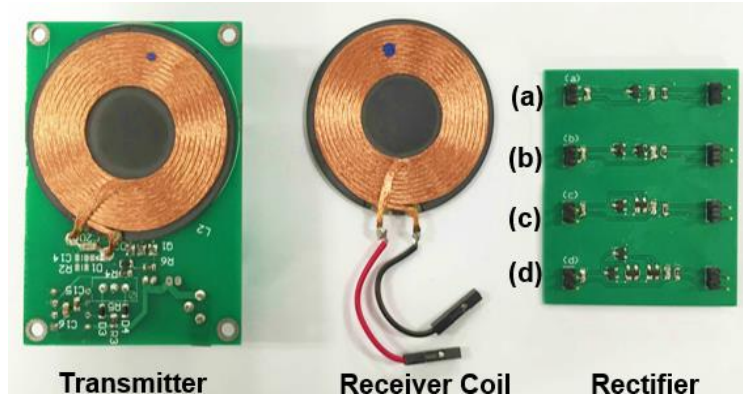


Figure 3.8 Inductive WPT test environment of both the transmitter and the receiver with different diode topologies.

Fig. 3.8 shows the 110 kHz inductive WPT test environment including both the pulse width modulated (PWM) transmitter and the optimized receivers with different diode topologies. The experiment setup is shown in Fig. 3.9 and Fig. 3.10, the PWM transmitter is used to supply the wide-range RF power to mimic the large incident power swing in practical dynamic scenarios. The delivered power can be tuned by changing the PWM duty cycle. The system

efficiency is defined as the output DC power versus the input power from the transmitter. $L_0=L_1=24\mu\text{H}$, $C_0=C_1=100\text{nF}$, $C_2=4.7\mu\text{F}$, $R_L=120\ \Omega$.

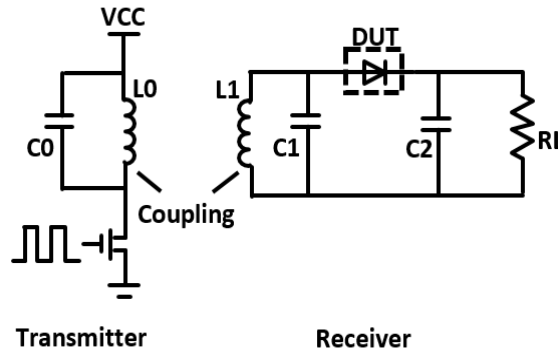


Figure 3.9 Inductive WPT test system diagram and measurement environment.

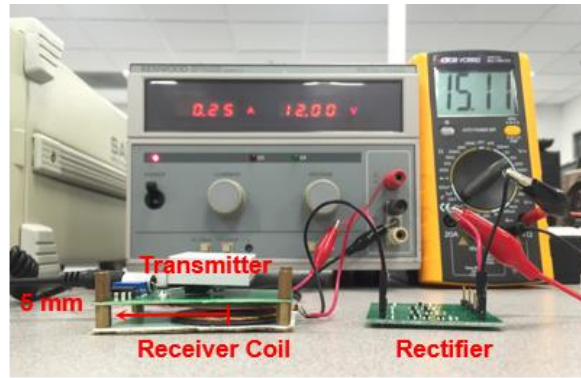


Figure 3.10 Inductive WPT test system diagram and measurement environment.

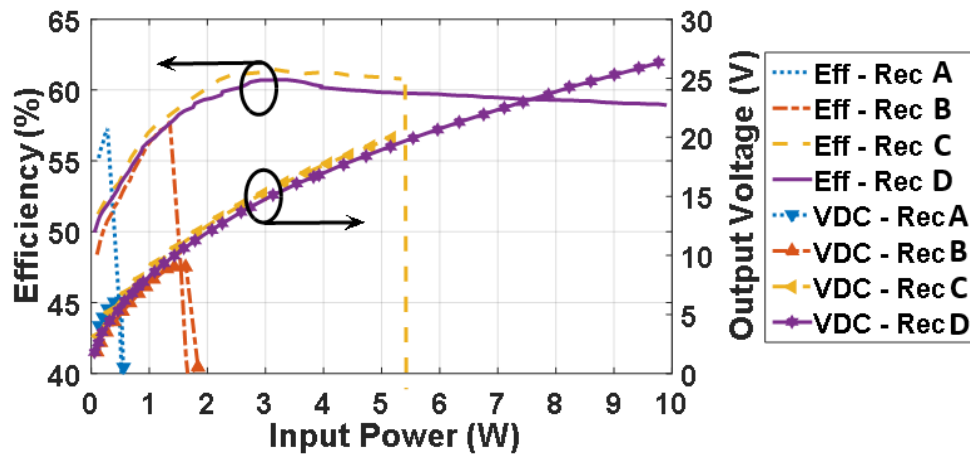


Figure 3.11 Measured system efficiencies and output DC voltages vs. input power of receivers (A)-(D) with diode topologies (a)-(d)

Fig. 3.11 presents the measured system efficiencies and output DC voltage for receivers with different diode topologies (a)-(d) under a wide input power

range. The receiver (A) achieves the highest output voltage and efficiency below 0.5W input power since the rectifier's threshold voltage dominates its performance in a low power range. The receiver (B) has degraded performance since its threshold voltage doubles with the stacked diode. Receivers (C) and (D) have slightly lower efficiency and output DC voltages than the receiver (A) in a low power range due to the MOSFET insertion loss. However, the efficiencies higher than the receiver (B) also indicate the advantage of the proposed topologies over the stacked diode strategy with similar matching status. In a high power range, the diode's breakdown voltage plays a key role in determining system power range. The breakdown of the diode-equivalent topologies would result in the drastic drop of the efficiency curves. When a high input power incidents into the rectifier circuits, large voltage swing applies across the diode. When its reverse peak exceeds the breakdown voltage, large current flows through the diode and causes significant power loss on the diode and therefore resulting in drastic efficiency drop. As can be seen, although performing well in a low power range, the receiver (A) breaks down rapidly when input power increases; the receiver (B) retains its performance in a larger power range, however, with a degraded efficiency. Different from the traditional topologies, the receivers (C) and (D)

maintain good performance in both low and high power levels. The receiver (C) has fixed power handling ability within 5 W input while the receiver (D) with the tuned V_{br} to maintain the high efficiency within the 10W wide input power range.

In summary, the proposed reconfigurable diode topology contributes in designing the rectifier with good performance in a wide input power range, which is the desired property to handle large power variations in practical scenarios. When applied in the near field test setup in Fig. 3.9 and Fig. 3.10, the proposed reconfigurable topology achieves good performance in comparison with the state-of-the-art WPT rectifiers as shown in Table. 3.2 below. As can be seen, [69][95][99] achieve good performance in either a low or high but relative narrow power range. In contrast, the reconfigurable topology can achieve satisfied efficiency over both the low and high power range. It fully utilizes the collected energy when large power variations exist.

Table 3.2 Rectifier Performance Comparison in Wide Power Range

Reference	Device Type	Topology	Pin range for eff > 50%
[95]	GaAs	Rectifiers combination	0.6mW – 1 W
[69]	PCB	Diode in shunt	10mW -50 mW
[99]	CMOS	Diode Bridge	2W-6W
This Work	PCB	Reconfigurable diode topology	>0.1 W- 10 W

3.4 Iterative reconfigurable diode topology

Besides the topology designs above, further development of the reconfigurable diode topology is also considered. According to the topology design and breakdown path analysis presented above, there are two possible approaches [97] to extend the diode-equivalent topology further as shown in the Fig. 3.12 below.

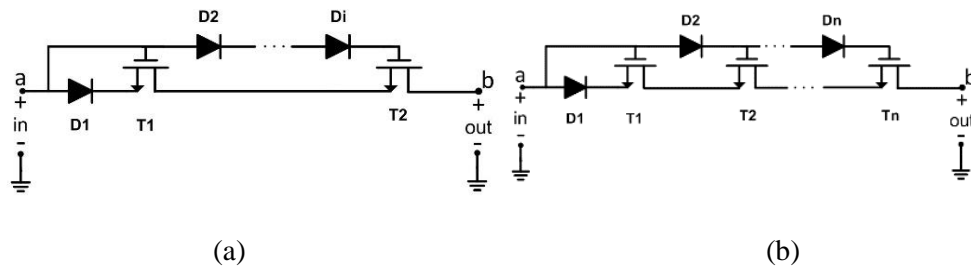


Figure 3.12 Two types of iterative reconfigurable diode topologies.

As shown in Fig. 3.12(a), the power handling ability of the diode topology is further extended by applying additional diodes in breakdown path (2) as analyzed in Eq. (3.11). Since the equivalent reverse breakdown voltage of the

topology is determined by the breakdown path which is firstly achieved when the reverse bias voltage keeps increasing. Assuming n stages are applied in the topology, the two possible breakdown paths are shown below.

- 1) The channel via MOSFET's source and drain breaks down first and the equivalent breakdown voltage is

$$V_{rect|BR} = V_{ds|BR}^{T1} + V_{ds|BR}^{T2} + V_{d|BR} \quad (3.12)$$

- 2) The channel via MOSFET's gate and drain breaks down first and the equivalent breakdown voltage is

$$V'_{rect|BR} = V_{gd|BR} + n \cdot V_{d|BR} \quad (3.13)$$

Referring to the datasheets of both the diodes and the MOSFET, since $V_{rect|BR} \ll V'_{rect|BR}$ when $n \geq 2$, the breakdown path is via T2's gate and drain.

In order to explore the maximum cascade number, the following criterion should be satisfied to switch off T2 successfully before the whole topology breaks down:

$$V_{in} - (n_{max} \cdot V_{d_n}) = V_{th} \quad (3.14)$$

$$V_{in} > V_{gd|BR} \quad (3.15)$$

With equation (3.14) and (3.15), we can derive

$$n_{max} < \frac{V_{gd|BR} - V_{th}}{V_{d_n}} \quad (3.16)$$

Therefore, the maximum iteration n_{max} is

$$n_{max} = \lfloor \frac{V_{gd|BR} - V_{th}}{V_{d_n}} \rfloor \quad (3.17)$$

When the applied stage number is beyond n_{max} , the last transistor $T_{n_{max}}$ cannot switch off and thus the topology breaks down rapidly.

Therefore, the proposed rectifier topology in Fig. 3.12(a) achieves a reconfigurable breakdown voltage as the scenario requires with its low threshold voltage remains.

Similar analysis can be applied to the topology in Fig. 3.12(b), the iteration of the diode-MOSFET unit helps in increasing the reverse breakdown voltage of the entire diode-equivalent topology. The two possible breakdown paths of the topology in Fig. 3.12(b) are shown below.

- 1) The channel via MOSFET's source and drain breaks down first and the equivalent breakdown voltage is

$$V_{rect|BR} = n \cdot V_{ds|BR} + V_{d|BR} \quad (3.18)$$

- 2) The channel via MOSFET's gate and drain breaks down first and the equivalent breakdown voltage is

$$V'_{rect|BR} = V_{gd|BR} + (n - 1)V_{d|BR} \quad (3.19)$$

According to the component characteristics, the breakdown would firstly occur via the channel of the MOSFET's gate and drain when the reverse bias voltage keeps increasing. Therefore, its equivalent breakdown voltage is

$$V_{BR} = V_{gd|BR} + (n - 1)V_{d|BR} \quad (3.20)$$

The entire topology iterates to extend its reverse breakdown voltage as long as the last MOSFET is able to switch off. For the successful iteration, the following requirements should be satisfied

$$V_{in} - (V_{d_2} + \dots + V_{d_n}) = V_{gs|TH} \quad (3.1)$$

$$V_{in} - (V_{d_2} + \dots + V_{d_{n-1}}) > V_{gd|BR} \quad (3.22)$$

$$V_{gs|TH} + V_{d_n} > V_{gd|BR} \quad (3.23)$$

Referring to the datasheets of all the selected components, Eq. (3.23) is satisfied regardless of the number of iterative stages with an appropriate component selection. In this case, the iterative topology in Fig. 3.12(b) is able to apply to any stages with its breakdown voltage configured to the sufficient value based on application requirements. In summary, the proposed topology obtains both the ultra-low threshold voltage as $V_{D1|TH}$ and tunable breakdown voltage as $V_{gd|BR} + (n - 1)V_{d|BR}$ regardless of the semiconductor constraints.

To summarize, both the diode topologies can iterate to extend its equivalent breakdown voltage to achieve better power handling ability. Meanwhile, the topology in Fig. 3.12(b) holds an unlimited extension while that in Fig. 3.12(a) is only able to extend to stages below n_{max} . However, the topology in Fig. 3.12(a) has less power loss than its counterpart in Fig. 3.12(b) since less components are involved in the design. In brief, the two topologies

both have their own advantages and can be applied in the rectifier designs based on the application scenarios.

3.5 Conclusion

In conclusion, chapter 3 presents both the reconfigurable diode topology and the iterative reconfigurable diode topology to increase its power handling ability. The proposed diode-equivalent topologies enable the independently tuned threshold voltage and the reverse breakdown voltage. With an appropriate configuration, the desired properties close to the ideal diode can be obtained regardless of the semiconductor constraints. These reconfigurable diode topologies are highly preferred in the WPT system with the optimized high PAPR waveforms. When the properly configured topologies are applied, it effectively solves the early breakdown problem as well as maintains the high RF-DC conversion efficiency. Therefore, high efficiency within an extended operating power range would be achieved in the WPT system with optimized waveforms. The topologies presented in Chapter 3 provide a practical component level design to solve the current challenges for the waveform-optimized WPT system and push the waveform-optimized WPT design one step forward the practical applications.

Chapter 4 Advanced System Block Designs for High-Efficiency Wireless Power Transfer

A completed WPT system is built up by several crucial circuit blocks including the coil pairs and the receiving circuits. In this chapter, the research work on both coil system and rectifier parts are presented for the waveform-optimized WPT system design. Firstly, a rapid design approach based on the concise mathematical model is proposed to efficiently design the MR-WPT system. It is also an excellent strategy to increase the system robustness in complicated environments by tracking the maximal efficiency with the proposed algorithms. For the rectifier design, an efficiency improvement has been observed by applying the multi-band waveforms. Different rectification approaches and design considerations for the multi-band waveforms are further investigated in this chapter. A dual-band rectifier with extended power range (EPR) is presented to study the multi-band waveforms' efficiency improvement mechanism and its performance in various input situations. Meanwhile, the early breakdown of the rectifier occurs with the multi-band waveform simultaneous incidence. The problem has been addressed and

solved in this chapter by applying the reconfigurable diode topology in the prior chapter.

4.1 Rapid Design Approach of Optimal Efficiency Magnetic Resonant Wireless Power Transfer System

4.1.1 Introduction

As the analysis in chapter 2 indicates, WPT technique has been treated as an excellent choice to replace the power wire and increase the mobility of the state-of-the-arts electronic devices. To design a WPT system, one of the most critical factors for performance evaluation is its power transfer efficiency. Different from the traditional inductive WPT, the optimal power transfer efficiency of an MR-WPT is achieved at a certain distance. In order to conduct the optimization, investigations on the behavior of the MR-WPT system have been done [46][50] and mathematical models are presented to depict the system and find its optimal configurations. However, in most cases, complicated closed-form equations are given to model the MR-WPT system but it lacks a clear and concise guideline to obtain the optimal efficiency of the MR-WPT system rapidly. Without the theoretical instructions, the random optimizations in CAD software (CST, HFSS, etc.) are less efficient and time-consuming.

Therefore, in this section, a rapid design approach is presented to provide a theoretical instruction and guideline to rapidly obtain the optimal configurations and maximum efficiency of a given MR-WPT system. With a concise MR-WPT system model, a rapid design procedure is presented to achieve the optimal efficiency efficiently. Both the CST simulation and an MR-WPT prototype demonstration prove its validity and effectiveness.

4.1.2 MR-WPT System Model Analysis

A typical MR-WPT system consists of four coils: drive, primary, secondary and load coil (or coils 1-4), as shown in Fig. 4.1. Drive and primary coils form the transmitter circuits while the receiver consists of secondary and load coils. All the four coils are tuned at resonance. When the current flow from the power source to the drive coil, it generates an oscillating magnetic field and the field subsequently excites the primary coil, which is an LCR (inductor-capacitance-resistor) tank with a coil inductor, a resonant capacitor and a parasitic resistor. The small parasitic resistor in the LCR tank results in the high quality factor (Q) of the primary coil and thus generating significant magnetic field oscillation. Likewise, the large magnetic field oscillation is easily received by the high Q secondary coil at the receiver side and the RF energy is then coupled to the load for rectification and powering the load.

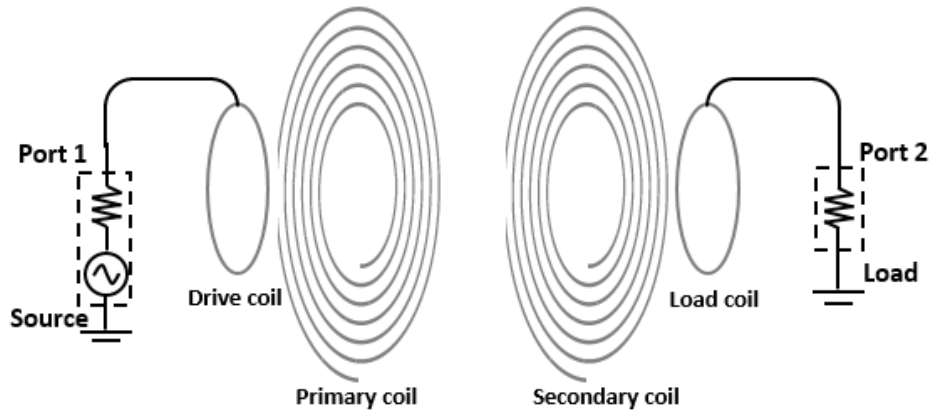


Figure 4.1 Magnetic resonant wireless power transfer system prototype

Unlike the two-coil inductive WPT system, of which the power transfer efficiency curve is monotonically decreasing with the coil separation distance, the power transfer efficiency curve of the MR-WPT system is separated into three regions: over-coupled, critically-coupled and under-coupled regimes. In the over-coupled region, the magnetic flux is delivered to the receiver side more than required and it leads to the frequency splitting [50] and the efficiency decrease at the operating frequency. In the under-coupled region, the transferred magnetic flux is less than required and accordingly results in the efficiency drop as well. As the transition point between these two regions, the critically coupled point corresponds to the largest distance with the maximum transfer efficiency. Therefore, the MR-WPT system obtains its optimal performance when tuned at its critically coupled point.

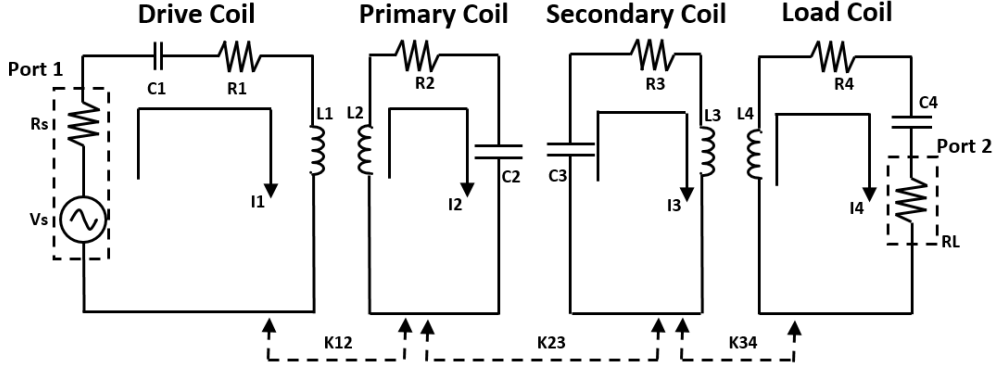


Figure 4.2 System Diagram of Magnetic Resonant Wireless Power Transfer

An equivalent model for the MR-WPT system is presented in Fig. 4.2 and its mathematical description [50] is derived from Kirchhoff's law as equation (4.1)-(4.4) show. The cross coupling coefficients k_{13} , k_{14} , k_{24} are negligible for the algorithm simplicity.

$$I_1 \left(R_s + R_1 + j\omega L_1 + \frac{1}{j\omega C_1} \right) + j\omega I_2 M_{12} = V_s \quad (4.1)$$

$$I_2 \left(R_2 + j\omega L_2 + \frac{1}{j\omega C_2} \right) + j\omega (I_1 M_{12} - I_3 M_{23}) = 0 \quad (4.2)$$

$$I_3 \left(R_3 + j\omega L_3 + \frac{1}{j\omega C_3} \right) + j\omega (I_4 M_{34} - I_2 M_{23}) = 0 \quad (4.3)$$

$$I_4 \left(R_L + R_4 + j\omega L_4 + \frac{1}{j\omega C_4} \right) + j\omega I_3 M_{34} = 0 \quad (4.4)$$

For a compact representation, the equations (4.1)-(4.4) can be interpreted in the matrix (4.5) to model the MR-WPT system and shows the relationship between the source voltage and the currents flow through each coil.

$$\begin{bmatrix} Z_1 & j\omega M_{12} & 0 & 0 \\ j\omega M_{12} & Z_2 & j\omega M_{23} & 0 \\ 0 & j\omega M_{23} & Z_3 & j\omega M_{34} \\ 0 & 0 & j\omega M_{34} & Z_4 \end{bmatrix} \begin{bmatrix} I_1 \\ I_2 \\ I_3 \\ I_4 \end{bmatrix} = \begin{bmatrix} V_s \\ 0 \\ 0 \\ 0 \end{bmatrix} \quad (4.5)$$

The parameter Z_x presents the coil impedance in (4.6)-(4.9) and the mutual inductance M_{xy} between coil x and coil y with the inductance value L_x, L_y is

shown in (4.10). The power transfer efficiency η is defined in Eq. (4.11) as the ratio of power delivered to the load P_{out} to the total source power input P_{in} to the system.

$$Z_1 = R_s + R_1 + j\omega L_1 + \frac{1}{j\omega C_1} \quad (4.6)$$

$$Z_2 = R_2 + j\omega L_2 + \frac{1}{j\omega C_2} \quad (4.7)$$

$$Z_3 = R_3 + j\omega L_3 + \frac{1}{j\omega C_3} \quad (4.8)$$

$$Z_4 = R_L + R_4 + j\omega L_4 + \frac{1}{j\omega C_4} \quad (4.9)$$

$$M_{xy} = \frac{\mu_0}{4\pi} \iint \frac{d\mathbf{l}_x \cdot d\mathbf{l}_y}{|\mathbf{r}_y - \mathbf{r}_x|} = k_{xy} \sqrt{L_x L_y} \quad (4.10)$$

$$\eta = \frac{P_{out}}{P_{in}} = |S_{21}|^2 \quad (4.11)$$

4.1.3 Rapid Design Approach

To compute the maximum power transfer efficiency, analysis from the circuit perspective is applied in this section. As shown in Fig.4.3, the latter coil is modeled as an equivalent load for the former coil with the principle of power sharing applied. The load coil is modeled as reflected impedance on the secondary coil in equation (4.13) and so on for the rest coils as shown in equation (4.12)-(4.14). Each coil should be in resonance and the reflected impedance are shown in Z'_x below:

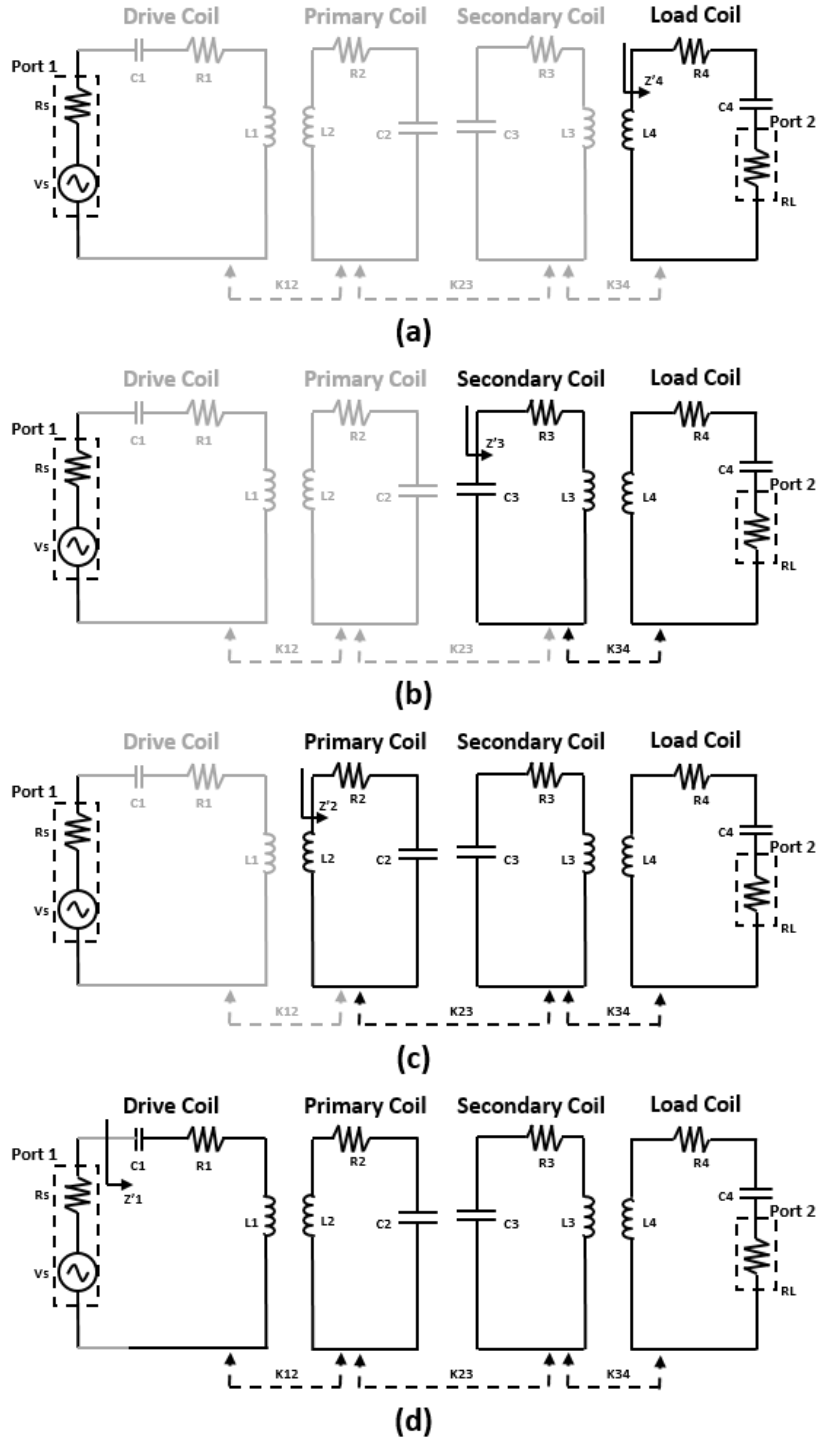


Figure 4.3 System Diagram of Magnetic Resonant Wireless Power Transfer

Since the coils have relatively very small resistances and in most cases

$K_{34}^2 \cdot \frac{L_4}{C_3} / R_L \gg R_3$ is guaranteed in an inductance-based system, the reflected

impedance Z'_x is simplified as shown in Eq. (4.13) and Eq. (4.14).

$$Z'_4 = j\omega L_4 + \frac{1}{j\omega C_4} + R_L + R_4 \approx R_L \quad (4.12)$$

$$\begin{aligned} Z'_3 &= j\omega L_3 + \frac{1}{j\omega C_3} + R_3 + \frac{(\omega M_{34})^2}{R_L} \\ &= R_3 + \frac{(\omega K_{34} \sqrt{L_3 L_4})^2}{R_L} = R_3 + \frac{K_{34}^2 \frac{L_4}{C_3}}{R_L} \approx \frac{K_{34}^2 \frac{L_4}{C_3}}{R_L} \end{aligned} \quad (4.13)$$

$$\begin{aligned} Z'_2 &= j\omega L_2 + \frac{1}{j\omega C_2} + R_2 + \frac{(\omega M_{23})^2}{Z'_3} \\ &= R_2 + \frac{(\omega K_{23} \sqrt{L_2 L_3})^2}{K_{34}^2 \frac{L_4}{C_3} / R_L} = R_2 + \frac{K_{23}^2 \frac{L_3}{C_2}}{K_{34}^2 \frac{L_4}{C_3} / R_L} \approx \frac{K_{23}^2 \frac{L_3}{C_2}}{K_{34}^2 \frac{L_4}{C_3}} R_L \end{aligned} \quad (4.14)$$

By such analogy, the equivalent impedance Z_{in} equals to

$$Z_{in} = Z'_1 \approx \frac{K_{12}^2 \cdot \frac{L_2}{C_1} \cdot K_{34}^2 \cdot \frac{L_4}{C_3}}{K_{23}^2 \cdot \frac{L_3}{C_2} \cdot R_L} = \frac{K_{12}^2 \cdot K_{34}^2 \cdot \frac{L_4}{C_1}}{K_{23}^2 \cdot R_L} \quad (4.15)$$

Based on the maximum power transfer principle, the optimal power transfer efficiency is only obtained when the equivalent impedance equals to the conjugated source impedance as shown in Eq. (4.16). In most cases, the source impedance is 50 Ohm.

$$Z_{in} = \frac{K_{12}^2 \cdot K_{34}^2 \cdot \frac{L_4}{C_1}}{K_{23}^2 \cdot R_L} = \frac{M_{12}^2 \cdot M_{34}^2 \cdot \omega_o^2}{M_{23}^2 \cdot R_L} = R_S^* \quad (4.16)$$

For a given set of coils, Eq. (4.17) is applied to connect the coupling coefficient k_{xy} with the coils' physical parameters. D_{xy} is the distance between the aligned coils x and y. N_x, N_y and r_x, r_y are the turns and radii of the coils x and y, respectively.

$$\begin{aligned} k_{xy} &= \frac{\mu_o N_x N_y \sqrt{r_x r_y} \beta}{\sqrt{L_x L_y}} \int_0^{2\pi} \int_0^{2\pi} \frac{\cos(\phi_x - \phi_y) d\phi_x d\phi_y}{\sqrt{1 - 2\beta \cos(\phi_x - \phi_y)}} \\ \beta &= \frac{r_x r_y}{D_{xy}^2 + r_x^2 + r_y^2} \end{aligned} \quad (4.17)$$

Therefore, the optimal coil distance configurations to obtain the maximum power transfer efficiency are easily achieved by two steps:

(i) Referring to Eq. (4.17), calculate the coupling coefficients k_{xy} with the coil characteristics and their distance D_{xy} .

(ii) Based on Eq. (4.16), select k_{xy} values to guarantee the maximum power transfer efficiency.

4.1.4 Experiment Result and Analysis

To validate the proposed design approach, a 6.78 MHz MR-WPT system under the A4WP (Alliance for Wireless Power) protocol is rapidly designed. The coil geometries in the system are shown in Table 4.1. Given the project's constraints, the transmitter-receiver distance (D_{23}) is set to be at least 50 mm to satisfy most wireless transmission requirements and meanwhile the distance between coils 3-4 is fixed at 5 mm to miniaturize the receiver.

Table 4.1 Coil Characteristics in the MR-WPT system

Coil	N	r(mm)	L(uH)	C(pF)	R(Ohm)
Drive Coil	2	50	1.096	502.9	0.261
Primary Coil	20	50	82.59	6.67	11.36
Secondary Coil	10	20	5.48	100.6	0.926
Load Coil	2	20	0.352	1567.3	0.096

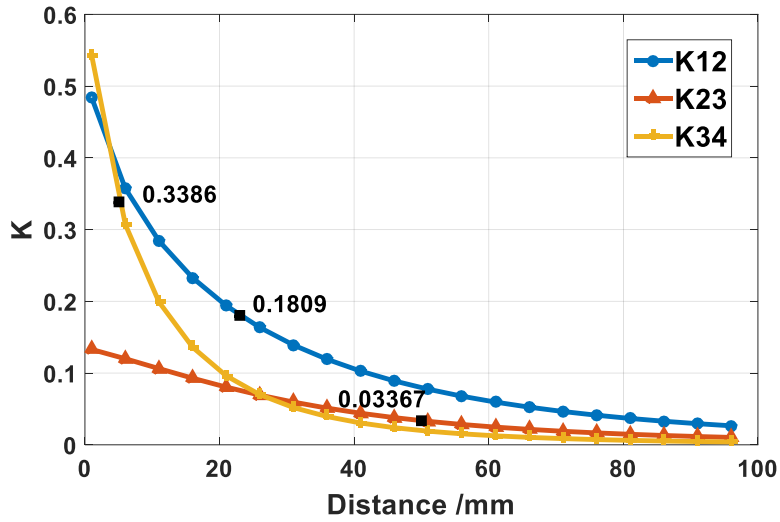


Figure 4.4 Coupling Coefficient k_{xy} vs. distance between coil x and y.

Fig. 4.4 shows the curves of coupling coefficient with coil distance. With the practical constraints, the optimal K_{12} can be calculated from (4.16). An appropriate set of coupling coefficients $K_{12}=0.1809$, $K_{23}=0.03367$, $K_{34}=0.3386$ is selected and the MR-WPT system with its optimal efficiency is accordingly obtained with the physical parameters $D_{12}=23$ mm, $D_{23}=50$ mm, $D_{34}=5$ mm.

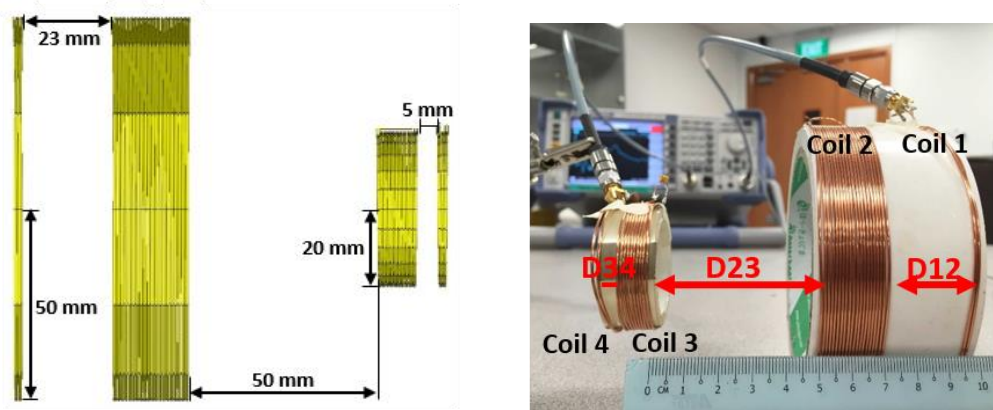


Figure 4.5 The MR-WPT system performance verification with CST Simulation and the prototype Experiment.

CST simulation and the prototype demonstration are presented and measured to verify the design. Both the CST simulation and measurement are

presented in Fig. 4.5. In the experiment setup, R&S ZVL network analyzer is used as shown above.

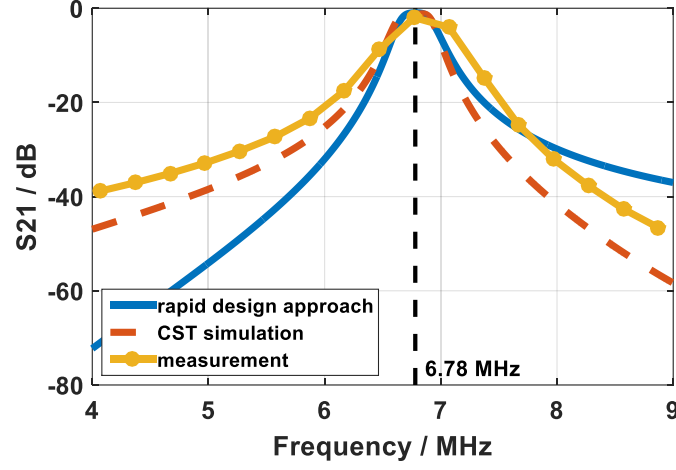


Figure 4.6 The MR-WPT system performance measurement with the Rapid Design Approach, CST Simulation and prototype experiment.

Table 4.2 Result Comparison and Analysis at 6.78 MHz

Parameter	Rapid Design Approach	CST Simulation	Prototype Measurement
S21 (dB)	-0.962	-1.095	-1.19
Efficiency (%)	80.1	77.4	76.1

The CST simulation and prototype measurement of the optimized MR-WPT system are revealed in both Fig. 4.6 and Table 4.2. Fig. 4.6 lists the S21-curves of the rapid design approach, the CST simulation and the prototype measurement. The highest transmission efficiency of 76.1% is achieved in the MR-WPT system at the designed resonant frequency of 6.78 MHz. The system efficiency is calculated by equation (4.11) and compared in Table 4.2. A good coherence is presented among these three approaches but with different computation burdens. Although there exists a bit deviation in the

lower out-of-band frequency range due to the simplification of the coil parasitic parameters and negligibility of the coupling coefficient k_{13} , k_{14} , k_{24} , the in-band accuracy still can be guaranteed with a much lower computation burdens.

Different from the traditional random optimization in the CAD software, the proposed rapid design approach achieves the optimal efficiency more efficiently. It fits the internal operating mechanism of the MR-WPT system and realizes the optimization only in two simple steps. It provides a simple and intuitive understanding of the MR-WPT system and significantly reduces the computation burden of optimization in designing such an MR-WPT system with the optimal efficiency.

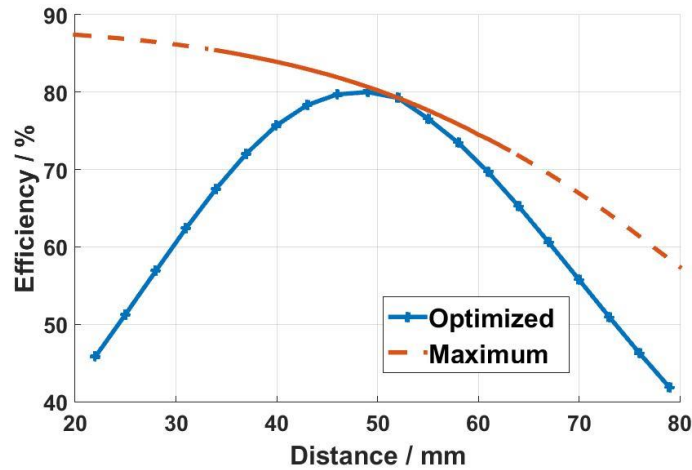


Figure 4.7 Maximum Efficiency Tracking with the Varying Transmitter-receiver Distance D_{23}

Moreover, the proposed rapid design approach also serves as an excellent optimal efficiency tracking strategy. In various complicated situations such as

the biomedical implants, the transmitter-receiver distance is not always fixed. In order to keep the optimal efficiency of the MR-WPT system, the distances D_{12} and D_{34} should be adjusted accordingly as indicated in the equations (4.16) and (4.17). Since the receiver should be kept compact in most cases, the optimal efficiency tracking is mainly realized by tuning the distance D_{12} . Fig. 4.7 shows the maximum efficiency tracking curve as the transmitter-receiver distance D_{23} varies. As is shown, the theoretical maximum efficiency decreases when the transmitter and the receiver separates. The solid part of the curve shows the feasible maximum system efficiency when D_{12} is within the tuning range of 10 mm - 40 mm while the dash part indicates the theoretical maximum efficiency with less practical D_{12} configurations. Based on the curve analysis, the MR-WPT system with varying transmitter-receiver distances is able to obtain its theoretical maximum efficiency by applying the proposed tracking strategy.

4.1.5 Effects of Biological Tissue

In the previous sections, the rapid design approach is successfully verified in air and the proposed MR-WPT system presents a good power transfer efficiency. However, further investigation needs to be done when it applies to

the bio-implants. The effects of the biological tissues on the implanted coils are explored and discussed in this section.

As mentioned in section 2.2.2, coil resonance is the predominant operating mechanism of the MR-WPT system. The influence of the non-resonant objects is nearly negligible. The magnetic resonant wireless power transfer system could only be influenced by the extraneous objects with significant magnetic properties since the near-field regime of the coil is majorly magnetic. Only the close proximity of large areas of metallic structures would affect the performance of the proposed coil system.

For the implanted coils surrounded by the biological tissues, the coils have the inductances that are quite close to that in air since the permeability of the biological tissue is almost the same as that of the free space. However, the surrounding tissues would, to some extent, affect the coils' parasitic capacitance with its high dielectric constants. The implanted coils with the increased parasitic capacitances may result in a little resonant frequency shift and a lower system Q-value. Since the implanted coils in most cases have small size and thus small inductance values, the resonant capacitance for working at low frequency would be large and the small value variations

brought by the surrounding tissue environment would not cause great changes for the design with an acceptable tolerance.

In order to verify the analysis above, simulation is implemented based on the phantom model in CST and in-vitro experiment is conducted with minced pork to mimic the biological tissue environment. The proposed MR-WPT system design is put into the biomedical application scenario to investigate its performances. As shown in Fig. 4.8, the receiving coils in the CST simulation are implanted into the muscle phantom with 50 mm underneath the surface. In the in-vitro experiment, the receiving coils are surrounded by the minced pork and RF power is delivered from the transmitter coils to the receiver coils with 50 mm gap with the minced pork as the mimicked biological tissue.

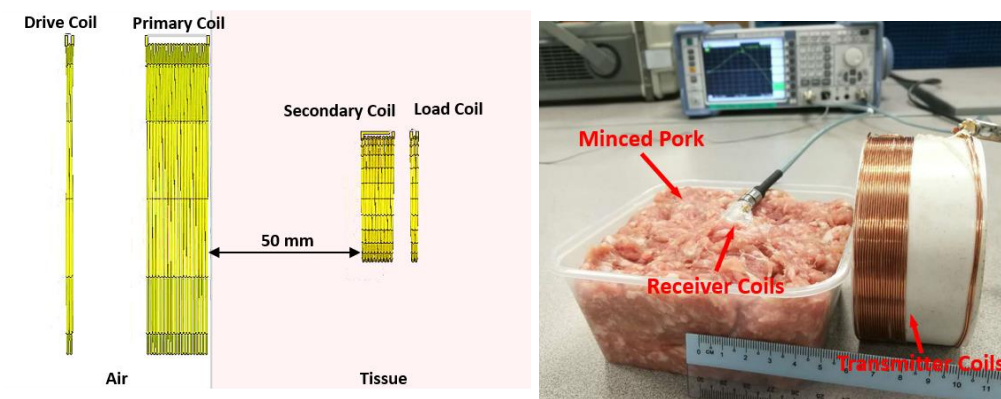


Figure 4.8 In-phantom Simulation and in-vitro experiment of the MR-WPT system

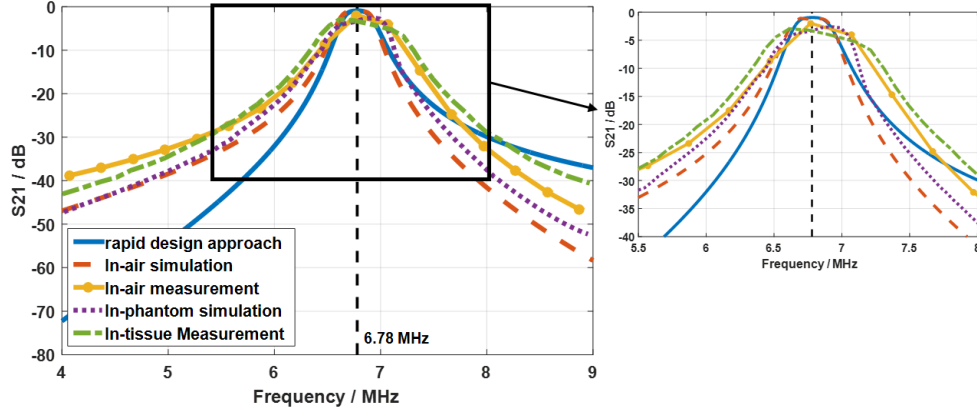


Figure 4.9 MR-WPT system performance verification in phantom model and in minced pork.

The experiment results are shown in Fig. 4.9 above. As can be seen, there is little variation of the achievable maximal efficiency, which indicates that the involvement of the biological tissue does not bring much power loss during the power transfer. Besides, the little frequency shift also verifies the influence of the biological tissues on the parasitic capacitances.

Besides the minimal influence on the coil system performance, the predominant magnetic near-field also introduces a safe alternative for the wireless power transfer through the biological tissue inside human body. As is known, with the non-metallic properties, human body can sustain strong magnetic fields without suffering from any potential risks. Take the magnetic resonance imaging (MRI) system as an example, the magnetic field applied in the system is around 1T and it has been widely and safely used for disease detection. While, the magnetic field applied is just around 10^{-6} T to wirelessly delivering power to the implantable medical devices.

In general, the in-phantom experiment and in-vitro experiment demonstrate that the magnetic resonant wireless power transfer system works well both in air and inside the environment surrounded biological tissues. With the negligible variation on its performance, the magnetic resonant wireless power transfer would be a good candidate for the biomedical applications and the proposed rapid design approach can also be applied in the WPT system design for bio-implants uses.

4.1.6 Technology Comparison

From the perspective of a practical WPT system prototype for the biomedical implants, research efforts on both the inductive and the magnetic resonant WPT systems have been presented. Both mechanisms are considered as good candidates to power the implanted biomedical devices. Appropriate technology should be chosen based on its design requirements. Therefore, before the systematic design and implementation, a pros & cons analysis is of great necessity to guide the technology selection for the given biomedical applications scenarios.

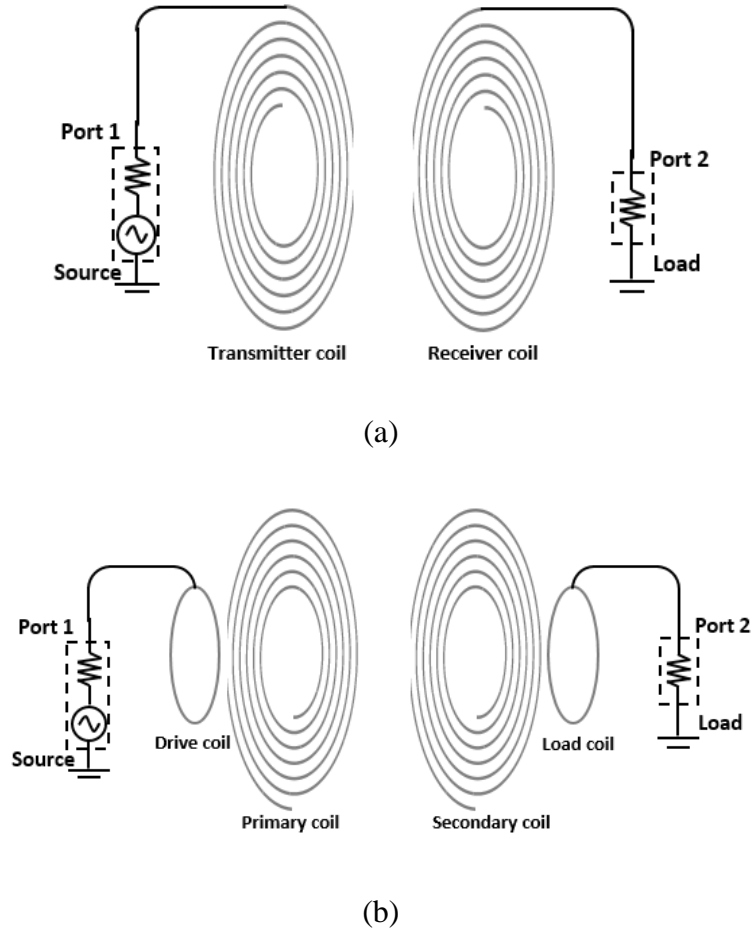


Figure 4.10 System diagram of different wireless power delivery approaches. .

Conventionally, the two-coil based inductive wireless power transfer in Fig. 4.10(a) is applied to deliver the RF power to the implantable medical devices. The RF power is inductively coupled from the transmitter coil to the receiver coil. With a detailed circuit analysis, the power transfer efficiency of the two-coil based inductive WPT system is calculated by Eq. 4.18.

$$\eta = \frac{k^2 Q_T Q_R}{1 + k^2 Q_T Q_R} \quad (4.18)$$

As can be seen, the power transfer efficiency of the inductive system is dominant by the Q-values of both the transmitter coil (Q_T) and the receiver coil (Q_R) and the mutual coupling in between, which is represented by the

coupling coefficient K . However, the Q -values of the coils are heavily limited in the inductive system and to achieve a high efficiency is challenging. As is shown in the inductive system diagram, the transmitter coil is in series with its source impedance and the receiver coil is in series with its load impedance. It results in a large portion of power loss in the source impedance when the generated current oscillating in the coil. Therefore, to achieve an acceptable power transfer efficiency, a close distance and high coupling coefficient must be guaranteed. Therefore, the inductive WPT system would achieve good performance in the close-range wireless power transfer.

Meanwhile, for the four-coil based magnetic resonant WPT systems, the additional two coils (primary and secondary coils) serve as the resonant tanks with high Q -values. They are designed to compensate the low Q -values of the drive and the load coils. For the four-coil based MR-WPT system, its power transfer efficiency can be calculated as shown below.

$$\eta = \frac{(k_{12}^2 Q_1 Q_2)(k_{23}^2 Q_2 Q_3)(k_{34}^2 Q_3 Q_4)}{[(1 + k_{12}^2 Q_1 Q_2)(1 + k_{34}^2 Q_3 Q_4) + k_{23}^2 Q_2 Q_3][1 + k_{23}^2 Q_2 Q_3 + k_{34}^2 Q_3 Q_4]} \quad (4.19)$$

In most cases, the coils are designed to get high Q -values and tight couplings can be guaranteed between drive and primary coils and between secondary and load coils. Therefore, the power transfer efficiency equation (4.19) can be simplified as Eq. (4.20) below.

$$\eta \approx \frac{k_{23}^2 Q_2 Q_3}{1 + k_{23}^2 Q_2 Q_3} \quad (4.20)$$

As can be seen in Eq. (4.20), the power transfer efficiency of the proposed MR-WPT system is dominated by the resonant tanks with high Q-values. The energy in the resonators is exchanged at a much higher rate than they lose energy due to the internal damping. By utilizing the resonance, the MR-WPT system can transfer the same amount of energy to a longer distance with much weaker magnetic fields. Therefore, the MR-WPT system can achieve much higher power transfer efficiency and longer transmission distance with loose coupling than its counterpart of the two-coil based inductive WPT system.

However, the drawback of the magnetic resonant WPT system is the frequency split when the two resonant circuits are tightly coupled at a close distance[50]. The system is no longer resonant at the original frequency and the maximum power transfer efficiency is shifted to either lower or higher frequencies with the resonance peak.

Summarized from all the analysis above, we can draw the conclusion that to the inductive WPT system mainly fits for the close-distance high-power wireless power delivery with simple system configurations. While, the MR-WPT system would be a better alternative for the wireless power delivery with high efficiency and deep implantation requirements. For the case of the spinal

cord stimulators in this thesis, we would like to select WPT system based on magnetic resonance mechanism for further development.

4.1.7 Summary

In this section, a rapid design approach for designing and tracking the optimal efficiency of the MR-WPT system is proposed. Besides, the MR-WPT system performance in biological tissue environment is also investigated. And a technology comparison between the inductive and the magnetic resonant WPT systems is also discussed to guide the technology selection for a systematic design with a given application scenarios. A concise mathematical model for the MR-WPT system and efficient design approaches are provided to obtain the optimal system configurations. The proposed design approach requires only two simple steps to accomplish the system design with an excellent accordance with the experiment. By applying the design approach, it significantly reduces the computation time compared with the current software optimizations. In this case, the proposed rapid design approach provides a good practice to accelerate the design of the MR-WPT system and the maximum efficiency tracking in the future.

4.2 Enhanced Dual-band Rectifier Design with an Ultra-Wide Power Range

4.2.1 Introduction

Wireless power transfer has become an attractive approach as the power supply for the sensor nodes in Wireless Body Sensor Network (WBSN) for its advantage of being available in the harsh biological environment where it is hard to deliver other power supplies. Besides the coil systems analyzed in the prior section, the rectifier block plays a significant role as well in the high efficiency WPT system design for IMDs. It converts the received RF signal into stable output DC power for the IMD circuits. Currently, most WPT designs apply the single band rectifiers, the multi-band rectifiers are only utilized in the ambient energy harvesting for additional channels to collect the RF energy in the air. However, the recent research shows that by applying an appropriately combined waveforms, the multi-band rectifier is able to obtain higher rectification efficiency. The efficiency improvement of combined multi-band signals initializes the research on the waveform configurations and optimizations. However, while improving the rectification efficiency, the multi-band rectifier suffers from an early breakdown problem as demonstrated in Fig. 4.11. Although resulting in the efficiency improvement in low power

range, the combined multi-band waveform causes its peak efficiency to shift to the low power side as well. It severely limits the operating power range and application scenarios of the multi-band rectifier.

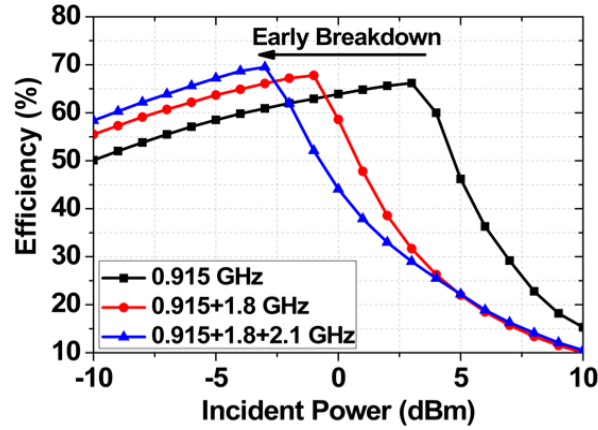


Figure 4.11 Demonstration of breakdown point shift by single (0.915 GHz), dual (0.915GHz & 1.8 GHz) and triple (0.915 GHz & 1.8 GHz & 2.1 GHz) band RF power inputs. RF energy is equally delivered from each band.

Therefore, in order to investigate the efficiency improvement of the combined multi-band waveforms and overcome the limitations of the multi-band rectifiers, a dual-band rectifier operating the GSM-900 and GSM-1800 bands is demonstrated in this section. It presents two improvements to tackle the above-mentioned problems. 1) The reconfigurable diode topology is implemented to extend its operating power range in GSM bands; 2) The optimal waveform configurations are investigated in the dual-band rectifier with different incident power ratios of each band.

4.2.2 Rectifier Design

Typically, there exist two major types of rectifier structures in the state-of-the-arts multi-band rectifier designs as shown in Fig. 4.12: the independent incident structure and the simultaneous incident structure. For the traditional independent incident structure in Fig. 4.12(a), it is not a rare case that the RF energy distributed on each band does not have sufficient voltage to turn on the diode respectively, which results in a very low rectification efficiency. Therefore, for the low-power-level applications such as the power delivery to IMDs, the simultaneous incident structure in Fig 4.12(b) is more preferred to obtain a higher rectification efficiency than its counterpart.

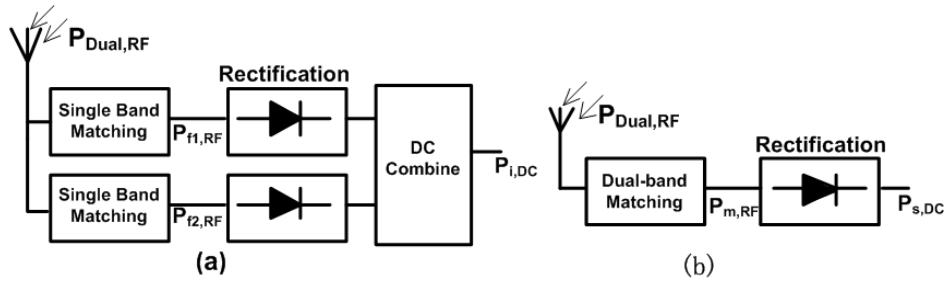


Figure 4.12 Rectifier Structure with different incident strategies (a) Independent input rectifier structure (b) Simultaneous input rectifier structure

However, although the simultaneous incident structure of the dual-band rectifier achieves a higher rectification efficiency, it is also restrained by the early breakdown problem in Fig. 4.11. There is always a tradeoff between the high rectification efficiency and the wide power range when selecting an

appropriate diode as the rectifying component. As indicated in the prior chapter, the low threshold voltage is preferred to obtain high efficiency in low power range while the wide operating power range would only be guaranteed with a high reverse breakdown voltage. However, conventional rectifiers can only obtain the desired efficiency in either low or high input power range due to the diode's physical structure. Some prior literature attempts to extend the rectifiers' operating power range. A switch-based rectenna [95] gets a relatively wide operating power range at the price of a complicated control circuit. An adaptive rectifier structure was presented in [108] to extend its operating power range. However, a number of components in the structure introduce large amount of unnecessary power losses and the 100 MHz single frequency design is less practical for the high-frequency WPT applications.

In order to extend the operating power range of the rectifier with a simple and effective approach, the single-stage reconfigurable diode topology in chapter 3 is implemented as shown in Fig. 4.13(a). The rectifier consists of a Schottky diode D1 and a pseudomorphic HEMT T1. The diode-equivalent topology has a threshold voltage as V_{th} and a breakdown voltage as V_{dg-BR} , which attributes to the breakdown voltage from gate and drain of the applied HEMT.

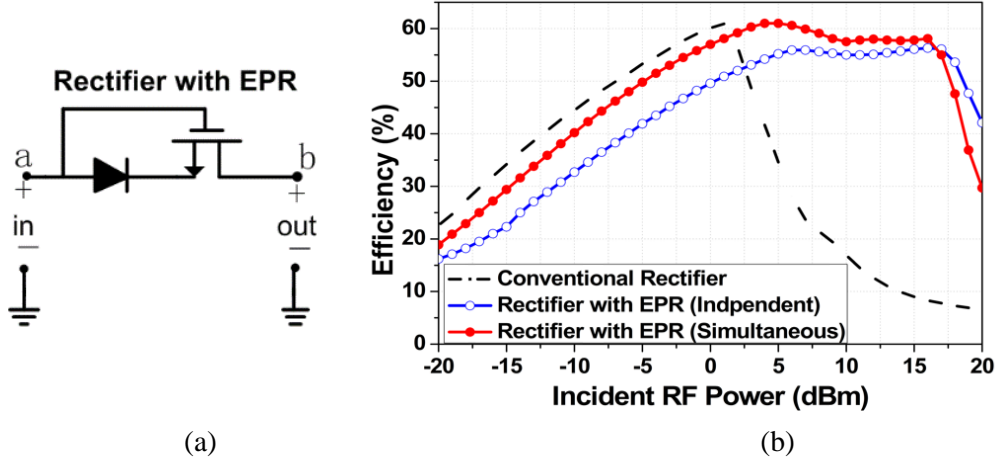


Figure 4.13 (a) Block structure of rectifier with EPR (b) simulated dual-band RF-DC conversion efficiencies of conventional rectifier and rectifier with EPR in both independent and simultaneous mode. RF energy is equally delivered from each band

The simulated dual-band (0.915 GHz and 1.8 GHz) efficiencies of the conventional rectifier and the rectifier with EPR in both independent and simultaneous modes are illustrated in Fig. 4.13(b). As compared in the figure, the operating power range of the rectifier with EPR in the simultaneous mode is greatly extended to 21 dBm (-4 dBm to 17 dBm) from the 10 dBm (-8 dBm to 2 dBm) power range of the conventional rectifier with the efficiency more than 50%. The peak efficiency around 60% of the rectifier with EPR in simultaneous mode is ranging from 5 dBm to 15 dBm. Moreover, as indicated in Fig. 4.13(b), the simultaneous mode of the dual-band rectifier with EPR gets an efficiency improvement over the independent mode. In general, the simulation results in Fig. 4.13(b) effectively verify both the power range extension and efficiency improvement of the proposed dual-band rectifier with

EPR in simultaneous incident mode. Experiment measurement and further analysis are presented in the section 4.2.3 below.

4.2.3 Experiment and Measurement

The schematic and fabricated circuits of the proposed rectifier are illustrated in Fig. 4.14. A zero-bias Schottky diode (Avago HSMS2850) is chosen due to its ultra-low threshold voltage (150mV). A GaAs pseudomorphic HEMT (ATF34143) is introduced with a threshold voltage of -0.5V. As shown in Fig. 4.15, simultaneous dual-band input is generated from two signal generators Agilent E8257D and power combiner HP 87302C. Pre-calibration has been done by the spectrum analyzer Anritsu MS2651B to determine the exact power received by the circuit.

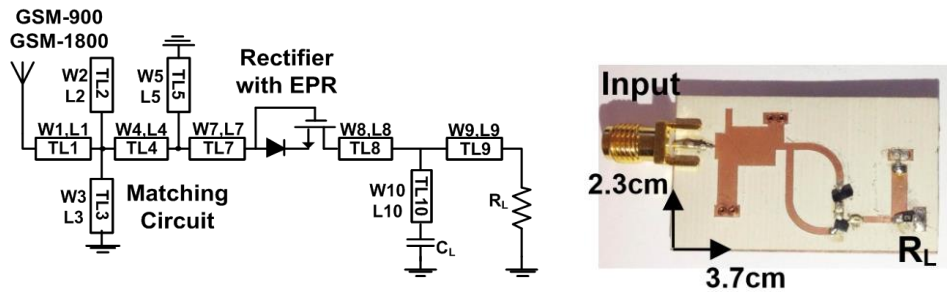


Figure 4.14 Schematics and fabricated circuits of the proposed rectifier with EPR
W1=4.2mm, L1=0.5mm, W2=1mm, L2=2.5mm, W3=3.6 mm, L3=6.7mm, W4=4.1 mm, L4=5 mm, W5=1.6 mm, L5=0.5mm, W6=1 mm, L6=0.3mm, W7=1 mm, L7=5 mm, W8=1 mm, L8=0.5 mm, W9=1.9mm, L9=9 mm, W10=1.4mm, L10=6.5 mm, CL=470 pF, RL=2.1k Ω .

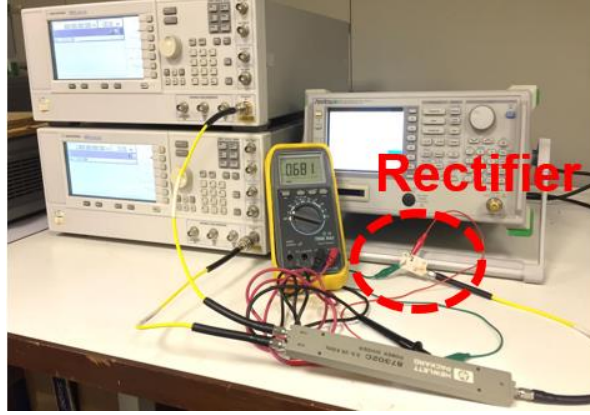


Figure 4.15 Experiment and Measurement Setup

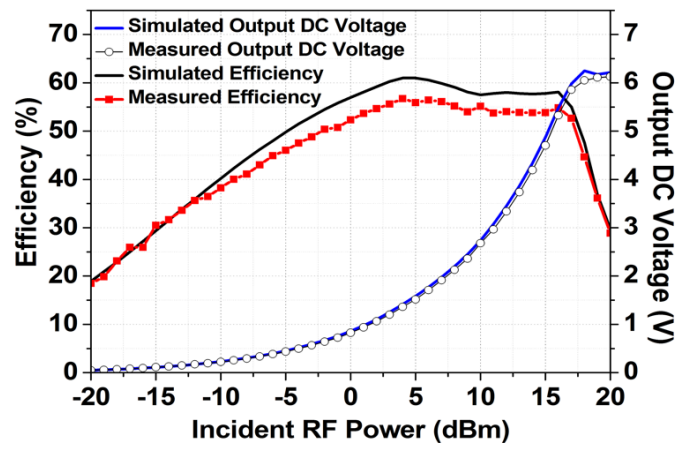


Fig. 4.16 Simulated and measured efficiency and output DC voltage of the dual-band rectifier in simultaneous input mode. RF power is equally delivered from each band.

Fig. 4.16 shows both the simulated and measured RF-DC conversion efficiencies and output voltages versus input power level when the dual-band RF power is simultaneously input into the rectifier. The measured efficiencies agree with the simulated ones well. Measured efficiency of more than 30% has been gained from -15dBm to 20dBm. The maximum output DC voltage is 6.2V on a 2.1k Ω load with an input power of 20dBm.

Table. 4.3 shows a comprehensive performance comparison between the rectifier with EPR and the state-of-the-art ones [6]-[9]. As indicated, the input

power range for efficiency more than 30% of the proposed rectifier with EPR appears favorably compared with other designs. The previous works can only cover either the low input power range ($P_{in} < 0\text{dBm}$) or the high input power range ($P_{in} > 0\text{dBm}$) while the proposed rectifier with EPR shows an excellent power handling capability ranging from -15dBm to 20dBm. Therefore, this proposed work would be a practical rectifier design with the wide operating power range and the high rectification efficiency at the same time.

Table 4.3 Rectifier Performance Comparison

Ref.	Topology	Freq (GHz)	P_{in} (dBm) for eff > 30%
[100]	Dual diode structure	2.45	-1 to 18
[101]	Diode in series	5.8	-2 to 13
[102]	Differential 2-stage rectifier	0.868	-17 to -3
[103]	Dual band resistor compression	0.915/2.45	> -10 to 0
This Work	Dual band extended power range	0.915+1.8	-15 to 20

4.2.4 Incident Waveform Analysis

Although Fig. 4.13(b) has given a glimpse of the efficiency improvement and operating power range extension of the dual-band rectifier in the simultaneous mode, the theoretical analysis and comprehensive investigations

are still necessary to present a solid foundation for the waveform-optimized WPT system design. Besides, the operating power range extensions are also clearly observed in the analysis with various incident power ratios.

As is known, the RF-DC conversion efficiency of the rectifier is a function of its incident power level as in (4.21), in which P_{in} is the total power including all incident RF power into circuit and P_{DC} is the output DC power over the load.

$$\eta (\%) = \eta(P_{in}) = \frac{P_{DC}}{P_{in}} \times 100\% \quad (4.21)$$

To demonstrate the efficiency enhancement, an important metric power gain G_P is defined in Equation (4.22). It indicates the enhancement capability of the simultaneous multiband incidence over the independent incidence for the same topology. $P_{s,DC}$ and $P_{i,DC}$ are the time averaged output powers of the simultaneous and the independent multiband incidence, respectively.

$$\begin{aligned} G_P &= 10 \log \left(\frac{P_{s,DC}}{P_{i,DC}} \right) = 10 \log \left(\frac{P_{s,RF} \cdot \eta(P_{s,RF})}{\sum_i P_{f_i,RF} \cdot \eta(P_{f_i,RF})} \right) \\ &= 10 \log \left(\frac{P_{f_1,RF} \cdot \eta(P_{s,RF}) + \cdots + P_{f_i,RF} \cdot \eta(P_{s,RF})}{P_{f_1,RF} \cdot \eta(P_{f_1,RF}) + \cdots + P_{f_i,RF} \cdot \eta(P_{f_i,RF})} \right) \end{aligned} \quad (4.22)$$

Assuming that the multiband simultaneously incident power equals the sum of each band independently incident. So, for the input power in each band,

$$\forall i, P_{s,RF} > P_{f_i,RF} \quad (4.23)$$

Besides, the theoretical analysis in [68][69] indicates that, before breakdown, the RF-DC efficiency monotonically increases with the rectifier's input power when either the single or multiband input. Based on Equation (4.24), simultaneous multiband input power obtains higher efficiency than the RF power on each band with separate input.

$$\forall i, \eta(P_{s,RF}) > \eta(P_{f_i,RF}) \quad (4.24)$$

Therefore, $P_{s,DC} > P_{i,DC}$ and $G_P > 0$ before it breaks down.

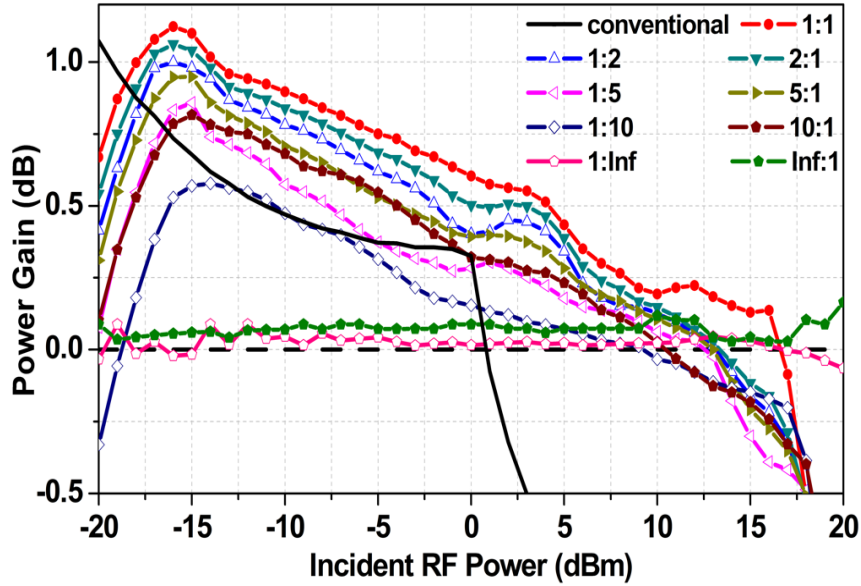


Figure 4.17 Investigation of power gain performance of dual-band conventional (diode in series structure) rectifier (0.915GHz: 1.8GHz=1:1) and dual-band rectifier with EPR with different input power ratios (0.915GHz: 1.8GHz).

Upon the theoretical analysis above, Fig. 4.17 illustrates a comprehensive investigation of the power gain performance of the proposed dual-band rectifier with different incident power ratios. The figure below, on one hand, indicates the operating power range extension of the proposed dual-band

rectifier with EPR (red dot curve) over the conventional rectifiers (black solid curve) with the incident power ratio $0.915 \text{ GHz} : 1.8 \text{ GHz} = 1:1$. The conventional rectifier's power gain drops below zero with 1 dBm while the rectifier with EPR has an extended power range to 17 dBm. Moreover, the effects of the incident power ratios on the power gain of the proposed dual-band rectifier with EPR are also investigated in Fig. 4.17. As can be seen, the power gains of the simultaneous mode over the independent mode are approaching zero when the incident power ratio is large. Since the minor part under the large power ratio could be ignored, both two modes are almost the same and achieve little gain. When the RF power in the two bands become closer, the incident power ratio becomes small and the related power gain increases. It indicates the efficiency improvement of the combined multi-band waveforms. The proposed dual-band rectifier is optimized to achieve its maximum power gain when the RF energy is equally delivered from each band. The incident power ratio that gets the maximal power gain would be different with the rectifier's performance on each RF band configured by circuit parameters. This investigation provides a good reference for future rectifier design with customized waveforms.

4.2.5 Summary

In conclusion, a novel dual-band rectifier with extended power range and an optimal RF power incidence strategy is designed. More than 30% efficiency is achieved in the extended power range from -15dBm to 20dBm with dual-band inputs. The positive power gains from -20 dBm to more than 10 dBm demonstrate the efficiency improvement resulted from the combined multi-band waveforms. With these two features, it would be a good reference for the future multiband rectifier design.

4.3 Conclusion

In this chapter, the block level research work is presented from both the coil system modeling and the rectifier design. Concise mathematical models and rapid design approach are demonstrated for the coil design in the MR-WPT system with consideration for bio-implant scenarios. The comparison between the inductive and magnetic resonant WPT systems provides a theoretical reference to the technology selection for the systematic WPT design with various design requirements. A dual-band rectifier with extended power range and its optimal combining strategy are designed upon the characteristics of the multi-band optimized waveforms. Different incident power ratios are investigated for waveform optimization.

In summary, these block-level designs in chapter 4 investigate both the coil system and the rectifier designs. They provide a solid foundation for the system-level WPT system design based on the optimized waveforms. Detailed design guideline and prototype are presented in chapter 5 for the IMD applications.

Chapter 5 In-Vivo High-Efficiency Wireless Power Transfer with Multi-sine Excitation

Based on the research investigations from the previous chapters, it has been proven to be a practical approach for applying the multi-sine waveform into the practical applications for biomedical implants. A multi-sine waveform based MR-WPT system is proposed in this chapter for implantable biomedical devices. The MR-WPT system obtains the desired high efficiency with an elaborate design by applying the optimized multi-sine waveforms with a high PAPR. System-level design considerations on the flexible coil design, system transfer model, and rectifier topology are all involved in improving the overall system efficiency and meanwhile eliminating its drawbacks. With all the optimized designs, the multi-sine waveform is for the first time implemented in an in-vivo MR-WPT system for the IMD power delivery. An MR-WPT system operating under 6.78 MHz center frequency is realized for wirelessly powering the miniaturized spinal cord stimulator implanted 18 mm beneath the skin. It achieves an overall system efficiency (both coils and rectifier included) of 50.7% with a 3-tone (230 kHz tone spacing) multi-sine waveform in the rat experiment. Low SAR and low temperature increase are

demonstrated to guarantee a safe and practical wireless power link for biomedical implants.

5.1 Introduction

In the recent decades, IMDs have become a focal point of interest as a promising technique for the future clinic diagnostics and therapy. The implantable devices have been adopted in a variety of advanced biomedical applications such as optogenetics [93], neural recording [22] and stimulation [20], etc. Among the various implantable devices, wirelessly-powered implants feature many advantages over the traditional ones with transcutaneous wire and bulky batteries. By replacing the wires and batteries with a high efficiency wireless power delivery link, the WPT technique efficiently reduces the patients' risk of infections and eliminates the frequent surgeries intended for battery replacement. Besides, the removal of the battery also makes it easier to miniaturize the IMD design and implant it with smaller incisions.

In the design of a high efficiency WPT system, it is always a significant issue to obtain both the optimal energy transfer and conversion efficiency. However, the current WPT systems for biomedical implants usually cannot achieve a satisfactory overall efficiency due to the limited RF power delivered

to the target implantable devices and the poor rectifier performance in such low incident power levels. To improve the WPT system efficiency, most of the research efforts have focused on the optimizations of the transmitter and receiver designs, both of which are usually based on the single-carrier, continuous-wave (CW) signal transmission waveform. Attention on the transmission waveform optimization has been paid only in recent years [65] [79]. As indicated in chapter 2, the optimized multi-sine signal with high PAPR can effectively improve the system efficiency compared with the traditional single-frequency sine waveform. It would be an excellent alternative to select multi-sine waveform to boost the WPT system efficiency for biomedical implants.

Therefore, here in this chapter, we present a completed systematic design procedure of adopting the multi-sine waveform into the practical MR-WPT systems for biomedical implants. Various considerations are involved from theoretical system models, biological effects and new rectifier topologies to improve the MR-WPT performance with the multi-sine excitation. Based on the multi-sine waveforms' mechanism analysis in Section 5.2, a series of system modeling and circuit design considerations are presented in Section 5.3 as the design guidance for a practical multi-sine MR-WPT system. Section 5.4

demonstrates a multi-sine MR-WPT prototype for spinal cord stimulator application [22] to verify the proposed design procedure from the coil and system model designs to the practical rectifier topology design. The tissue effects and in-vivo experiment in the rodent model are studied in Section 5.5. Moreover, Section 5.6 concludes the results obtained in this chapter.

5.2 Multi-sine Waveform Analysis

As presented in chapter 2, the multi-sine waveform has been considered as an appropriate alternative for the waveform-optimized WPT system. The synthesized multi-sine waveform composes of in-phase, narrowly-spaced multi-tone signals and it presents high PAPR in the time domain. It has been proven that it is able to improve the system efficiency compared with the traditional single frequency sine waveform. For the optimized multi-sine waveform, different configurations of the tone characteristics such as the number of tones and tone spacing determine its time-domain shapes. With the proper settings, the multi-sine waveform obtain a high PAPR and thus an improved overall system efficiency. s

Examples of CW and the optimized multi-sine waveform are demonstrated to verify the efficiency improvement effect of the multi-sine signals. For the system illustration under 6.78MHz, which is the frequency band raised by

Alliance For Wireless Power (A4WP) for wireless charging, Fig. 5.1 presents both the frequency spectrum and the time-domain waveforms of 6.78MHz CW signal and 3-tone evenly-spaced multi-sine signals with 6.78MHz as center frequency and 10 kHz as tone spacing.

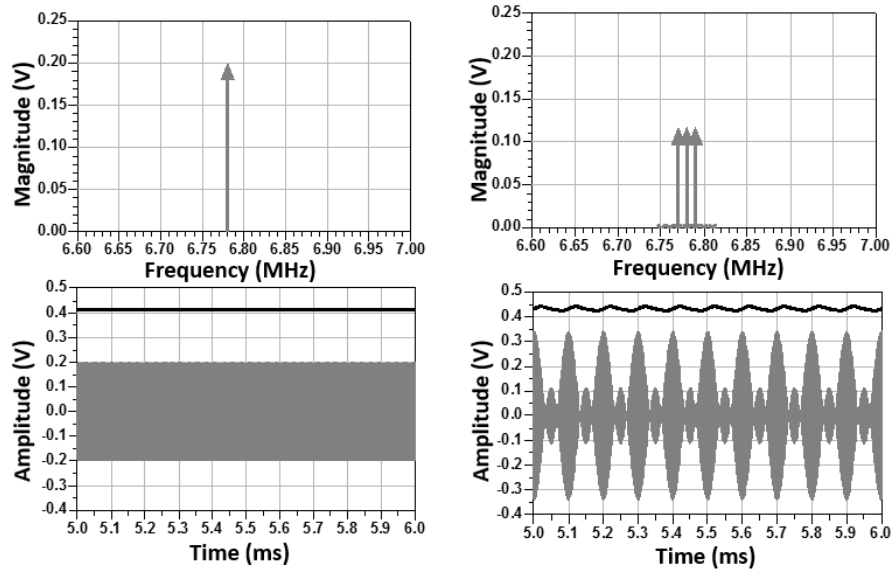


Figure 5.1 Frequency spectrum and time-domain waveforms of 6.78 MHz CW signal and 3-tone 10 kHz-spacing multi-sine waveforms.

Different spectrums and time-domain waveforms are presented in Fig. 5.1 with the same average power. As can be seen, the DC output is lift up by applying the 3-tone multi-sine waveform and it will be further improved when an increased number of tones are involved [61]. The tone separation in spectrum determines the signal's periodic peaks and the output ripples in time domain. Careful considerations and tradeoff should be made when the multi-sine WPT is applied in various application scenarios. Inappropriate

configurations of the tone number and spacing would leads to the potential problems of rectifier's early breakdown and large output ripples [104].

In order to achieve an excellent overall performance, tone spacing should be properly optimized within a given application scenarios. Inappropriate wide tone spacing may result in rectifier's mismatch and thus lower the efficiency. And if a narrow tone spacing applies, the peaks would be largely spaced and the ripple might be also increased to a value that is not tolerated by the circuits to be powered. Therefore, in designing the multi-sine waveform for WPT system, an appropriate tone spacing within rectifier's bandwidth is preferred to eliminate the output DC ripple and improve the system stability.

5.3 System Modelling and Analysis

Prior to designing a high efficiency multi-sine MR-WPT prototype for biomedical implants, the fundamental system characteristics should be carefully analyzed. In this section, we present a comprehensive investigation from component level to the circuit block level, which involves the integral coil model, the power transfer model and the reconfigurable rectifier design.

5.3.1 Integral Inductor Model

To model the MR-WPT system, accurate models of self-inductance and mutual inductance to quantitatively describe the inductance behavior of coils are highly desired. Currently, it is a common practice to approximate the planar spiral coil as multiple concentric circular loops with different radii [56]. The accuracy of this practice in most cases is acceptable to coils with a large number of turns. However, its accuracy may deteriorate when it applies to coils with only a few turns or large turn spacing, which are frequently used in MR-WPT systems as the drive and load loop. In order to get accurate coil designs, here in this section, we'd like to model the spiral coils as Archimedes spiral in the Cartesian coordinate system and calculate its self-inductance as a curve integral [105] and its mutual inductance by Neumann formula.

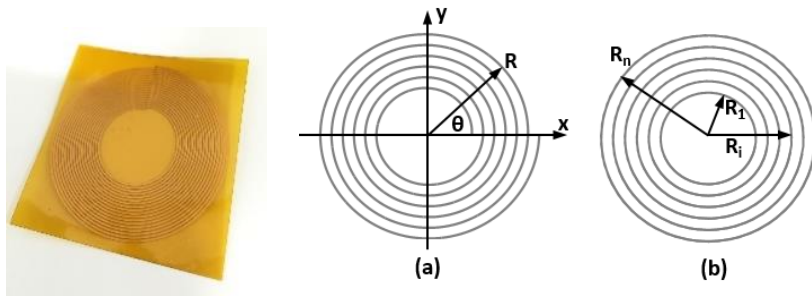


Figure 5.2 Photography of the planar spiral coil (PSC) and its equivalent models (a) Archimedes spiral model (b) concentric-loop model.

The general Neumann formula derived from Eq. (2.9) for mutual inductance calculation is also presented in (5.1). \mathbf{r}_1 and \mathbf{r}_2 represent the radii vectors of the wire fractions \mathbf{l}_1 and \mathbf{l}_2 in the integral.

$$M = \frac{\mu_0}{4\pi} \iint \frac{d\mathbf{l}_1 \cdot d\mathbf{l}_2}{|\mathbf{r}_2 - \mathbf{r}_1|} \quad (5.1)$$

Accordingly, the self-inductance is presented in (5.2) as the equation (5.1) derivation when $\mathbf{l}_1 = \mathbf{l}_2$ with a correction item to avoid the $1/|\mathbf{r}_2 - \mathbf{r}_1|$ in the integral becomes infinite.

$$L = \left(\frac{\mu_0}{4\pi} \iint \frac{d\mathbf{l}_1 \cdot d\mathbf{l}_2}{|\mathbf{r}_2 - \mathbf{r}_1|} \right)_{|\mathbf{r}_2 - \mathbf{r}_1| > \frac{a}{2}} + \frac{\mu_0}{4\pi} lY \quad (5.2)$$

Here a and l denotes the radius and length of the coil. Y is a constant depending on the current distribution in the wire. $Y = 0$ when the skin effect occurs and $Y = 1/2$ when the current in the wire is distributed homogeneously.

In our proposed coil design, the spiral coil is modeled accurately as the Archimedes spiral in the Cartesian coordinate system in equation (5.3) below, where a and b are the initial radius and turn spacing of the coil, respectively.

$$\begin{aligned} x(\theta) &= r(\theta) \cdot \cos \theta \\ y(\theta) &= r(\theta) \cdot \sin \theta \text{ where } r(\theta) = a + b\theta \end{aligned} \quad (5.3)$$

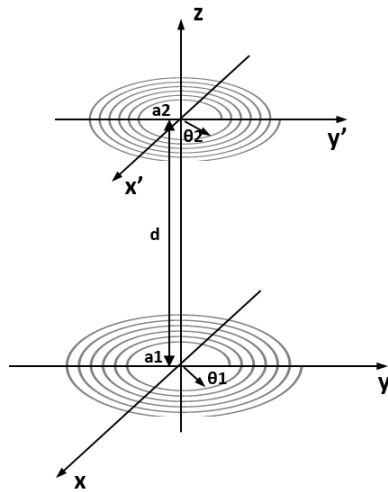


Figure 5.3 Self-inductance and mutual inductance calculation based on the integral inductor model in Cartesian coordinates.

Therefore, the modeled self-inductance and mutual inductance for an n-turn PSC are shown in equation (5.4) and (5.5).

$$L = \left(\frac{\mu_0}{4\pi} \iint_0^{2\pi n} \frac{(b^2 + r^2) \cos(\theta_1 - \theta_2)}{[2r^2(1 - \cos(\theta_1 - \theta_2))]^{\frac{1}{2}}} d\theta_1 d\theta_2 \right)_{|r_2 - r_1| > \frac{a}{2}} + \frac{\mu_0}{4\pi} lY \quad (5.4)$$

$$M = \frac{\mu_0}{4\pi} \iint \frac{(b_1 b_2 + r_1 r_2) \cos(\theta_1 - \theta_2) + (b_1 r_2 - b_2 r_1) \cos(\theta_1 - \theta_2)}{[r_1^2 + r_2^2 - 2r_1 r_2 \cos(\theta_1 - \theta_2) + d^2]^{\frac{1}{2}}} d\theta_1 d\theta_2 \quad (5.5)$$

By modeling the spiral coil as the Archimedes spiral in Cartesian coordinates, it provides better accuracy in WPT coil design than the traditional approximation approach, especially for the drive and load loops in MR-WPT systems. Only by obtaining accurate self-inductance and mutual inductance models could the MR-WPT systems guarantee an efficient and accurate design procedure.

5.3.2 Power Transfer Model

In most cases, the state-of-the-art theoretical models for MR-WPT systems are only valid in its resonant condition, here we provide a complete theoretical model for an MR-WPT system applied in all circumstances and accordingly present a bandwidth calculation for the proposed multi-sine transmission waveform. The calculated system bandwidth determines the tone spacing configurations of the proposed multi-sine waveform. As analyzed in section 5.2 before, an appropriate tone spacing results in high efficiency with less

ripple and is much preferred in designing a stable MR-WPT system.

Bandwidth information is crucial to determine the proper tone spacing of the incident multi-sine waveforms and thus a high efficiency stable MR-WPT system.

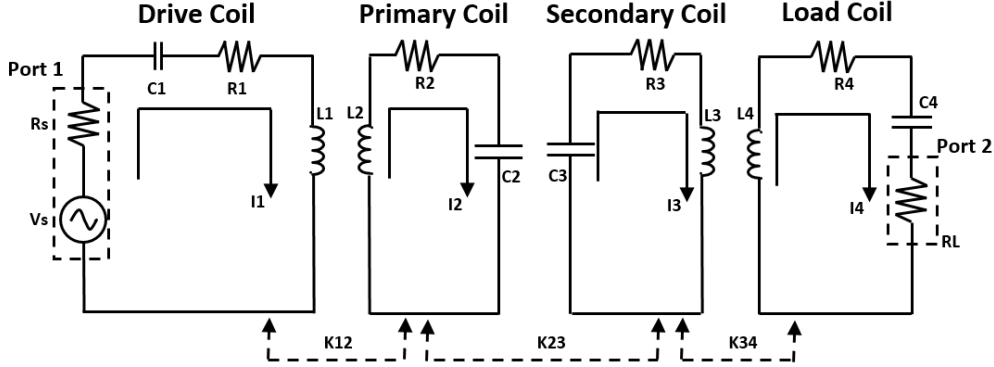


Figure 5.4 System Diagram of Magnetic Resonant Wireless Power Transfer

Although the system diagram and its equivalent circuit matrix for the MR-WPT system have been revealed in section 4.1.2, they are also presented here in Fig. 5.4 and equation (5.6) for easy reference.

$$\begin{bmatrix} Z_1 & j\omega M_{12} & 0 & 0 \\ j\omega M_{12} & Z_2 & j\omega M_{23} & 0 \\ 0 & j\omega M_{23} & Z_3 & j\omega M_{34} \\ 0 & 0 & j\omega M_{34} & Z_4 \end{bmatrix} \begin{bmatrix} I_1 \\ I_2 \\ I_3 \\ I_4 \end{bmatrix} = \begin{bmatrix} V_s \\ 0 \\ 0 \\ 0 \end{bmatrix} \quad (5.6)$$

The impedance of each coil can be expressed as below:

$$Z_4 = j\omega L_4 + \frac{1}{j\omega C_4} + R_L + R_4 \quad (5.7)$$

$$Z_3 = j\omega L_3 + \frac{1}{j\omega C_3} + R_3 \quad (5.8)$$

$$Z_2 = j\omega L_2 + \frac{1}{j\omega C_2} + R_2 \quad (5.9)$$

$$Z_1 = j\omega L_1 + \frac{1}{j\omega C_1} + R_S + R_1 \quad (5.10)$$

The current flow in each coil is obtained by solving the matrix in (5.6) and only the current in the drive and load coil is presented in (5.12)-(5.13). k_{ij} denotes the coupling coefficients between coil i and coil j and has been defined in equation (5.11).

$$k_{ij} = M_{ij} / \sqrt{L_i L_j} \quad (5.11)$$

$$I_1 = \frac{\omega^2 k_{23}^2 L_2 L_3 Z_4 + \omega^2 k_{34}^2 L_3 L_4 Z_2 + Z_2 Z_3 Z_4}{(Z_1 Z_2 + \omega^2 k_{12}^2 L_1 L_2)(Z_3 Z_4 + \omega^2 k_{34}^2 L_3 L_4) + \omega^2 k_{23}^2 L_2 L_3 Z_1 Z_4} \cdot V_s \quad (5.12)$$

$$I_4 = \frac{j\omega^3 k_{12} k_{23} k_{34} L_2 L_3 \sqrt{L_1 L_4}}{(Z_1 Z_2 + \omega^2 k_{12}^2 L_1 L_2)(Z_3 Z_4 + \omega^2 k_{34}^2 L_3 L_4) + \omega^2 k_{23}^2 L_2 L_3 Z_1 Z_4} \cdot V_s \quad (5.13)$$

As indicated in chapter 4, the latter coil could be regarded as an equivalent load for the former coil in the coil system. Therefore, the overall input impedance Z_{in} when looked into the drive coil from the power source side is expressed as following:

$$\begin{aligned} Z_{in} &= R_1 + j\omega L_1 + \frac{1}{j\omega C_1} + \frac{j\omega M_{12} \cdot I_2}{I_1} \\ &= R_1 + j\omega L_1 + \frac{1}{j\omega C_1} + \frac{(\omega M_{12})^2}{Z_2 + \frac{(\omega M_{23})^2}{Z_3 + \frac{(\omega M_{34})^2}{Z_4}}} \\ &= R_1 + j\omega L_1 + \frac{1}{j\omega C_1} + \frac{\omega^2 k_{12}^2 L_1 L_2 (\omega^2 k_{34}^2 L_3 L_4 + Z_3 Z_4)}{\omega^2 k_{23}^2 L_2 L_3 Z_4 + \omega^2 k_{34}^2 L_3 L_4 Z_2 + Z_2 Z_3 Z_4} \end{aligned} \quad (5.14)$$

Therefore, the system efficiency is calculated accordingly as shown in equation (5.15).

$$\eta = |S_{21}|^2 = \frac{P_{out}}{P_{in}} = \frac{I_4 I_4^* R_L}{I_1 I_1^* |Z_{in}|} \quad (5.15)$$

In order to explore the bandwidth of the entire MR-WPT system with less mismatch loss, here we'd like to define the 1dB bandwidth of the system as shown in (5.16).

$$S_{21}|_r - S_{21}|_{BW} = -1 \text{ dB} \quad (5.16)$$

Substituting (5.15) into (5.16), we get the system bandwidth expression as shown in (5.18). Several definitions and notations are made in (5.17) for clarification, where ω_0 is the resonant frequency and BW is the bandwidth of the MR-WPT system.

$$\frac{\omega - \omega_0}{\omega_0} \triangleq \frac{1}{2} BW, \alpha_{ij} = k_{ij} Q_i Q_j, \beta_i = 1 + jBW Q_i \quad (5.17)$$

$$\begin{aligned} -1dB = & \left(\frac{\omega}{\omega_0}\right)^6 \cdot \frac{1 + \alpha_{23} + \alpha_{34}}{\left(\frac{\omega}{\omega_0}\right)^2 (\alpha_{23}\beta_4^* + \alpha_{34}\beta_2^*) + \beta_2^* \beta_3^* \beta_4^*} \cdot \\ & \frac{1 + \alpha_{23} + \alpha_{34} + \alpha_{12}(1 + \alpha_{34})}{\beta_1^* \left[\left(\frac{\omega}{\omega_0}\right)^2 (\alpha_{23}\beta_4 + \alpha_{34}\beta_2) + \beta_2 \beta_3 \beta_4 \right] + \left(\frac{\omega}{\omega_0}\right)^2 \alpha_{12} \left[\left(\frac{\omega}{\omega_0}\right)^2 \alpha_{34} + \beta_3 \beta_4 \right]} \end{aligned} \quad (5.18)$$

From the equation (5.18), we get a clear insight that the system bandwidth is mainly determined by the Q_i value of each coil and the coupling coefficients k_{ij} in between. With the system bandwidth calculated, the multi-sine transmission waveform can be appropriately designed to achieve the optimal system performance.

Therefore, the proposed power transfer model in this section reveals a completed MR-WPT system on both resonant and non-resonant modes. Different from the critically coupling point calculation in traditional models,

the bandwidth calculation above provides a frequency range with acceptable transmission loss, which provides a useful reference for the appropriate multi-sine waveform design. Given the bandwidth information of the MR-WPT system, an appropriate tone spacing is then selected to tradeoff between the transmission loss and the output ripple. Therefore, the tone spacing should be large and fully utilize the calculated bandwidth. Therefore, an appropriate tone spacing should be $BW/(N - 1)$ with N as the number of tones selected upon the design requirements.

5.3.3 Reconfigurable Rectifier Topology Design

With the calculated system bandwidth, the multi-sine waveform can be properly configured as the transmission waveform. When the multi-sine waveform is incident into the rectifier circuit, it achieves higher RF-DC efficiency than its counterpart with traditional single frequency CW waveform. However, although the multi-sine waveform gets an improved efficiency, it causes the rectifier's early breakdown as indicated in chapter 4. Regarding the features of multi-sine waveforms, the desired rectifier requires a high breakdown voltage V_{br} to prevent the early breakdown as well as an ultra-low threshold voltage V_{th} to retain the high rectification efficiency with the high PAPR multi-sine inputs. In order to provide a practical solution for the multi-

sine WPT, the iterative reconfigurable rectifier topology [97] in chapter 3 is applied in this chapter as shown in Fig. 5.5. It obtains both the sufficient high breakdown voltage V_{br} and the low threshold voltage V_{th} . Therefore, it extends the rectifier's input power range as well as retains the high RF-DC efficiency from multi-sine inputs.

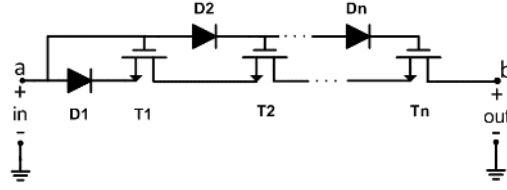


Figure 5.5 Iterative Reconfigurable Rectifier Topology

The iterative reconfigurable rectifier topology in Fig. 5.5 is composed of a series of diodes and N-channel MOSFETs, which have a negative switch-on voltage. When the topology is forward biased, MOSFETs are ON and the topology is equivalent to a simple diode. In the reverse biased situation, MOSFETs would firstly turn OFF and hold most of the reverse biased voltages to protect the diode D1 from an early breakdown. Based on the analysis in chapter 3, the topology obtains a sufficiently high reverse breakdown voltage as long as equation (3.23) is satisfied. The diode-equivalent topology has the low threshold voltage $V_{D1|TH}$ and the tunable reverse breakdown voltage $V_{gd|BR} + (n - 1)V_{d|BR}$ regardless of the semiconductor constraints.

The iterative reconfigurable diode topology can be tuned to fit for most of the application scenarios requirements. When applied to multi-sine scenarios, it effectively solves the early breakdown problem and extends its improved efficiency to a wide power range. Therefore, the iterative reconfigurable rectifier topology with a proper configuration can be regarded as a practical solution to the problem in the state-of-the-art multi-sine WPT systems.

5.4 Experimental Verification

In this section, we discuss the design of an entire multi-sine MR-WPT system for wirelessly powering an implantable spinal cord stimulator as a therapeutic solution for neuropathic pain management. Based on all the analysis and considerations above, wireless power is transmitted in the form of the multi-sine waveform and rectified into stable DC power efficiently. A high efficiency multi-sine MR-WPT system is practically designed based on the full considerations in section 5.3 and implemented from the flexible coil design to in-vivo rodent experiment.

5.4.1 Flexible Coil Design

Flexible printed planar spiral coil (PSC) is an ideal candidate for the proposed biomedical implants when compared with its wire-wound counterparts. The flexible PSC is biocompatible and can be fabricated to a

compact size to get a minimally invasive implant, whereas the wire-wound coils cannot reduce in size without sophisticated machinery.

In this experiment, four PSCs are designed on the flexible substrate of DuPont Kapton with a dielectric of 3.5. The copper wire width is 0.5 mm for transmitter coils (coil 1 and 2) and 0.3 mm for receiver coils (coil 3 and 4). For the implanted stimulator, the maximum outer diameter of the receiver coils is chosen to be 20 mm. The distance between transmitter and receiver is set to 18 mm as the optimal implant depth. Based on these design constraints, coils are designed as listed in Table. 5.1.

Table 5.1 Coil Physical Parameters

Type	Drive Coil	Primary Coil	Secondary Coil	Load Coil
Inner Dia. (mm)	18	21	8	18
Outer Dia. (mm)	24	48	20	20
Turns	4	18	12	2
L(μ H) – M1	0.602	13.53	2.26	0.184
M1 Error (%)	+7.8	+5.2	+4.6	+6.4
L(μ H) – M2	0.541	12.397	2.108	0.165
M2 Error (%)	-3	-3.6	-2.5	-4.7
L(μ H) – CST	0.548	12.681	2.194	0.167
L(μ H) - Meas	0.558	12.871	2.161	0.173
Resonant C(pF)	1000	43	250	3300
Resistor(Ohm)	0.182	2.53	0.83	0.106

In order to verify the proposed integral inductor model presented in section 5.3, a comparison between various inductor models is presented in Table 5.1 among the traditional model [106] (M1), the proposed integral inductor model (M2), CST simulation and measurement results. From the comparisons, we can clearly conclude that the newly proposed integral inductor model achieves the accuracy within 5% while the traditional model has a larger error to around 8%, in particular for inductors with fewer turns. The refined inductor model

helps in magnetic resonant WPT system design since its drive and load loops in most cases have fewer turns and a key influence on the system performance.

5.4.2 MR-WPT System Design

Based on the accurate models on self-inductance and mutual inductance, the coupling coefficients k_{ij} are plotted versus separating distances in Fig. 5.6 and the proposed MR-WPT system is designed accordingly referring to the approach [107] presented in chapter 4.

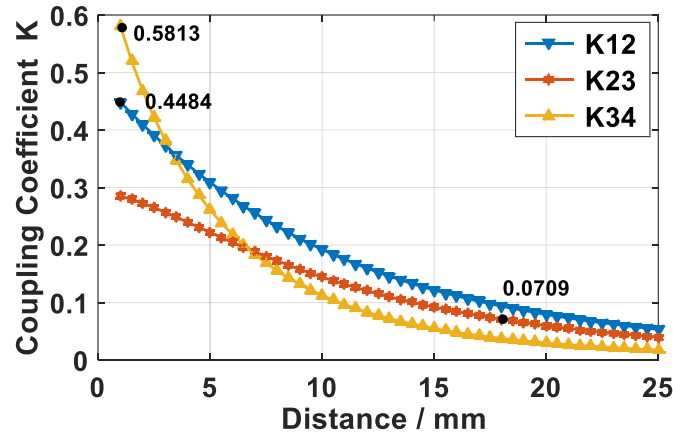


Figure 5.6 Coupling Coefficients vs. Separation Distance Configuration.

Considering the design constraints in implant scenarios, an appropriate set of coupling coefficients $K_{12}=0.4484$, $K_{23}=0.0709$, $K_{34}=0.5813$ is determined to achieve its optimal efficiency and an MR-WPT system design is accordingly obtained with $D_{12}=1$ mm, $D_{23}=18$ mm, $D_{34}=1$ mm. The design is verified by the finite integration technique based CST in-air simulation and its experiment setup is shown in Fig. 5.7(b). Besides, CST simulation with the 3-layer tissue

model and the in-vitro experiment are accomplished as well to investigate the MR-WPT system performance for the implanted scenario.

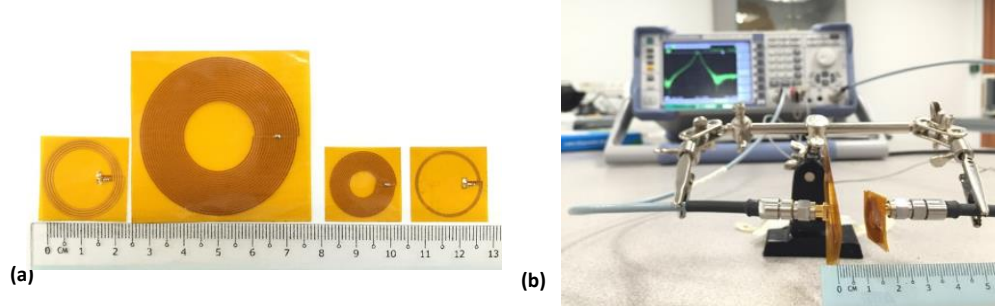


Figure 5.7 (a) Fabricated Flexible Coils (b) In-air Experiment Setup for the proposed MR-WPT system

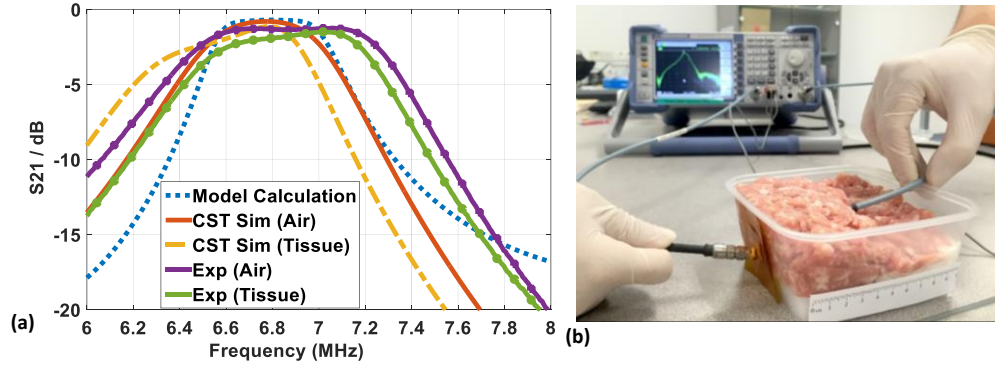


Figure 5.8 (a) Power Transfer Performance of the MR-WPT system in different test environments (b) In Vitro Experiment Setup for the proposed MR-WPT system

The system power transfer performance is presented in Fig. 5.8 (a) and Table 5.2. Based on the design procedure, we get an MR-WPT system with 72.6 % efficiency and 550 kHz 1-dB bandwidth. The proposed power transfer model shows a good coherence with the CST simulations. The involvement of tissue and the component value tolerance may lower system Q value and lead to the efficiency loss and bandwidth variation. Since the factors to cause bandwidth variation are unpredictable, it is still an appropriate choice to

design the transmission waveform conservatively based on the calculated bandwidth in our proposed model to avoid the possible transmission loss and guarantee high transfer efficiency. Based on the system configurations, we'd like to select the transmission waveform as a 3-tone evenly-spaced multi-sine signal with 6.78MHz center frequency and 230 kHz tone spacing.

Table 5.2 MR-WPT System Performance

Parameter	S_{21} (dB)	Efficiency (%)	Bandwidth (kHz)
Model Calculation	-0.82	82.8	460
CST Simulation (Air)	-0.88	81.7	440
CST Simulation (Tissue)	-1.12	77.2	510
Measurement (Air)	-1.16	76.5	620
Measurement (Tissue)	-1.39	72.6	550

It is also worth noting that the power transfer model provides the method to calculate its bandwidth and configure the waveform accordingly rather than to design the system to widen its bandwidth at the sacrifice of system Q-value and efficiency. Therefore, designing a high power transfer efficiency coil system is also crucial to get high overall system efficiency. In the comparison with the state-of-the-art implant designs as listed in Table 5.3, the proposed MR-WPT system has an outstanding performance and its high power transfer

efficiency provides a solid foundation for designing an entire high efficiency wireless power link for the biomedical implant applications.

Table 5.3 Coil System Performance Comparison

Ref.	Coil Dimension (mm) (R_t, R_r)	Frequency (MHz)	Implant Depth (mm)	Efficiency (%)
[69]	(15, 15)	4.5	10	54
[71]	(26, 5)	6.78	15	22
[6]	(22.5, 4)	5	15	47
[72]	(12,12)	2	12	40
This work	(24,10)	6.78	18	72.6

5.4.3 Reconfigurable Rectifier with the Multi-sine Waveform

For the incident multi-sine waveform, its high PAPR characteristic attributes to the rectifier's efficiency improvement but meanwhile limits its maximum input power range. By applying the proposed reconfigurable rectifier, the system both retains its high efficiency improvement and extends it to a much wider input power range. In this case, it successfully solves the early breakdown problem in the multi-sine incident. Meanwhile, it also enhances its efficiency improvement effect by extending the rectifier's maximum input power range and thus enlarging its application scenarios.

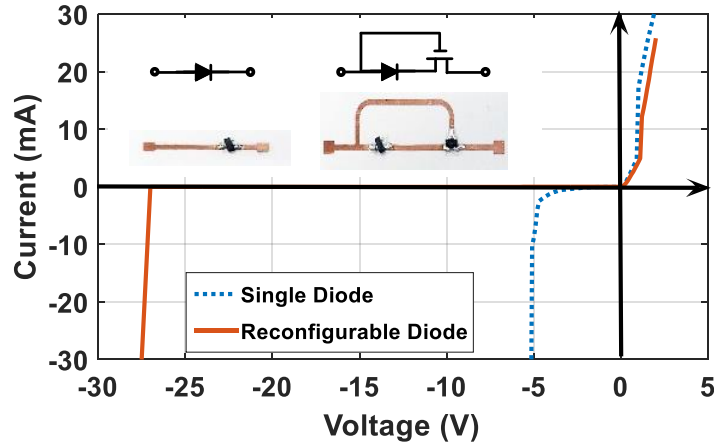


Figure 5.9 I-V curve of the traditional and the reconfigurable rectifier topology

Based on the waveform configurations in section 5.3, we apply the 1-stage reconfigurable rectifier with Schottky diode HSMS-2850 and N-channel MOSFET BF998. The measured I-V curves are shown in Fig. 5.9. It shows that the breakdown voltage of the proposed rectifier is widely extended from the original -5V to -28V without changing its 150 mV ultra-low threshold voltage. Both the high breakdown voltage and the ultra-low threshold voltage are achieved for high rectification efficiency with the multi-sine waveform.

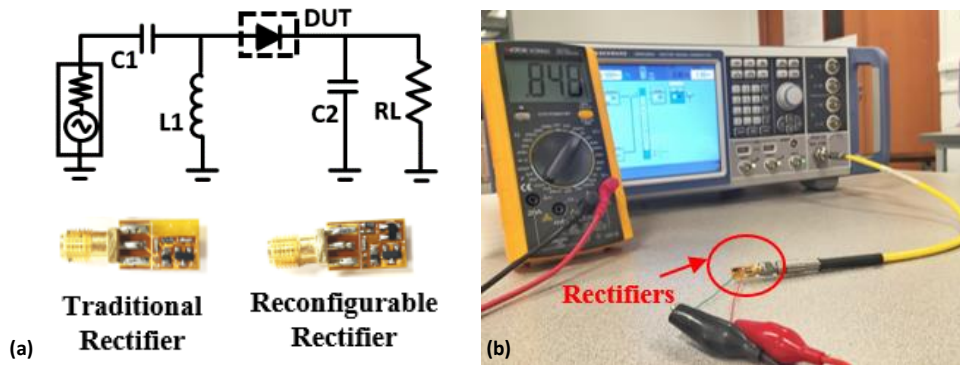


Figure 5.10 (a) Circuit Schematics and Fabricated Boards of the Rectifier Topologies. (b) Rectifier Test Experiment Setup. $C1=110\text{pF}$, $C2=500\text{pF}$, $L1=4.7\mu\text{F}$, $RL=1.8\text{K}\Omega$. DUT: Device Under Test.

The reconfigurable rectifier is specifically designed under 6.78MHz and tested as shown in Fig. 5.10. Both the RF-DC efficiency and its output voltage are presented in Fig. 5.11. Compared with the traditional single frequency CW signal, the 3-tone multi-sine waveform results in higher RF-DC efficiency, e.g. from 20% to 36.4% with -20dBm inputs into the traditional rectifier. The efficiency improvement contributed by the high PAPR multi-sine waveform retains until the traditional rectifier breaks down. As shown in Fig. 5.11, although the multi-sine transmission waveform has a higher conversion efficiency, its early breakdown limits the maximum output DC power and restrains the maximum input power range for the traditional rectifiers when applying the multi-sine waveform to improve the conversion efficiency.

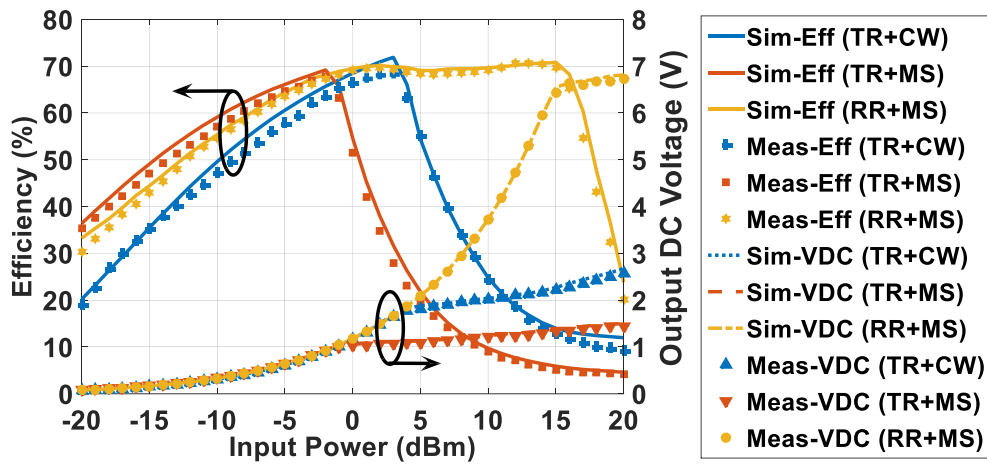


Figure 5.11 Simulated and Measured RF-DC Efficiency and Output Voltage Curves of the Traditional and the Proposed Reconfigurable Rectifier under Various Incident Waveforms. TR: Traditional rectifier, RR: Reconfigurable rectifier, CW: Continuous wave, single frequency, MS: Multi-Sine waveform

In order to solve this problem, the reconfigurable rectifier is designed to extend its available input power range as well as retain the high conversion efficiency from the multi-sine inputs. It obtains RF-DC efficiency improvement before breakdown and extends its high efficiency from -2 dBm to 15dBm for larger maximum input power shown in Fig. 5.11 and Table. 5.4.

As shown in Fig. 5.11 and the rectifier performance comparison in Table 5.4, we can see that the reconfigurable rectifier with the multi-sine input achieves high efficiency with extended maximum input power range. It achieves the efficiency above 50% from -13 to 17 dBm. The 50% efficiency point at -13dBm indicates the high rectification efficiency with the incident multi-sine waveform in the comparison in Table 5.4. Its wide power range of the efficiency above 50% to 17dBm shows its largely extended maximum input power and the high rectification efficiency in between. In contrast, the other rectifier designs in Table 5.4 with the traditional single frequency waveform only have relatively low efficiency in low power range and only a narrow power range is maintained. Therefore, from the experiment and comparisons above, we can draw the conclusion that the proposed reconfigurable rectifier not only eliminates the drawback of the multi-sine waveform but also strengthens its efficiency improvement to a wider power

range and it is a good candidate in designing a high efficiency wireless power link for biomedical implants.

Table 5.4 Rectifier Performance Comparison

Ref.	Topology	Pin (dBm) for eff. >50%	Maximum Pin (dBm)
[108]	Diode in series	-10 to 4	0
[109]	Diode in series	>-4 to 10	4
[100]	Dual diode structure	5 to 18	15
This work	Reconfigurable Rectifier	-13 to 17	15

5.5 Tissue Effects and In-vivo Test

5.5.1 Tissue Effects

When the designed receiver coils and circuits are implanted in the human tissue, there are two major concerns on the MR-WPT system from the influence of the surrounding tissues: a) Power propagation and absorption in the human tissue. b) Associated tissue heating with the absorbed RF power

Firstly, concerns on the absorption of high electromagnetic fields in the human body are addressed. Human EM exposure is evaluated in terms of the specific absorption rate (SAR) using (5.19), where σ is the electrical conductivity and ρ is the mass density of the tissue and E is the electric field.

Investigations [88][89] have also been done to evaluate the influence of the MR-WPT system on SAR.

$$SAR = \frac{\sigma E^2}{2\rho} \quad (5.19)$$

Safety standards on SAR are established by the IEEE and International Commission on Non-ionizing Radiation Protection (ICNIRP) as follows:

1) 1-g average SAR. The IEEE C95. 1-1999 standard [91] restricts the averaged SAR over 1-g tissue in the shape of a cube to be less than 1.6W/Kg.

2) 10-g average SAR. The IEEE C95.1-2005 standard [92] restricts the averaged SAR over 10-g tissue cube to be less than 2W/Kg.

Secondly, tissue temperature increase caused by the EM power absorption is another important safety consideration. The temperature increase of the surrounding tissue should not exceed more than 1-2 °C due to continuous heating caused by EM waves propagating in the tissue [47].

In order to investigate the tissue effects of the proposed MR-WPT system in practical environments, the voxel human body model is involved. The three-dimensional voxel human body male adult model ‘Gustav’ is used to evaluate the WPT system safe powering conditions for implantation on the back side of human waist (cube used: 25.6cm×12.7 cm×12.8 cm) as shown in Fig. 5.12 below. For the spinal cord stimulator applications, the receiver coil is

implanted 18 mm beneath the skin near human spine. The thermal evaluation has been done via the co-simulation with CST Microwave Suite and the stationary thermal solver in CST Multi-physics Suite. In the experiment, ambient temperature is set to 20 °C (293.1 K) and the body temperature is considered to be 37 °C (310.1K).

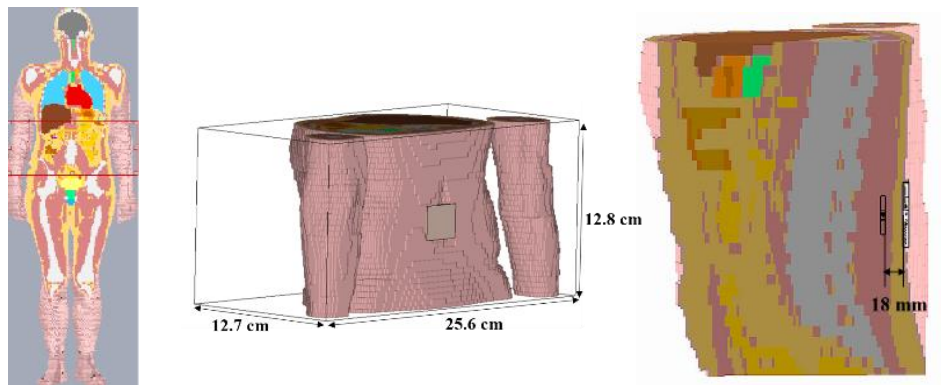


Figure 5.12 Three-dimensional Gustav Voxel human body model for the wireless power transfer system implanted in spine

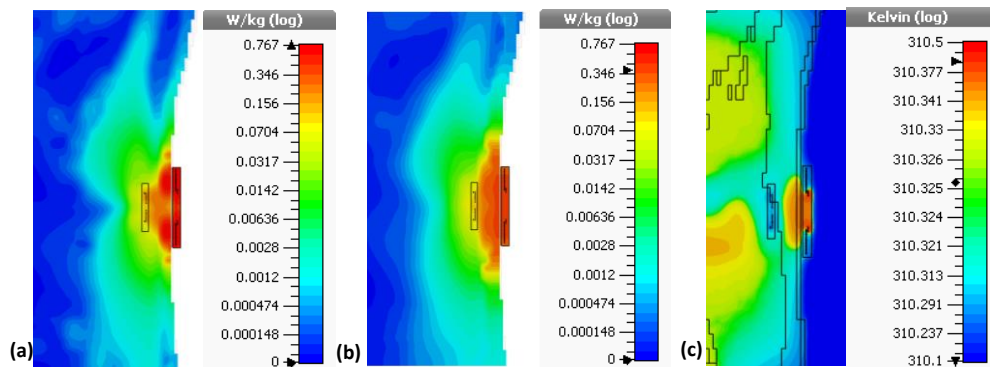


Figure 5.13 (a) 1-g average SAR distribution (b) 10-g average SAR distribution (c) temperature variation distribution in voxel human body model

The 1-g / 10-g average SAR distribution and the temperature increase are simulated and are presented in Fig. 5.13. As is shown, the maximum 1-g average SAR value is 0.767 W/Kg and 10-g average SAR value is only 0.368W/Kg and the temperature increase is 0.3°C. Both the SAR and

temperature increase of the MR-WPT system are far below the regulations for safety considerations.

5.5.2 In Vivo System Test in Rodent Model

In order to further investigate the system performance in the real tissue environment, the proposed multi-sine MR-WPT system is tested in vivo by conducting an experiment in the rat as shown in Fig. 5.14. The receiver coils and circuits are encapsulated within the biopolymer silicone Polydimethylsiloxane (PDMS) for biocompatible coating. The encapsulated receiver is implanted around the rat's spine 18 mm beneath its skin through an incision in the skin. The incision is sutured and RF power is delivered from the outside transmitter coil with the designed incident waveform being generated by R&S vector signal generator SMW200A.

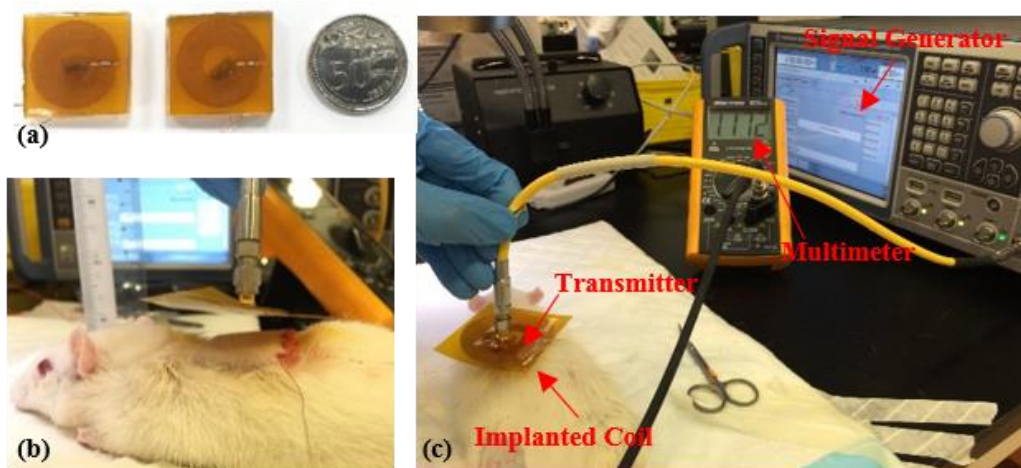


Figure 5.14 Rat Surgical Experiment and Measurement for the proposed multi-sine WPT system. (a) Encapsulated receiver coils and circuits (b) Receiver implanted inside the rat and the outside transmitter coil (c) In vivo test experiment setup.

The overall efficiency of the MR-WPT system is measured and plotted as shown in Fig. 5.15 below. Considering both the coils and circuits in the system, a maximum overall efficiency of 50.7% (72.6% transmission efficiency, 70.4% rectification efficiency) is achieved from the in vivo measurement with the incident 3-tone multi-sine waveform. It obtains high efficiency improvement over the traditional single-frequency waveform and largely extends its maximum input power range from original 3dBm to 15dBm. The proposed MR-WPT system with the multi-sine input allows high efficiency operations over wide power range.

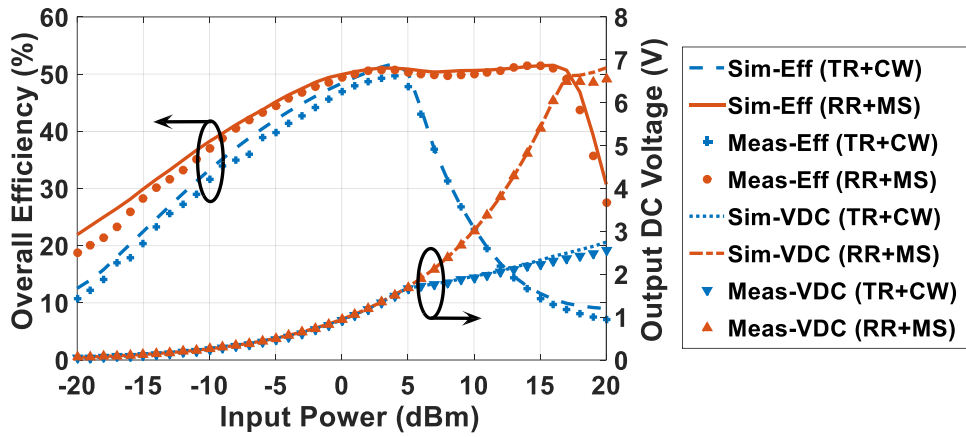


Figure 5.15 In vivo measurement of the overall system efficiency of the proposed multi-sine WPT system.

As reported in the in-vivo experiment, the proposed multi-sine MR-WPT system provides a high efficiency wireless power link with up to 20 mW (16dBm/39.8 mW is transmitted with 50.7% efficiency) power delivered to 18 mm inside the human body for the implanted neurostimulators or other

biomedical devices. Since it covers the power consumptions of the state-of-the-art neuro-stimulation chips [124], it would be a good candidate to replace the existing battery operated systems and to be used to power the fully implanted neurostimulators wirelessly in future. By applying more stages in the reconfigurable rectifier design, the available power range for the wireless power link can be further extended to fit more complex and power-consuming bio-implants applications.

5.6 Conclusion

In this chapter, a high efficiency magnetic resonant wireless power transfer system is designed with the optimized multi-sine waveform for implanted neurostimulation applications. Maximum overall system efficiency of 50.7% (72.6% transmission efficiency, 70.4% rectification efficiency) is achieved from 0-16 dBm input power range with the 3-tone, 230 kHz multi-sine waveform and considerations from the flexible coil design, system model design, and rectifier design to tissue effects evaluation. The optimized multi-sine waveform is for the first time applied in practical MR-WPT system design for in-vivo bio-implants.

From the perspective of the systematic design, the waveform-optimized WPT system prototype and the illustration of the design procedure presented

in chapter 5 integrate a number of component-level and block-level contributions to put the multi-sine WPT system from a research hotspot into a practical prototype and meanwhile provides a reference and insight for the future R&D in either academia or industry on the topic of WPT system design for biomedical applications

Chapter 6 Conclusion and Future Works

6.1 Conclusion

This thesis presents a completed design procedure for the waveform-optimized WPT system for miniaturized implantable biomedical devices. It is found that applying optimized waveforms with high PAPR in WPT systems helps to obtain a significant efficiency improvement without complicated system design. However, there are still some challenges to consider before it is finally applied in practical implantable devices. To design the waveform-optimized wireless power link for biomedical devices, several major contributions have been presented in the thesis and categorized as component, block and system level designs as shown in chapter 3, 4 and 5, respectively.

Firstly, a novel reconfigurable diode topology is presented in chapter 3 from the component level to increase the power handling ability of the WPT system with the optimized high PAPR waveforms. Different from the traditional off-the-shelf diodes, it achieves both ultra-low threshold voltage and high reverse breakdown voltage at the same time. These properties are highly desired when high PAPR waveforms incident and result in both high efficiency and extended operating power range. In the design of the

reconfigurable diode topology, an n-channel MOSFET is involved in the topology to hold the major portion of the reverse-bias voltage across the diode equivalent topology, which prevents the diode from breakdown and obtains a wide operating power range without enlarging its threshold voltage. With the two desired properties simultaneously achieved, the proposed reconfigurable diode topology is regarded as a good candidate for the proposed waveform-optimized WPT system to achieve both high efficiency and extended power range when applied in the implantable biomedical devices.

Besides the novel diode topology design, considerations on circuit blocks are also involved. Chapter 4 presents two contributions from both coil system and rectifier blocks, respectively. For the coil system design, a concise mathematical model for the MR-WPT coil system and a rapid design approach are presented to efficiently achieve the optimal efficiency of the WPT system within given scenarios. Moreover, it also serves as an optimal efficiency tracking strategy with the coupling coefficients variations in an MR-WPT system. For the rectifier design, a dual-band rectifier design aims to investigate the rectification efficiency improvement by the multi-frequency waveforms with different incident power ratios. Meanwhile, it also implements the reconfigurable diode topology in chapter 3 and realizes the

operating power range extension. All the designs mentioned above provide a powerful tool for analyzing the MR-WPT system and laid the foundation for investigating and practically implementing the waveform-optimized WPT system for biomedical implants.

Based on the theoretical analysis and circuit designs from the previous chapters, chapter 5 shows an entire system level WPT design with the multi-sine waveforms for the implantable neural stimulators. It involves all the design considerations in earlier chapters and provides a completed design procedure from flexible coil design, waveform design, rectifier design, bio-compatible considerations to the final in-vivo test. For the first time, the optimized multi-sine waveform excitations are implemented into practical MR-WPT system for IMD applications. The entire design procedures presented in Chapter 5 also can be regarded as a good reference for the future design of wireless power supply or the battery charger for the miniaturized biomedical devices.

In summary, a completed waveform-optimized WPT design procedure targeted at biomedical applications is presented in this thesis. Optimizations and designs are given from the fundamental diode topology design, circuit block design to the final system design with in vivo test. Theoretical deduction

and topology designs are adopted to improve the system efficiency and increase its robustness within complicated application scenarios. It would provide an excellent illustration for applying the optimized waveforms to achieve high efficiency and stable wireless power link for the implantable biomedical devices

6.2 Future Works

My research conducted in the past four years focuses on the designing the high-efficiency wireless power link for implantable bioelectronics with optimized waveform excitations, which delivers the RF power from outside human body to the targeted implanted medical electronic devices with carefully designed waveforms. Since the electromagnetic approach is currently the most promising and reliable power delivery solution for supplying the biomedical devices implanted inside human body, miniaturized implantable biomedical devices with a high-efficiency wireless power link has become a trend and consequently, the research and development on the waveform-optimized wireless power transfer for biomedical devices will be under the spotlight for quite a long time in the future. To further improve the functionality and robustness of the entire system, some other works could be investigated in future:

1. The refinement on the subsequent power management circuits.

In this thesis, RF power is efficiently delivered to the targeted devices as its DC power supply. However, the power cannot be fully utilized without the power management circuits to power the subsequent circuits or charge its battery. In most circuit designs, DC-DC converter is necessary to provide a standard and stable power supply. Within a wirelessly-powered bioelectronics system, the DC-DC converter is often intended to boost the rectified DC voltage to the standard power supply voltage like 3.3V or 5v, etc. Moreover, Low-dropout (LDO) regulator and battery monitor circuits would also be involved in the system if the system requires.

2. Enabling the simultaneous wireless power and information transfer.

In most state-of-the-art designs, the system has separated channels for communication and power delivery. It would have a good communication quality but at the sacrifice of the complicated system design with independent coil and antenna blocks. It would also be a feasible alternative to modulating the communication signals onto the transmission power waveform. A compact wireless power information transmission

system for the miniaturized biomedical devices could be developed with further research and investigation.

3. Development of high performance RF power transmitter.

As shown in the research, the multi-sine waveform is a good alternative for wireless power delivery to the bio-implants due to its high efficiency and harmless to the human body. However, to efficiently generate the high PAPR waveforms from the current power amplifiers is still a challenge. Related research could also be done to investigate high-performance RF power transmitter to deliver the power efficiently with various optimized waveforms.

Bibliography

[1] J. Andreu-Perez, D. R. Leff, H. M. D. Ip and G. Z. Yang, "From Wearable Sensors to Smart Implants--Toward Pervasive and Personalized Healthcare," IEEE Transactions on Biomedical Engineering, vol. 62, no. 12, pp. 2750-2762, Dec. 2015.

[2] D. Jeon, Y. P. Chen, Y. Lee, Y. Kim, Z. Foo, G. Kruger, D. Sylvester, "24.3 An implantable 64nW ECG-monitoring mixed-signal SoC for arrhythmia diagnosis," 2014 IEEE International Solid-State Circuits Conference (ISSCC), San Francisco, CA, 2014, pp. 416-417.

[3] X. Zou, W. S. Liew, L. Yao and Y. Lian, "A 1V 22 μ W 32-channel implantable EEG recording IC," 2010 IEEE International Solid-State Circuits Conference (ISSCC), San Francisco, CA, 2010, pp. 126-127.

[4] S. Vaddiraju, M. Kastellorizios, A. Legassey, D. Burgess, F. Jain and F. Papadimitrakopoulos, "Needle-implantable, wireless biosensor for continuous glucose monitoring," 2015 IEEE 12th International Conference on Wearable and Implantable Body Sensor Networks (BSN), Cambridge, MA, 2015, pp. 1-5.

[5] A. M. T. Salam, M. Mirzaei, M. S. Ly, D. K. Nguyen and M. Sawan, "An Implantable Closed loop Asynchronous Drug Delivery System for the

Treatment of Refractory Epilepsy,” IEEE Transactions on Neural Systems and Rehabilitation Engineering, vol. 20, no. 4, pp. 432-442, July 2012.

[6] R. Jegadeesan, S. Nag, K. Agarwal, N. V. Thakor and Y. X. Guo, "Enabling Wireless Powering and Telemetry for Peripheral Nerve Implants," IEEE Journal of Biomedical and Health Informatics, vol. 19, no. 3, pp. 958-970, May 2015.

[7] F. G. Zeng, S. Rebscher, W. Harrison, X. Sun and H. Feng, "Cochlear Implants: System Design, Integration, and Evaluation,” IEEE Reviews in Biomedical Engineering, vol. 1, no.7 , pp. 115-142, 2008.

[8] G. Wang, W. Liu, M. Sivaprakasam, M. Zhou, J. D. Weiland and M. S. Humayun, "A Dual-Band Wireless Power and Data Telemetry for Retinal Prosthesis," 28th IEEE Annual International Conference on Engineering in Medicine and Biology Society (EMBS '06), New York, NY, 2006, pp. 4392-4395.

[9] Q. Xu, D. Hu, B. Duan and J. He, "A Fully Implantable Stimulator With Wireless Power and Data Transmission for Experimental Investigation of Epidural Spinal Cord Stimulation," IEEE Transactions on Neural Systems and Rehabilitation Engineering, vol. 23, no. 4, pp. 683-692, July 2015.

[10] Y. J. Min, H. K. Kim, Y. R. Kang, G. S. Kim, J. Park and S. W. Kim, "Design of Wavelet-Based ECG Detector for Implantable Cardiac Pacemakers," IEEE Transactions on Biomedical Circuits and Systems, vol. 7, no. 4, pp. 426-436, Aug. 2013.

[11] M. B. Santana, P. Halje, H. Simplicio, U. Richter, M. A. Freire, "Spinal cord stimulation alleviates motor deficits in a primate model of Parkinson Disease." Neuron, Vol. 84, no.4, pp. 716 – 722, Apr. 2014.

[12] O. Aquilina, "A brief history of cardiac pacing," Images in Pediatric Cardiology, vol. 8, no. 4, pp. 17-81, Apr. 2006.

[13] P. Arzuaga, "Cardiac pacemakers: the past, present and future," IEEE Instrumentation & Measurement Magazine, vol. 17, no. 3, pp. 21-27, June 2014.

[14] C. J. Deepu, X. Zhang, W. S. Liew, D. Wong and Y. Lian, "An ECG-on-Chip With 535 nW/Channel Integrated Lossless Data Compressor for Wireless Sensors," IEEE Journal of Solid-State Circuits, vol. 49, no. 11, pp. 2435-2448, Nov. 2014.

[15] B. Amar, A. Ammar, B. Kouki, and Hung Cao, "Power Approaches for Implantable Medical Devices." Sensors, vol. 15, no. 11, pp. 889-914, Nov. 2015.

[16] K.T. Settaluri, H. Lo, R.J. Ram, “Thin thermoelectric generator system for body energy harvesting,” *Journal of Electronic Materials*, vol. 4, no. 1, pp. 984–988, Jan. 2012.

[17] P. Niu, P. Chapman, R. Riemer, X. Zhang, “Evaluation of Motions and Actuation Methods for Biomechanical Energy Harvesting,” *IEEE 35th Annual Power Electronics Specialists Conference*, Germany, 2004, pp. 2100–2106.

[18] X. Wei, J. Liu, “Power sources and electrical recharging strategies for implantable medical devices,” *Front. Energy Power Eng. China*, 2008, pp. 10–13.

[19] J. Sohn, S. B. Choi, D. Lee, “An investigation on piezoelectric energy harvesting for mems power sources” *Journal of Intelligent Material Systems and Structures*, vol. 25, no. 3, pp. 391-400, March 2005.

[20] M. Ghovanloo, K. Najafi, “A wireless implantable multichannel micro-stimulating system-on-a-chip with a modular architecture,” *IEEE Trans. Neural Syst. Rehabil. Eng.* Vol. 15, no. 7, pp. 449–457, July 2007.

[21] B. Lenaerts, R. Puers, “An inductive power link for a wireless endoscope” *Biosensors*, vol. 22, no. 5, pp. 1390–1395, May 2007.

[22] R. B. North, "Neural Interface Devices: Spinal Cord Stimulation Technology," Proceedings of the IEEE, vol. 96, no. 7, pp. 1108-1119, July 2008.

[23] C. Jian, G. Shumei and S. Yilin, "Development of a simultaneous monitoring system for non-invasive blood pressure and blood oxygen saturation," 2013 IEEE 11th International Conference on Electronic Measurement & Instruments (ICEMI), Harbin, 2013, pp. 968-973.

[24] Z. Chi, H. Jiang, J. Xia, H. Liu, Z. Weng and Z. Wang , "A smart capsule for in-body pH and temperature continuous monitoring," 2014 IEEE 57th International Midwest Symposium on Circuits and Systems (MWSCAS), College Station, TX, 2014, pp. 314-317.

[25] S. Smith, "An implantable drug delivery system with wireless power and communication," Bionic Health: Next Generation Implants, Prosthetics and Devices, London, 2009, pp. 1-88.

[26] C. O. Oluigbo, A. Salma and A. R. Rezai, "Deep Brain Stimulation for Neurological Disorders," IEEE Reviews in Biomedical Engineering, vol. 5, no. 10, pp. 88-99, Oct. 2012.

[27] G. T. A. Kovacs, C. W. Storment and J. M. Rosen, "Regeneration microelectrode array for peripheral nerve recording and stimulation," IEEE

Transactions on Biomedical Engineering, vol. 39, no. 9, pp. 893-902, Sept. 1992.

[28] X. Li, W.A. Serdijn, W. Zheng, Y. Tian and B. Zhang, "The injectable neurostimulator: an emerging therapeutic device." Trends in Biotechnology, vol. 33, no. 7, 388 – 394, July 2015.

[29] D. Ma, S. M. Sun, C. K. Ho, D. W. M. Mok, C. K. Chui and S. K. Y. Chang, "Wireless medical implant: A case study on the artificial pancreas," 2012 IEEE International Conference on Communications (CICC), Ottawa, ON, 2012, pp. 6096-6100.

[30] Evera. [Online]. Available: <http://www.medtronic.com/us-en/patients-/treatments-therapies/defibrillator-icd-tachycardia/evera-xt.html>

[31] VitalSense. [Online]. Available: <http://www.actigraphy.com/devices-/vitalsense/>

[32] Cochlear. [Online]. Available: <http://www.cochlear.com/wps/wcm/-connect/intl/home>

[33] SecondSight. [Online]. Available: <http://www.secondsight.com/>

[34] Soletra. [Online]. Available: <http://www.medtronic.eu/your-health-/essential-tremor/device/dbs-therapy/soletra-neurostimulator/>

[35] Proteus. [Online]. Available: <http://www.proteus.com/>

- [36] J. Holmberg et al., "Battery-less wireless instrumented knee implant," IEEE Trans. Med. Devices, vol. 7, no. 3, pp. 1–11, Mar. 2013.
- [37] Carmat. [Online]. Available: <http://www.carmatsa.com/en/>
- [38] J. E. Pandolfino et al., "Ambulatory esophageal pH monitoring using a wireless system," Am. J. Gastroenterol, vol. 98, no. 4, pp. 740–749, Apr. 2003.
- [39] N. Tesla, "The transmission of electrical energy without wires as a means for furthering peace," Electrical World and Engineer, vol. 9, no. 1, pp. 21- 24, January 1905.
- [40] P. E. Glaser, "Power from the Sun: Its Future," Science, vol. 162, no. 11, pp. 857- 861, November 1968.
- [41] N. Shinohara, "Wireless Power Transmission for Solar Power Satellite (SPS)," Space Solar Power Institute, Tech. Rep., 2000.
- [42] A. E. Abdulhadi, Yi Ding, M. Parvizi and R. Abhari, "Multi-Port UHF RFID tag antenna for enhanced energy harvesting of self-powered wireless sensors," 2014 IEEE MTT-S International Microwave Symposium (IMS2014), Tampa, FL, 2014, pp. 1-3.
- [43] J. A. Hagerty, F. B. Helmbrecht, W. H. McCalpin, R. Zane and Z. B. Popovic, "Recycling ambient microwave energy with broadband rectenna

arrays," IEEE Transactions on Microwave Theory and Techniques, vol. 52, no. 3, pp. 1014-1024, March 2004

[44] S. Kim et al., "Ambient RF Energy-Harvesting Technologies for Self-Sustainable Standalone Wireless Sensor Platforms," Proceedings of the IEEE, vol. 102, no. 11, pp. 1649-1666, Nov. 2014.

[45] J.A. Shaw, "Radiometry and the Friis transmission equation". Am. J. Physics vol. 81, no. 1, pp. 33-37, Jan. 2013.

[46] K. RamRakhyani, S. Mirabbasi and M. Chiao, "Design and Optimization of Resonance-Based Efficient Wireless Power Delivery Systems for Biomedical Implants," IEEE Transactions on Biomedical Circuits and Systems, vol. 5, no. 2, pp. 48-63, Feb. 2011

[47] C. Liu, Y. X. Guo, H. Sun and S. Xiao, "Design and Safety Considerations of an Implantable Rectenna for Far-Field Wireless Power Transfer," IEEE Transactions on Antennas and Propagation, vol. 62, no. 11, pp. 5798-5806, Nov. 2014.

[48] R. A. Bercich, D. R. Duffy and P. P. Irazoqui, "Far-Field RF Powering of Implantable Devices: Safety Considerations," IEEE Transactions on Biomedical Engineering, vol. 60, no. 8, pp. 2107-2112, Aug. 2013.

[49] U. M. Jow and M. Ghovanloo, "Design and Optimization of Printed Spiral Coils for Efficient Transcutaneous Inductive Power Transmission," IEEE Transactions on Biomedical Circuits and Systems, vol. 1, no. 9, pp. 193-202, Sept. 2007.

[50] A. P. Sample, D. T. Meyer and J. R. Smith, "Analysis, Experimental Results, and Range Adaptation of Magnetically Coupled Resonators for Wireless Power Transfer," IEEE Transactions on Industrial Electronics, vol. 58, no. 2, pp. 544-554, Feb. 2011.

[51] M. P. Theodoridis, "Effective Capacitive Power Transfer," IEEE Transactions on Power Electronics, vol. 27, no. 12, pp. 4906-4913, Dec. 2012.

[52] R. Jegadeesan, Y. X. Guo and M. Je, "Electric near-field coupling for wireless power transfer in biomedical applications," 2013 IEEE MTT-S International Microwave Workshop Series on RF and Wireless Technologies for Biomedical and Healthcare Applications (IMWS-BIO), Singapore, 2013, pp. 1-3.

[53] J. D. Griffiths, "Introduction to Electrodynamics-3rd Edition", Pearson Education, 2007.

- [54] C. Volkmar, T. Baruth, J. Simon, U. Ricklefs and R. Thueringer, "Arbitrarily shaped coils' inductance simulation based on a 3-dimensional solution of the Biot-Savart law," Proceedings of the 36th International Spring Seminar on Electronics Technology, Alba Iulia, 2013, pp. 210-215.
- [55] Rosa, B. Edward, "Calculation of the self-inductances of single-layer coils," Bulletin of the Bureau of Standards, Volume 2, No. 2, pp. 161, Feb 1906
- [56] M. Q. Nguyen, Z. Hughes, P. Woods, Y. S. Seo, S. Rao and J. C. Chiao, "Field Distribution Models of Spiral Coil for Misalignment Analysis in Wireless Power Transfer Systems," IEEE Transactions on Microwave Theory and Techniques, vol. 62, no. 4, pp. 920-930, April 2014.
- [57] J. Kim, D. H. Kim, J. Choi, K. H. Kim and Y. J. Park, "Free-Positioning Wireless Charging System for Small Electronic Devices Using a Bowl-Shaped Transmitting Coil," IEEE Transactions on Microwave Theory and Techniques, vol. 63, no. 3, pp. 791-800, March 2015.
- [58] K. Fotopoulou and B. W. Flynn, "Wireless Power Transfer in Loosely Coupled Links: Coil Misalignment Model," IEEE Transactions on Magnetics, vol. 47, no. 2, pp. 416-430, Feb. 2011.
- [59] K. Na, H. Jang, H. Ma and F. Bien, "Tracking Optimal Efficiency of Magnetic Resonance Wireless Power Transfer System for Biomedical Capsule

Endoscopy," IEEE Transactions on Microwave Theory and Techniques, vol. 63, no. 1, pp. 295-304, Jan. 2015.

[60] B. H. Waters, B. J. Mahoney, G. Lee and J. R. Smith, "Optimal coil size ratios for wireless power transfer applications," 2014 IEEE International Symposium on Circuits and Systems (ISCAS), Melbourne VIC, 2014, pp. 2045-2048.

[61] R. R. Harrison, "Designing Efficient Inductive Power Links for Implantable Devices," 2007 IEEE International Symposium on Circuits and Systems, New Orleans, LA, 2007, pp. 2080-2083

[62] L. Chen, S. Liu, Y. C. Zhou, and T. J. Cui, "An Optimizable Circuit Structure for High Efficiency Wireless Power Transfer" IEEE Transactions on Industrial Electronics, vol. 60, no. 1, pp. 339-349, Jan. 2013.

[63] J. Guo, H. Zhang and X. Zhu, "Theoretical Analysis of RF-DC Conversion Efficiency for Class-F Rectifiers," IEEE Transactions on Microwave Theory and Techniques, vol. 62, no. 4, pp. 977-985, Apr 2014.

[64] J. Guo and X. Zhu, "Class-F rectifier RF-DC conversion efficiency analysis," 2013 IEEE MTT-S International Microwave Symposium Digest (IMS), Seattle, WA, 2013, pp. 1-4.

[65] A. Boaventura, A. Collado, N. B. Carvalho and A. Georgiadis, "Optimum behavior: Wireless power transmission system design through behavioral models and

efficient synthesis techniques," *IEEE Microwave Magazine*, vol. 14, no. 2, pp. 26-35, Feb 2013.

[66] C. R. Valenta and G. D. Durgin, "Harvesting Wireless Power: Survey of Energy-Harvester Conversion Efficiency in Far-Field, Wireless Power Transfer Systems," *IEEE Microwave Magazine*, vol. 15, no. 4, pp. 108-120, June 2014.

[67] J. O. McSpadden, L. Fan, and K. Chang, "Design and experiments of high-conversion-efficiency 5.8-GHz rectenna," *IEEE Trans. Microwave Theory Tech.*, vol. 46, no. 12, pp. 2053–2060, Dec. 1998.

[68] T. W. Yoo and K. Chang, "Theoretical and experimental development of 10 and 35 GHz rectennas," *IEEE Transactions on Microwave Theory and Techniques*, vol. 40, no. 6, pp. 1259-1266, Jun 1992.

[69] Jiapin Guo and Xinen Zhu, "An improved analytical model for RF-DC conversion efficiency in microwave rectifiers," 2012 *IEEE MTT-S International Microwave Symposium Digest (IMS)*, Montreal, QC, Canada, 2012, pp. 1-3.

[70] H.C. Sun, Y.X. Guo, M. He, Z. Zhong, "A Dual-Band Rectenna Using Broad-Band Yagi Antenna Array for Ambient RF Power Harvesting," *IEEE Antennas and Wireless Propagation Letters*, vol. 12, pp. 918-921, 2013.

- [71] H. Sun, Z. Zhong and Y. X. Guo, "An Adaptive Reconfigurable Rectifier for Wireless Power Transmission," IEEE Microwave and Wireless Components Letters, vol. 23, no. 9, pp. 492-494, Sept. 2013.
- [72] A. Collado and A. Georgiadis, "Conformal Hybrid Solar and Electromagnetic (EM) Energy Harvesting Rectenna," IEEE Transactions on Circuits and Systems I: Regular Papers, vol. 60, no. 8, pp. 2225-2234, Aug. 2013.
- [73] C. Walsh, S. Rondineau, M. Jankovic, G. Zhao, and Z. Popovic, "A conformal 10 GHz rectenna for wireless powering of piezoelectric sensor electronics," in IEEE MTT-S Int. Microwave Symp. Dig, 2005, CA, US, pp. 143 - 146.
- [74] U. Olgun, C.-C. Chen, and J. L. Volakis, "Investigation of rectenna array configurations for enhanced RF power harvesting," IEEE Antenna Wireless Propag. Lett., vol. 10, no. 6, pp. 262-265, June 2011.
- [75] C. Gomez, J. A. Garcia, A. Mediavilla, and A. Tazon, "A high efficiency rectenna element using E-pHEMT technology," Proc. 12th GAAS Symposium., Amsterdam, NL, 2004, pp. 315 - 318.
- [76] W. C. Brown, "The History of Power Transmission by Radio Waves," IEEE Transactions on Microwave Theory and Techniques, vol. 32, no. 9, pp. 1230-1242, Sep 1984.

[77] A. S. Boaventura and N. B. Carvalho, "Maximizing DC power in energy harvesting circuits using multi-sine excitation," IEEE MTT-S International Microwave Symposium Digest (IMS), Baltimore, MD, 2011, pp. 1-3.

[78] C. C. Lo, Y. L. Yang, C. L. Tsai, C. S. Lee and C. L. Yang, "Novel wireless impulsive power transmission to enhance the conversion efficiency for low input power," 2011 IEEE MTT-S International Microwave Workshop Series on Innovative Wireless Power Transmission: Technologies, Systems, and Applications (IMWS), Uji, Kyoto, 2011, pp. 55-58.

[79] A. Boaventura, D. Belo, R. Fernandes, A. Collado, A. Georgiadis and N. B. Carvalho, "Boosting the Efficiency: Unconventional Waveform Design for Efficient Wireless Power Transfer," IEEE Microwave Magazine, vol. 16, no. 3, pp. 87-96, April 2015.

[80] A. Collado and A. Georgiadis, "Improving wireless power transmission efficiency using chaotic waveforms," IEEE MTT-S International Microwave Symposium Digest (IMS), Montreal, QC, Canada, 2012, pp. 17 - 22.

[81] M. S. Trotter, J. D. Griffin, and G. D. Durgin, "Power-optimized waveforms for improving the range and reliability of RFID systems," Proc. IEEE Int. Conf. RFID, Orlando, FL, 2009, pp. 80-87.

[82] A. S. Boaventura and N. B. Carvalho, "Extending reading range of commercial RFID readers," *IEEE Trans. Microwave Theory Tech.*, vol. 61, no. 1, pp. 633–640, Jan. 2013.

[83] C. R. Valenta, M. M. Morys and G. D. Durgin, "Theoretical Energy-Conversion Efficiency for Energy-Harvesting Circuits Under Power-Optimized Waveform Excitation," *IEEE Transactions on Microwave Theory and Techniques*, vol. 63, no. 5, pp. 1758-1767, May 2015.

[84] M. S. Trotter and G. D. Durgin, "Survey of range improvement of commercial RFID tags with Power Optimized Waveforms," 2010 IEEE Intl. Conf. on RFID, Orlando, FL, 2010, pp. 195-202.

[85] R.-H. Kim, , H. Tao, , T. Kim, , Y. Zhang, , S. Kim, , B. Panilaitis, M. Yang, D.-H. Kim, Y. H. Jung, B. H. Kim , Y. Li, , Y. Huang and J. A. Rogers, "Materials and Designs for Wirelessly Powered Implantable Light-Emitting Systems." *Small*, vol. 8, no. 9, pp. 2812–2818, Sep. 2012.

[86] C. Gabriel, S. Gabriel and E. Corthout. "The dielectric properties of biological tissues: I. Literature Survey". *Physics in Medicine and Biology*, Vol. 41, No. 11, pp. 2236-2253, Nov. 1996

- [87] C Gabriel, S Gabriel and E Corthout. "The dielectric properties of biological tissues: III. Parametric models for the dielectric spectrum of tissue". Physics in Medicine and Biology, Vol. 41, No. 11, pp. 2271-2293, Nov. 1996
- [88] A. Christ et al., "Evaluation of Wireless Resonant Power Transfer Systems With Human Electromagnetic Exposure Limits," IEEE Transactions on Electromagnetic Compatibility, vol. 55, no. 2, pp. 265-274, April 2013.
- [89] Xingyi Shi, B. H. Waters and J. R. Smith, "SAR distribution for a strongly coupled resonant wireless power transfer system," IEEE Wireless Power Transfer Conference (WPTC), Boulder, CO, 2015, pp. 1-4.
- [90] PA Hasgall, Di Gennaro F, Baumgartner C, Neufeld E, Gosselin MC, Payne D, Klingeböck A, Kuster N, "IT'IS Database for thermal and electromagnetic parameters of biological tissues," Version 3.0, September 01st, 2015, [Online].Available: <http://www.itis.ethz.ch/database>
- [91] IEEE Standard for Safety Levels With Respect to Human Exposure to Radio frequency Electromagnetic Fields, 3kHz to 300GHz, IEEE Standard C95.1,1999.
- [92] IEEE Standard for Safety Levels With Respect to Human Exposure to Radio frequency Electromagnetic Fields, 3kHz to 300GHz, IEEE Standard C95.1,2005.

[93] K. L. Montgomery, A. J. Yeh, J. S. Ho, V. Tsao, S. M. Iyer, L. Grosenick, E. A. Ferenczi, Y. Tanabe, K. Deisseroth, S. L. Delp, and A. S. Y. Poon, "Wirelessly powered, fully internal optogenetics for brain, spinal, and peripheral circuits in mice," *Nature Methods*, vol. 12, no. 6, pp. 969-974, June 2015.

[94] X. Wang, J. He, L. Guo, S. Sha and M. Lu, "Wireless charging for low-power mobile devices based on retro-reflective beamforming," 2014 IEEE Antennas and Propagation Society International Symposium (APSURSI), Memphis, TN, 2014, pp. 1411-1412.

[95] V. Marian, C. Vollaie, J. Verdier, and B. Allard, "Potentials of an Adaptive Rectenna Circuit", *IEEE Antennas Wirel. Propag. Lett.*, vol. 86, no. 10, pp. 1393–1396, Oct. 2011.

[96] Z. Liu, Z. Zhong, Y.X. Guo, "Enhanced Dual-band Ambient RF Energy Harvesting with Ultra-Wide Operating Power Range," *IEEE Microwave and Wireless Components Letters*, vol. 25, no. 9, pp. 630-632, Sep 2015.

[97] Z. Liu, Z. Zhong, Y. X. Guo, "Iterative Non-breakdown Rectifier Topology for Via-Tissue Multi-Sine Wireless Power Transmission," *IEEE MTT-S International Microwave Workshop Series on RF and Wireless*

Technology for Biomedical Healthcare Application, Taiwan, ROC, 2015, pp. 21-23.

[98] R. Jegadeesan and Y.X. Guo, "Topology selection and efficiency improvement of inductive power links," *IEEE Transactions on Antennas and Propagation*, vol. 60, no. 10, pp. 4846-4854, Oct 2012.

[99] Moh, K.-G. Neri, F. Sungwoo Moon, Pye Yeon, Jinhyuck Yu, Youso Cheon, Yong-seong Roh, Myeon Ko, Byeong-Ha Park, "12.9 A fully integrated 6W wireless power receiver operating at 6.78MHz with magnetic resonance coupling," 2015 IEEE International Solid-State Circuits Conference (ISSCC), San Francisco, CA, 2015, pp.1-3,.

[100] H. Takhedmit, B. Merabet, L Cirio, B Allard, F Costa, C. Voltaire, and O. Picon, "A 2.45-GHz dual-diode RF-to-dc rectifier for rectenna applications," *European Microwave Conference (EuMC)*, Paris. FR, 2010, pp.37-40.

[101] Defu Wang, and R. Negra, "Design of a dual-band rectifier for wireless power transmission," *IEEE Wireless Power Transfer Conference (WPTC)*, Italy, 2013, pp.127-130.

[102] S. Scorcioni, L. Larcher, and A. Bertacchini, "A Reconfigurable Differential CMOS RF Energy Scavenger With 60% Peak Efficiency and -21

dBm Sensitivity," IEEE Microwave and Wireless Components Letters, vol.23, no.3, pp.155-157, March 2013.

[103] K. Niotaki, A. Georgiadis, and A. Collado, "Dual-band rectifier based on resistance compression networks," IEEE MTT-S International Microwave Symposium (IMS), Tampa, FL, 2014, pp.1-3.

[104] C. R. Valenta and G. D. Durgin, "Rectenna performance under power-optimized waveform excitation," Proc. IEEE Int. Conf. RFID, Orlando, FL, 2013, pp. 237–244.

[105] R. Dengler, "Self-inductance of a wire loop as a curve integral". Advanced Electromagnetics, vol. 5, no. 1, pp. 1–8, Jan. 2013.

[106] S. Atluri and M. Ghovanloo, "Design of a wideband power-efficient inductive wireless link for implantable biomedical devices using multiple carriers", IEEE EMBS Conf. Neural Eng., San Diego, CA, 2005, pp. 533-537.

[107] Z. Liu, Z. Zhong and Y. X. Guo, "Rapid design approach of optimal efficiency magnetic resonant wireless power transfer system," Electronics Letters, vol. 52, no. 4, pp. 314-315, Feb 2016.

[108] B. R. Franciscatto, V. Freitas, J.-M. Duchamp, C. Defay, and T. P. Vuong, "High-efficiency rectifier circuit at 2.45 GHz for low-input power RF energy harvesting," Eur. Microw. Conf. (EuMC), Itlay, 2013, pp. 507–510.

[109] N. Zhu, R. W. Ziolkowski, and H. Xin, "Electrically small GPS L1 rectennas," *IEEE Ant. Wireless Propag. Letter*, vol. 10, no. 5, pp. 95–98, May 2011.

[110] H. M. Lee, "A Power-Efficient Wireless Neural Stimulating System with Inductive Power Transmission," Ph.D. Dissertation. School of Electrical and Computer Engineering, Georgia Institute of Technology, GA, US, 2014.

[111] Aristeidis Karalis, J.D.Joannopoulos, Marin Soljacic. "Efficient wireless non-radiative mid-range energy transfer". *Annals of Physics*, vol. 323, no. 1, pp. 34-38, Jan 2008.

[112] Andre Kurs, Aristeidis Karalis, Robert Moffatt, "Wireless Power Transfer via Strongly Coupled Magnetic Resonances". *Science*, vol. 317, no. 5, pp. 83-85, May 2007.

[113] Qi Wireless Charging Specifications v1.2.2 [Online]. Available: <http://www.qiwireless.com/>

[114] Air Fuel Wireless Power Transfer System Baseline System Specification (BSS) v1.3 [Online]. Available: <http://www.airfuel.org/>

[115] Power Matters Alliance [Online]. Available: <http://www.power-matters.org/>

[116] Alliance for Wireless Power [Online] Available: <http://www.a4wp.org/>